A Search for the Higgs Boson in the ZH Dilepton Decay Channel at CDF II

by

Ravi Shekhar

Department of Physics
Duke University

Date: ______________________________

Approved:

____
Assoc. Professor Ashutosh V. Kotwal, Advisor

____
Professor Richard G. Palmer

____
Professor Al Goshaw

Thesis submitted in partial fulfillment of the requirements for the degree of
Master of Science in the Department of Physics
in the Graduate School of Duke University
2009

Abstract

This dissertation describes a search for the Standard Model Higgs boson produced in association with the Z boson via Higgs-strahlung at the CDF II detector at the Tevatron. At a Higgs boson mass between 100 GeV/c^2 and 150 GeV/c^2, the primary Higgs decay mode is to a pair of b quarks. The associated Z boson decays to a pair of electrons or muons with significant branching fraction, allowing detection of a final event signature of two visible leptons and two b quarks. This specific final state allows exclusion of large QCD backgrounds, leading to a more sensitive search. To achieve maximum sensitivity, matrix element probabilities for ZH signal and the dominant backgrounds are used as components to a likelihood fit in signal fraction.

No significant result was observed. Using the Feldman-Cousins technique to set a limit with 2.7/fb of data, at 95% coverage and a Higgs boson mass of 115 GeV/c^2, the median expected limit was $12.1 \times \sigma_{SM}$ and a limit of $8.2 \times \sigma_{SM}$ was observed, where σ_{SM} is the NNLO theoretical cross section of $p\bar{p} \rightarrow ZH \rightarrow l^+l^-b\bar{b}$ at $\sqrt{s}$=1.96 TeV

Contents

Abstract iii

List of Tables vii

List of Figures viii

1 Introduction 1

2 Motivation and Theory 4

2.1 Standard Model 5

2.1.1 Fundamental Particles 6

2.1.2 Standard Model Symmetries 7

2.2 Quantum Chromodynamics 9

2.3 Electroweak Interactions 11

2.3.1 Goldstone Model 12

2.3.2 Higgs Mechanism 14

2.4 Higgs Phenomenology 16

2.4.1 Indirect Constraints 16

2.4.2 Tevatron Higgs Production 17

3 Experimental Apparatus 23

3.1 Tevatron 23

3.2 CDF II Detector 26

3.2.1 Cerenkov Luminosity Counter 29

3.2.2 Silicon Tracking 29

3.2.3 Central Outer Tracker 30

3.2.4 Calorimeters 31

3.2.5 Muon Detectors 31

3.3 CDF Software 32

3.3.1 Event Triggers 32

3.3.2 Lepton Identification 33

3.3.3 Jet Modeling and Reconstruction 35

3.3.4 SecVtx Tagging 37

4 Event Selection **38**

4.1 Event Criteria 39

4.1.1 Jets 40

4.1.2 b-Tagging 42

4.2 Backgrounds 43

4.3 Signal Acceptance 45

4.4 Event Totals 46

4.4.1 Pretag 46

4.4.2 Double Loose b-Tag 47

4.4.3 Single Tight b-Tag 48

5 Matrix Elements **49**

5.1 Matrix Element Approximations 49

5.1.1 Initial State 50

5.1.2 Final State 51

5.2 Jet Transfer Function 52

5.3 Processes 55

5.3.1 $ZH \to l^+l^- b\bar{b}$ and ZZ . . . 55
5.3.2 Z+jets . . . 56
5.3.3 $t\bar{t}$ . . . 57
6 Analysis Technique **58**
6.1 Likelihood Fitting — 1 . . . 58
6.2 Resampling . . . 59
6.3 Normalization . . . 60
6.4 Pseudo-Experiments . . . 63
6.5 Likelihood Fitting — 2 . . . 67
6.5.1 Combined Tag Channels . . . 68
6.5.2 Separated Tag Channels . . . 68
6.6 Feldman-Cousins Method . . . 70
6.7 Systematics . . . 74
7 Results **77**
8 Conclusions **81**
A Additional Plots **82**

List of Tables

2.1 Fundamental Forces in the Universe 4

4.1 Summary of Event Criteria 39

4.2 Central electron trigger path 39

4.3 Central muon trigger paths 40

4.4 Electron requirements 41

4.5 Muon requirements 41

4.6 Expected $ZH \rightarrow l^+l^-b\bar{b}$ events 45

4.7 Pretag background expectation 46

4.8 Double bTag background expectation 47

4.9 Single bTag background expectation 48

5.1 Transfer function constants 53

6.1 Normalization constants for matrix elements 62

6.2 Background b tagging rates 64

6.3 Signal b tagging rates 64

6.4 Rate Systematic scale factor 65

6.5 Background Fractions 69

6.6 Rate Uncertainties 74

7.1 Expected and Observed Limits 80

List of Figures

2.1 Fundamental particles in the Standard Model 5

2.2 Tree Level Standard Model Interactions 8

2.3 Vertices of QCD 9

2.4 A schematic diagram of the colors in QCD SU(3) group 10

2.5 Meson color configuration 11

2.6 Baryon color configuration 11

2.7 V_s and V_{sb} potentials 13

2.8 Goldstone Symmetry Breaking Potential 13

2.9 Theoretical Constraints on Higgs Mass 17

2.10 M_W combination 18

2.11 m_{top} combination 18

2.12 Summary of Electroweak Constraints on the Higgs 19

2.13 Global Fit to collider data 19

2.14 $p\bar{p} \to ZH$ Production Cross Section 20

2.15 Higgs Production Processes 21

2.16 Higgs Boson Branching Ratios 21

2.17 $ZH \to l^+l^-b\bar{b}$ production mechanism 22

3.1 Tevatron Complex 24

3.2 Integrated luminosity at CDF II 26

3.3 CDF detector schematic 27
3.4 CDF Tracking Volume 28
3.5 Silicon detector barrel structure 30
3.6 Muon detector coverage 32
3.7 Jet energy scale 36
3.8 Jet energy scale systematic uncertainty 36
4.1 ZH Higgs decay b-quark kinematics 42
4.2 $t\bar{t}$ and Drell-Yan Background Processes 43
4.3 $WW/WZ/ZZ$ Background Processes 44
4.4 $ZH \to l^+l^-b\bar{b}$ production mechanism 45
5.1 Jet Transfer Funtion Contours 53
5.2 Parton and Jet Spectra 54
5.3 Z+jets dominant production mechanism 56
6.1 A single log-likelihood curve 61
6.2 Normalization histogram in S_m 61
6.3 Pseudo-experiment Likelihood 71
6.4 Pseudo-experiment Log-likelihood 71
6.5 Measured Signal Fraction Peak Histograms 72
6.6 Measured Signal Fraction 2D Map 73
6.7 Feldman-Cousins Ratio 73
6.8 Shape Systematic Effects 76
7.1 Data Likelihood Curve 77
7.2 Feldman-Cousins confidence bands 78
7.3 Expected distribution of limits 79
7.4 $p\bar{p} \to ZH \to l^+l^-b\bar{b}$ limits at 95% coverage. 80

A.1 $M_H = 100\ GeV/c^2$ 83
A.2 $M_H = 105\ GeV/c^2$ 84
A.3 $M_H = 110\ GeV/c^2$ 85
A.4 $M_H = 115\ GeV/c^2$ 86
A.5 $M_H = 120\ GeV/c^2$ 87
A.6 $M_H = 125\ GeV/c^2$ 88
A.7 $M_H = 130\ GeV/c^2$ 89
A.8 $M_H = 135\ GeV/c^2$ 90
A.9 $M_H = 140\ GeV/c^2$ 91
A.10 $M_H = 145\ GeV/c^2$ 92
A.11 $M_H = 150\ GeV/c^2$ 93

1
Introduction

Over a century ago, future Nobel Laureate Albert A. Michelson wrote the famous words [1]

> The more important fundamental laws and facts of physical science have all been discovered, and these are now so firmly established that the possibility of their ever being supplanted is exceedingly remote [...] our future discoveries must be looked for in the sixth place of decimals.

At the end of the 19th century, Physics seemed like a complete, self-consistent theory. All of known Physics could be predicted by the classical theories of Mechanics, Fields, Electromagnetism and Thermodynamics. Nature was predicted so well that it led many, including Michelson and Lord Kelvin to believe there was nothing more to discover.

Yet two seemingly insignificant problems lingered. The æther could not be detected in an experimental setting, despite ever increasing sensitivity of measurements. And blackbody radiation of resonant cavities could not be explained without an infrared or ultraviolet divergence. The solution to the two problems came from Special Relativity and Quantum Mechanics respectively. In the 1940s these two ideas were integrated into Quantum Electrodynamics, an extremely accurate, predictive theory of the interaction of light and matter. Shortly thereafter, large numbers new of particles were observed at particle colliders leading to the coining of the term the *particle zoo*. There were many competing theories to explain the particle zoo, and eventually one was selected by a combination of experiment and theoretical progress. That theory is now called the Standard Model (SM).

The SM was developed with knowledge of a significant part of the particle zoo, so it fit the known particles quite well. It predicted several new particles which had not yet been observed, including what came to be known as the W and Z bosons, the gluon, and the bottom and top quarks. Each of these particles has been experimentally observed between the mid 1970s and 2000, making the SM one of the most successful and longest lasting theories of Modern Physics.

But the SM had one flaw; it required all particles to be massless. Because this to be empirically false, there must be a mechanism through which otherwise massless particles acquire mass. In 1964, Peter Higgs, along with five others proposed [2] that there is a field (now known as the Higgs Field) that permeates the universe and has a nonzero vacuum expectation value (vev). This nonzero vev causes symmetry breaking, leading to a coupling of otherwise massless particles to the Higgs field. The particles behave as if they are swimming through the thick, viscous Higgs field. This viscous field coupling produces terms in equations which are indistinguishable from inertial mass. This idea became to be known as the Higgs Mechanism and was incorporated into the SM, albeit with the drawback that each fundamental particle's coupling to the Higgs field is a free parameter in the SM. More on the Higgs and how it relates to the SM is presented in chapter 2.

It is interesting to consider the parallels between now and a century ago. Currently, the SM seems predictive of all of particle physics (with the possible exception of massive neutrino, see [3]). The only unobserved particle from the minimal, self-consistent SM is the Higgs boson. In both cases there seems to be a framework for understanding and predicting large parts of the physical world. Only a small piece of the puzzle is missing. Discovery of this piece would be another success to an amazingly successful theory. On the other hand, discovery of a null result would force a change in the SM and potentially open the door to significant new Physics. Regardless of the outcome, there is a gain in understanding of the universe. This makes the Higgs boson worth searching for.

This dissertation presents a search for the Higgs Boson produced in conjunction with the Z boson via Higgs-strahlung at the Collider Detector located at the Tevatron at Fermi National Accelerator Laboratory (CDF at FNAL), located outside Chicago, Illinois. The salient points of the detector apparatus and software is presented in chapter 3. Second order predictions of Higgs mass known from other parameters in the SM such as the W boson mass and top quark mass favor a Higgs with a mass between 50 and 200 GeV/c^2. The ZH associated production search presented in this dissertation has good sensitivity from 100 to 130 GeV/c^2, and is considered a 'low mass' Higgs search.

For Higgs boson masses between 100 and 150 GeV/c^2, the Higgs primarily decays to a pair of b quarks, $b\bar{b}$. The associated Z boson decays to two visible leptons approximately 7% of the time. The event signature to look for is a pair of b quark jets and a pair of opposite sign visible ($e^{\pm}$, $\mu^{\pm}$) leptons. The dilepton requirement in this event signature allows reduction of large QCD backgrounds (See chapter 4). However, this requirement is not so tight as to allow a simple counting experiment to be used; advanced analysis techniques are still required to maximize sensitivity.

The advanced analysis technique used is a likelihood fitter with the signal and background matrix element probabilities for each event. Matrix elements, presented in chapter 5, present a way of analyzing events somewhat independent from standard collaboration analysis tools, potentially allowing for technique semi-independent confirmation of results. The likelihood fitting technique used is presented in chapter 6. Finally, the results from this search are presented in chapter 7.

2

Motivation and Theory

We currently believe there are four fundamental forces in the universe, given in table 2. The two nuclear forces have a characteristic scale The SM attempts to predict the strong,

Force	Theory	Strength	Scale
Strong Nuclear	Chromodynamics	~ 10	10^{-15} m
Electromagnetic	Electrodynamics	$\sim 10^{-2}$	∞
Weak Nuclear	Flavordynamics	$\sim 10^{-13}$	10^{-18} m
Gravity	Geometrodynamics	$\sim 10^{-42}$	∞

Table 2.1: Fundamental Forces in the Universe [4]

weak and electromagnetic forces, as gravity is currently not entirely reconciled with Quantum Mechanics. One of the key findings is that above a certain energy ($\Lambda_{EW} \sim 100$ GeV), the weak and electromagnetic forces unify into the electroweak force. Based on what are called Grand Unified Theories (GUTs), we believe at still higher energies ($\Lambda_{\mathrm{GUT}} \sim 10^{15}$ GeV), the electromagnetic, strong and weak nuclear forces will merge into a single force.

We believe the Higgs boson to be on the same scale as $\Lambda_{EW} \sim 100\ GeV$, and therefore given the center of mass energy of 1.96 TeV at the Tevatron, we can reasonably search for the Higgs.

2.1 Standard Model

The major theoretical underpinnings of the Standard Model (SM) have been largely unchanged for almost forty years (with the significant exception of nonzero neutrino mass, see [3]). By the late 1970s, the Lagrangian for the Standard Model had been written down in its current form. Figure 2.1 summarizes the fundamental particles along with their crucial properties like mass, charge, and spin. With the exception of the Higgs, hereafter abbreviated as H, all of the particles predicted have been discovered.

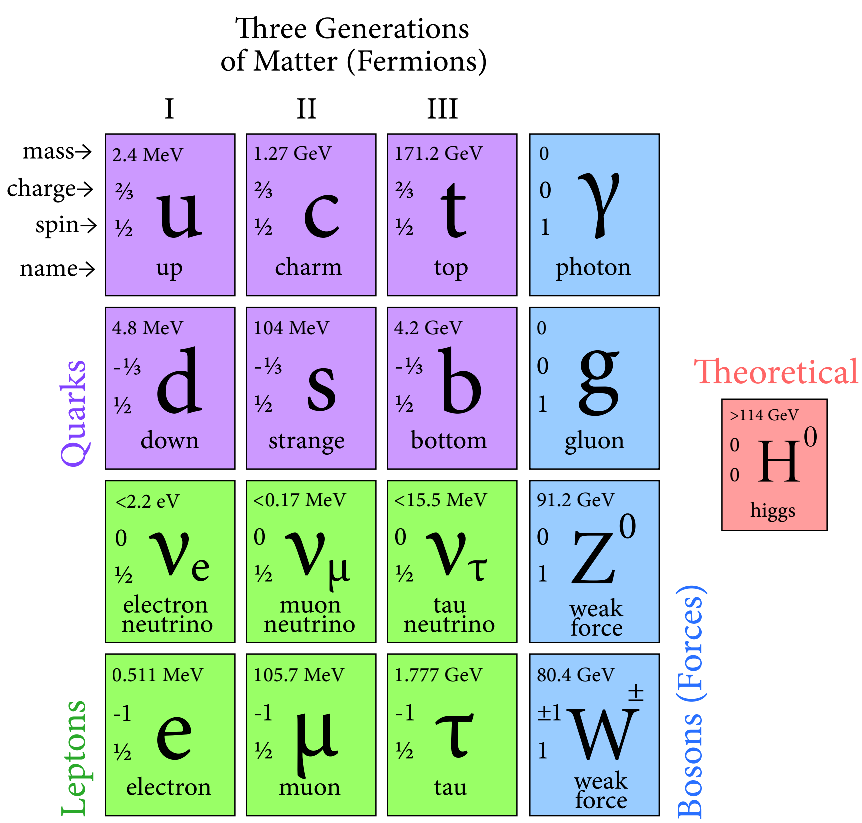

FIGURE 2.1: The minimum set of particles predicted by the Standard Model. Quarks and Leptons are fermions with spin=1/2 and the four bosons have spin 1. The Higgs Boson, which has not yet been observed has spin 0. Figure from [5]

2.1.1 Fundamental Particles

Particles can be classified according to the spin they have, either integer spin (0, 1, 2, ...), or half-integer spin ($\frac{1}{2}, \frac{3}{2}, \ldots$). Particles with integer spin are *bosons* and particles with half integer spin are *fermions*. Bosonic fields and fermionic fields transform differently under Lorentz Transforms, and have opposite symmetrization requirements for systems of identical particles. All particles that make up matter are fermions, whereas the particles that carry forces are bosons.

Looking at Figure 2.1, it is apparent that there is a left to right symmetry in the fermions. Each column is a *generation*, and each successive generation has particles with higher masses. The number of generations is not set by the SM, but all indications are that there are only three generations of matter. This symmetry between generations is called flavor symmetry and is broken by the fact that the particles have masses. Of course, in the high mass limit, flavor symmetry is regained between generations, which is often a useful fact when calculating cross sections and branching ratios.

Fermions

There are two classes of fermions, *quarks* and *leptons*. As seen in figure 2.1, there are six quarks and six leptons, as well as corresponding antiparticles.

The six quarks are: *up* (u), *down* (d), *charm* (c), *strange* (s), *top* (t), and *bottom* (b), and their oppositely charged antiparticles form the hadronic sector of the SM. Quarks couple to all four force carrying bosons (because they carry both color and electroweak charge) and occur in isospin doublets for each generation. Interestingly, the quark eigenstates that interact with the W and Z are linear combinations of the eigenstates that interact with the gluon. The eigenstates are related by the CKM Matrix [6]. Because of the nature of the color charge gluon interaction, free quarks are not observed in nature, existing only in bound states of two (mesons) or three (baryons) quarks.

The six leptons are ν_e, ν_μ, ν_τ, e, μ, and τ, and they come in isospin doublets like the quarks. The first three are neutral neutrinos and the others are charged leptons. Unlike quarks, leptons do not carry color charge, only electroweak charge. Consequently, they can exist as free particles. The neutrinos are believed to be left handed particles and therefore only couple to left handed W and Z bosons. The charged leptons couple to both left and right handed W, Z and γ bosons. More information on the SM predicted couplings is given in figure 2.2.

Bosons

Bosons are the force carriers and have integer spin. The photon, γ is the most well known and is the massless force carrier for the electromagnetic force. The Z boson, a carrier of the weak force, has no charge and behaves much like a very massive γ, with a mass of 91.2 GeV/c^2. Both are their own antiparticles, unlike the W, also a carrier of the weak force, which comes in two forms, W^+ and W^-. Unlike the γ and Z, the W interacts with other W particles, making the weak force non-abelian. Finally, the gluon is the carrier of the strong force, and is a massless bi-colored boson. Because it carries color charge, it can interact with other gluons, thus making the strong force non-abelian as well. The Higgs boson, still theoretical, is the quanta of the scalar Higgs field. It couples to itself, and to all massive particles. Couplings can be seen in figure 2.2.

2.1.2 Standard Model Symmetries

The Standard Model is formulated as a gauge theory. Gauge theories are elegant because once the gauge fields have been postulated, the interactions between the fields are a property of the gauge symmetry group. The SM is a

$$\mathrm{SU}(3)_C \times \mathrm{SU}(2)_L \times \mathrm{U}(1)_Y \tag{2.1}$$

theory. The SU(3) has a subscript C to indicate it represents the Quantum Chromodynamics (QCD) sector of the SM. This sector is also known as the colored sector because

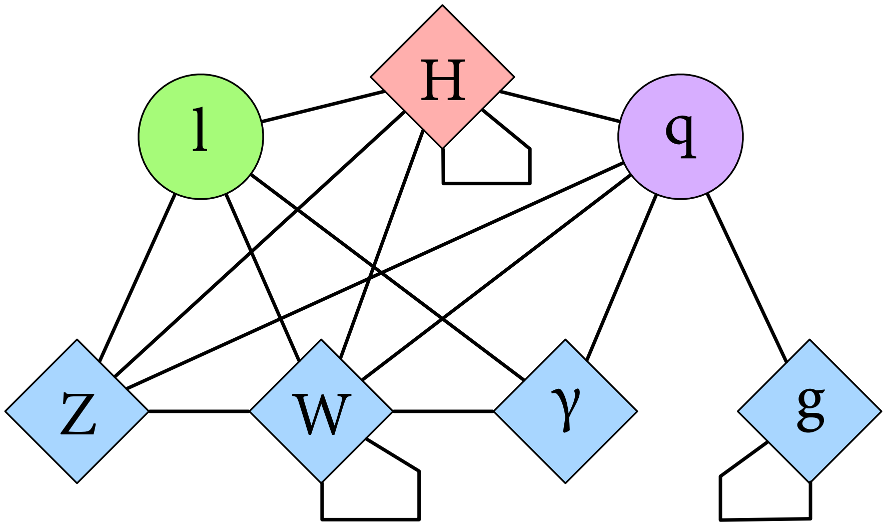

FIGURE 2.2: Tree level interactions in the Standard Model. Noticeably the H, W, and g all have self-couplings, making the fields non-abelian.

of the analogous relationship between the three vector fields and the three different additive components of white light: red, green and blue. The SU(2) group forms the weak sector and has the subscript L to indicate that the group contains left-handed weak isospin doublets. The U(1) forms the electromagnetic sector and has the subscript Y to indicate the group forms right-handed hypercharge singlets. The combined SU(2)×U(1) groups form the electroweak force.

From the gauge group, tree level interactions can be easily predicted. More detail for each sector will be given individually, but the tree level interactions between particles in the SM are given in figure 2.2. The diagram can be summarized as

- The H, W, and g bosons have self coupling, indicating that the associated fields are non-abelian.
- Both quarks and leptons interact with the electroweak and Higgs sectors, coupling to Z, W, γ, and H bosons.
- Gluons only couple to quarks and other gluons.

- The W and Z couple to the H, giving them mass, but the γ and g are massless.

2.2 Quantum Chromodynamics

Quantum Chromodynamics is the study of the strong force between quarks and gluons. The vertices of QCD are given in Figure 2.3. Gluons are the massless force carrying bosons, and are bicolored, whereas quarks carry a single color charge. The coupling of particles via the strong force is given by [7]

$$\alpha_s(q^2) = \frac{12\pi}{(33 - 2n_f)\log(q^2/\Lambda^2_{qcd})} \tag{2.2}$$

where $\Lambda_{qcd} \sim 200\ MeV$ and n_f is the number of quark flavors.

The most unusual thing about the strong force is that as distance between the particles

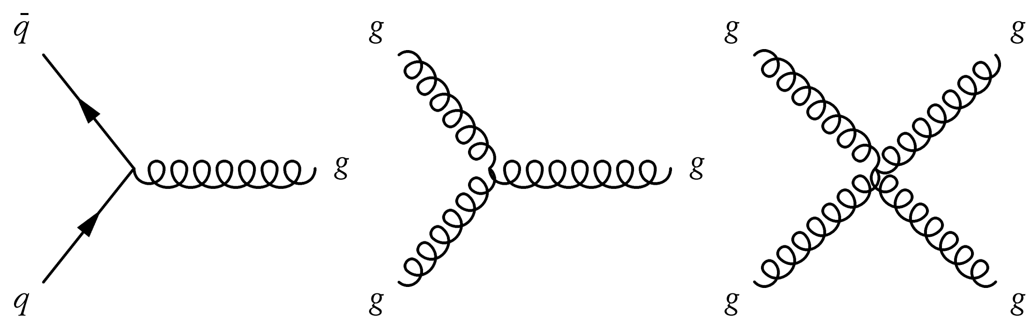

FIGURE 2.3: The vertices of QCD show quark-gluon and gluon-gluon coupling.

increases, the force between them also increases. This leads to the twin phenomena of *confinement* and *asymptotic freedom*. Confinement requires that free quarks do not exist; only quark bound states can exist. Asymptotic freedom states that in the limit of high energies (or alternatively small distances), quarks propagate as free particles, which is the logical extension of a force that increases with distance. This allows perturbation theory to be used for high center of mass energy scattering, like what is observed at the Tevatron. Figure 2.4 gives a rough schematic description of the QCD color states. Each

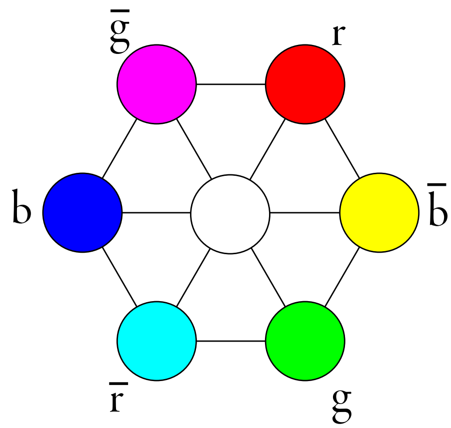

FIGURE 2.4: A schematic diagram of the colors in QCD SU(3) group

of the three basis states can be added with complex coefficients, which is not shown on the diagram. However, from the figure, it is evident that there is more than one way to achieve a colorless (white) state.

Confinement requires colored gluons and colorless quark bound states. The three basis states can be combined into nine independent states analogously to the addition of spins for three spin $\frac{1}{2}$ particles. There are eight colored octet states (equation 2.3) and a colorless singlet state $(r\bar{r} + b\bar{b} + g\bar{g})/\sqrt{3}$. The colorless state is not an allowed gluon state, so there are eight distinct allowed gluons. One convention defines the gluons as

$$\begin{array}{ll}
(r\bar{b} + b\bar{r})/\sqrt{2} & -i(r\bar{b} - b\bar{r})/\sqrt{2} \\
(r\bar{g} + g\bar{r})/\sqrt{2} & -i(r\bar{g} - g\bar{r})/\sqrt{2} \\
(b\bar{g} + g\bar{b})/\sqrt{2} & -i(b\bar{g} - g\bar{b})/\sqrt{2} \\
(r\bar{r} + b\bar{b})/\sqrt{2} & (r\bar{r} + b\bar{b} - 2g\bar{g})/\sqrt{6}
\end{array} \tag{2.3}$$

Correspondingly, there are two ways for quark bound states to achieve a colorless final state. The first is a meson (figure 2.5), which is a combination of a color and the corresponding anti-color, such as $r\bar{r}$. The second is a baryon (figure 2.6), which is an equal combination of the three colors (or anti-colors) like rgb. The QCD Lagrangian is given

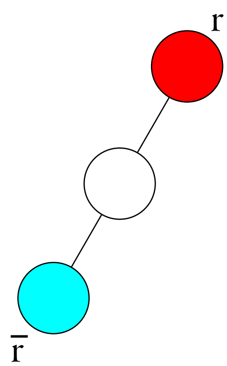

FIGURE 2.5: A possible meson color configuration

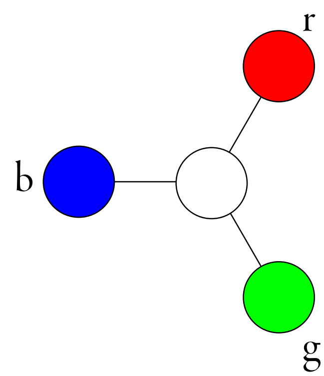

FIGURE 2.6: A possible baryon color configuration

by [8]

$$\mathcal{L}_{qcd} = -\frac{1}{4} F_a^{\mu\nu} F_{a\mu\nu} + \bar{\psi}_j \left(i\gamma_\mu D_{jk}^\mu - M_j \delta_{jk} \right) \psi_k \tag{2.4}$$

where the covariant derivative is

$$D_{jk}^\mu = \delta_{jk} \partial^\mu + ig(T_a)_{jk} G_a^\mu \tag{2.5}$$

and $F_a^{\mu\nu}$ is the ath field strength tensor, M is the quark mass matrix, g is the strong coupling constant, and T is the SU(3) generator matrices.

2.3 Electroweak Interactions

The electroweak interaction has the symmetry group $SU(2)_L \times U(1)_Y$. Weak Isospin (T_L) and hypercharge (Y) are the generators of the transformations. They relate to normal electromagnetic charge through the relation

$$Q = T_3 + \frac{1}{2} Y \tag{2.6}$$

where T_3 is the third component of weak isospin. The electroweak Lagrangian is

$$\mathcal{L}_{ew} = -\frac{1}{4} W^{\mu\nu} W_{\mu\nu} - B^{\mu\nu} B_{\mu\nu} + \bar{\psi} i \gamma^\mu D_\mu \psi \tag{2.7}$$

with the covariant derivative

$$D_\mu = \partial_\mu + i g W_\mu T + \frac{1}{2} i g' B_\mu Y \tag{2.8}$$

where $B_{\mu\nu} = \partial_\mu B_\nu - \partial_\nu B_\mu$, like the Maxwell field tensor. The B field represents the gauge field corresponding to the $\mathrm{U}(1)_Y$. The SU(2) corresponding gauge field is $W_{\mu\nu}$, defined as

$$W_{\mu\nu} = \partial_\mu W_\nu - \partial_\nu W_\mu - g W_\mu \times W_\nu \tag{2.9}$$

The W and B fields mix (see section 2.3.2) through a mixing angle θ_W (also known as the Weinberg angle). The third component of weak isospin mixes with B as

$$\begin{pmatrix} Z_\mu \\ A_\mu \end{pmatrix} = \begin{pmatrix} \cos\theta_W & -\sin\theta_W \\ \sin\theta_W & \cos\theta_W \end{pmatrix} \begin{pmatrix} W_\mu^3 \\ B_\mu \end{pmatrix} \tag{2.10}$$

creating the familiar Maxwell field A_μ and the Z boson field. Choosing $g' = g\tan\theta_W$ and $e = g\sin\theta_W$, the observable W is related to the ladder operators in SU(2), leading to a complete definition of all four fields as equations 2.11 - 2.13

$$W_\mu^\pm = \frac{1}{\sqrt{2}}\left(W_\mu^1 \mp i W_\mu^2\right) \tag{2.11}$$

$$Z_\mu = \frac{-g' B_\mu + g W_\mu^3}{\sqrt{g^2 + g'^2}} \tag{2.12}$$

$$A_\mu = \frac{g B_\mu + g' W_\mu^3}{\sqrt{g^2 + g'^2}} \tag{2.13}$$

2.3.1 Goldstone Model

Before attacking the full complexities of the SM, it is useful to consider a simplified case of symmetry breaking from a nonzero vacuum expectation value. Following the treatment of Goldstone [9], let us posit the existence of a complex scalar field $\hat{\phi}$.

$$\hat{\phi} = \frac{1}{\sqrt{2}}(\hat{\phi}_1 - i\hat{\phi}_2) \qquad \hat{\phi}^\dagger = \frac{1}{\sqrt{2}}(\hat{\phi}_1 + i\hat{\phi}_2) \tag{2.14}$$

with the Lagrangian density

$$\hat{\mathscr{L}}_G = (\partial_\mu \hat{\phi}^\dagger)(\partial^\mu \hat{\phi}) - \hat{V}(\hat{\phi}) \tag{2.15}$$

Now we consider two cases, $\hat{V}_s(\hat{\phi})$, $\hat{V}_{sb}(\hat{\phi})$

$$\hat{V}_s = \frac{1}{4}\lambda(\hat{\phi}^\dagger\hat{\phi})^2 + \mu^2\hat{\phi}^\dagger\hat{\phi} \qquad \hat{V}_{sb} = \frac{1}{4}\lambda(\hat{\phi}^\dagger\hat{\phi})^2 - \mu^2\hat{\phi}^\dagger\hat{\phi} \tag{2.16}$$

Clearly the Lagrangian is invariant under transforms in U(1), $e^{-i\alpha}$. And as shown in figure 2.7, the symmetric potential V_s has a minimum at $(\hat{\phi}^\dagger\hat{\phi})_{\min} = 0$. In a perturbative situation, there will be a Taylor expansion in $|\hat{\phi}|$ about the minimum. Because the minimum is zero, the classical average value of the $(\hat{\phi}^\dagger\hat{\phi})$ field is zero as well. The symmetry

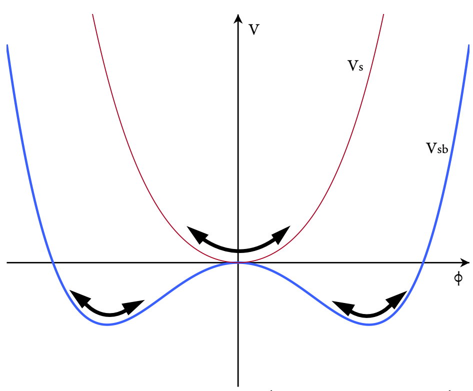

FIGURE 2.7: V_s and V_{sb} potentials

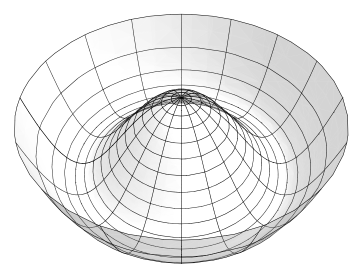

FIGURE 2.8: Goldstone Symmetry Breaking Potential

breaking potential V_{sb} only changes the sign of the second term. This causes a qualitative change in behavior. We follow the same strategy as V_s, doing a taylor expansion about the minimum, $(\phi^\dagger\phi)_{\min} = 2\mu^2/\lambda$ which can be rearranged into $v = 2|\mu|/\lambda^{1/2}$, where v is the vacuum expectation value (vev). A plot of the symmetry breaking potential in the $\hat{\phi}_1$, $\hat{\phi}_2$ plane is figure 2.8. Expanding about the minimum makes two modes immediately apparent, a radial mode with no restoring potential, and a transverse mode with roughly parabolic restoring potential. Because the radial component will be expanded about v, we posit the following form of $\phi(x)$

$$\hat{\phi}(x) = \frac{v + \hat{h}(x)}{\sqrt{2}} \exp(i\hat{\theta}(x)/v) \tag{2.17}$$

which leads to the Lagrangian density (up to second order)

$$\hat{\mathscr{L}}_G = \frac{1}{2}\partial_\mu \hat{h}\partial^\mu \hat{h} - \mu^2\hat{h}^2 + \frac{1}{2}\partial_\mu\hat{\theta}\partial^\mu\hat{\theta} + \mu^4/\lambda + O(\hat{\theta}^3, \hat{h}^3) \tag{2.18}$$

The $\mu^2\hat{h}^2$ term indicates that the $\hat{h}$ mode has a mass $\sqrt{2}\mu$. Yet the $\hat{\theta}$ mode has no corresponding mass term, indicating it is a massless boson, known as the Goldstone boson. This is logical considering that there is no restoring force in the θ direction.

This shows how the addition of a complex scalar field ϕ with nonzero vev breaks an internal symmetry, giving itself mass. Goldstone's Theorem [8] requires there be a massless mode as well. We now go on to the SU(2) × U(1) symmetry of the SM.

2.3.2 Higgs Mechanism

Following the same prescription as the Goldstone case, we introduce a complex scalar field isospin doublet

$$\phi = \begin{pmatrix} \phi^+ \\ \phi^0 \end{pmatrix} \tag{2.19}$$

the electroweak sector Lagrangian excluding fermions is therefore

$$\begin{aligned} \mathscr{L}_\phi = (D_\mu\phi)^\dagger(D^\mu\phi) + \mu^2(\phi^\dagger\phi) - \frac{\lambda}{4}(\phi^\dagger\phi)^2 \\ -\frac{1}{4}W_{\mu\nu}W^{\mu\nu} - B_{\mu\nu}B^{\mu\nu} \end{aligned} \tag{2.20}$$

Again, the minimum is at $(\hat{\phi}^\dagger\hat{\phi}) = -\mu^2/2\lambda$, and we expand about the minimum, using the same form as before, adjusted for SU(2)

$$\phi(x) = \exp\left(\frac{i\xi(x)\cdot\tau}{2v}\right)\begin{pmatrix} 0 \\ (v + H(x))/\sqrt{2} \end{pmatrix} \tag{2.21}$$

The fact that the SU(2) is a local symmetry allows us to gauge transform such that the $\xi(x)$ fields vanish (unitary gauge). Thus the $\phi(x)$ field is

$$\phi(x) = \begin{pmatrix} 0 \\ (v + H(x))/\sqrt{2} \end{pmatrix} \tag{2.22}$$

Substituting ϕ into 2.20 [8] as

$$\begin{aligned}
\mathscr{L}_\phi =& \frac{1}{2}(\partial_\mu H \partial^\mu H) - \mu^2 H^2 \\
& - \frac{1}{4}(\partial_\mu W_{1\nu} - \partial_\nu W_{1\mu})(\partial^\mu W_1^\nu - \partial^\nu W_1^\mu) + \frac{1}{8} g^2 v^2 W_{1\mu} W_1^\mu \\
& - \frac{1}{4}(\partial_\mu W_{2\nu} - \partial_\nu W_{2\mu})(\partial^\mu W_2^\nu - \partial^\nu W_2^\mu) + \frac{1}{8} g^2 v^2 W_{2\mu} W_2^\mu \\
& - \frac{1}{4}(\partial_\mu W_{3\nu} - \partial_\nu W_{3\mu})(\partial^\mu W_3^\nu - \partial^\nu W_3^\mu) - \frac{1}{4} B_{\mu\nu} B^{\mu\nu} \\
& + \frac{1}{8} v^2 (g W_{3\mu} - g' B_\mu)(g W_3^\mu - g' B^\mu)
\end{aligned} \tag{2.23}$$

The first two components of the W field have quadratic terms. This indicates the fields are massive with mass $M_W = gv/2$. The third component of the W field mixes with the B field. We can choose an orthogonal combination that mixes the two by an angle θ_W as in equation 2.10. Combined with the ladder W operators instead of isospin components

1 and 2, and equations 2.11-2.13, we get

$$\begin{aligned}\mathscr{L}_\phi =& \frac{1}{2}(\partial_\mu H \partial^\mu H) - \mu^2 H^2 \\ & - \frac{1}{4}(\partial_\mu W^+_\nu - \partial_\nu W^+_\mu)(\partial^\mu W^{+\nu} - \partial^\nu W^{+\mu}) + \frac{1}{8} g^2 v^2 W^+_\mu W^{+\mu} \\ & - \frac{1}{4}(\partial_\mu W^-_\nu - \partial_\nu W^-_\mu)(\partial^\mu W^{-\nu} - \partial^\nu W^{-\mu}) + \frac{1}{8} g^2 v^2 W^-_\mu W^{-\mu} \\ & - \frac{1}{4}(\partial_\mu Z_\nu - \partial_\nu Z_\mu)(\partial^\mu Z^\nu - \partial^\nu Z^\mu) + \frac{1}{8}(g^2 + g'^2) v^2 Z_\mu Z^\mu \\ & - \frac{1}{4}(\partial_\mu A_\nu - \partial_\nu A_\mu)(\partial^\mu A^\nu - \partial^\nu A^\mu) \end{aligned} \tag{2.24}$$

which is the electroweak lagrangian without any fermion terms. In this case, it is apparent that there are five gauge bosons, four of which have mass, H, $W^\pm$, Z, and one which is massless. The addition of the Higgs field also introduces mass terms for the fermions in the SM. That derivation will not be discussed here, in favor of deferring to a lucid explanation in Chapter 22 of [8] .

2.4 Higgs Phenomenology

The previous section focused on the tree level Standard Model theory. Now we must explore the specifics of higher order corrections as it applies to the search for the Higgs boson at the Tevatron.

2.4.1 Indirect Constraints

Partial wave scattering amplitudes for gauge boson pairs in the SM violate unitarity if the Higgs Boson mass exceeds 1 TeV/c^2 [10, 11]. There is also a vacuum stability constraint [12] requiring the Higgs boson mass to be greater than 4 GeV/c^2. Together these two constraints set a lower and upper bound on the Higgs boson mass within the confines of the SM. The constraints are believed to be related to the level of the Λ_{GUT}, where the

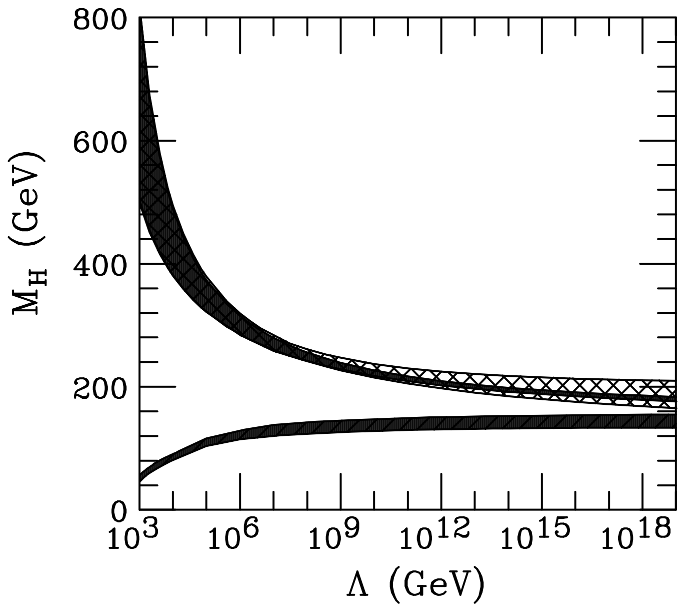

FIGURE 2.9: Theoretical Constraints on Higgs Mass [12] [13]

SM breaks down and we expect new physics. Figure 2.9 relates the two constraints and Λ_{GUT}.

The SM also provides constraints on the Higgs boson mass from the measured top quark and W boson masses. The current world average of the W Boson mass is $80.398 \pm 0.025\ GeV/c^2$ [6]. The top quark mass average is $173.1 \pm 1.6\ GeV/c^2$ [14].

Figures 2.12 and 2.13 show that all the measured SM parameters combined with the direct exclusion from LEP favor a Higgs boson between 114 GeV/c^2 and 140 GeV/c^2. This happens to be the region where the ZH associated production process is the most sensitive.

2.4.2 Tevatron Higgs Production

Figure 2.14 summarizes the cross sections for different production mechanisms at $\sqrt{s} = 1.96\ TeV$ at the Tevatron.

The four dominant production processes are given in figure 2.14, and the Higgs

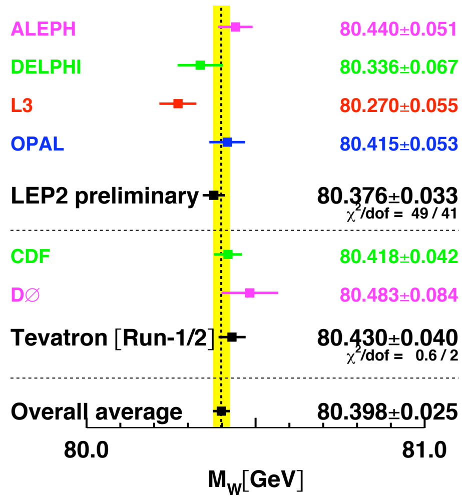

FIGURE 2.10: M_W combination [6]

branching ratios are given as a function of mass in figure 2.16. The production of Higgs through gluon-gluon fusion is predicted to have the largest cross section, but with a final state of two quarks (most likely $b\bar{b}$) at lower Higgs masses, it is completely swamped by QCD background. The next largest cross section is associated WH production, which is the subject of other searches at the Tevatron. This dissertation focuses on associated

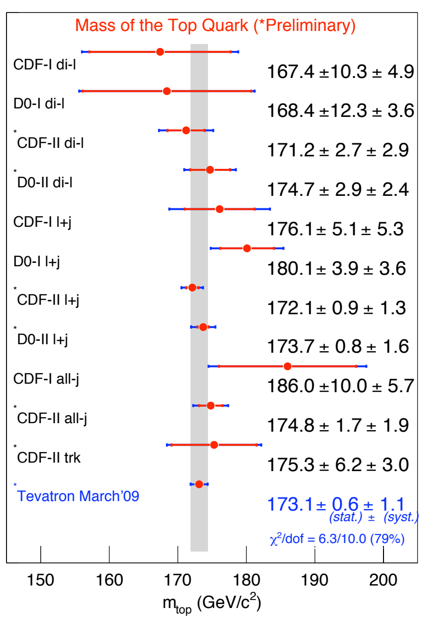

FIGURE 2.11: m_{top} combination [14]

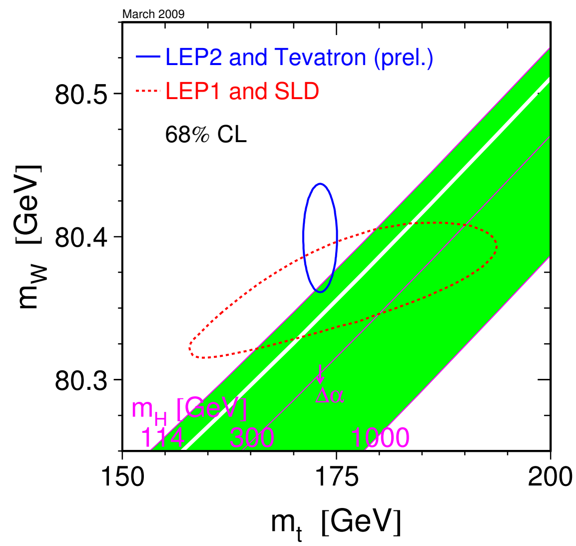

FIGURE 2.12: Summary of Electroweak Constraints on the Higgs [15] [16]. The blue ellipse is the 68% confidence interval centered around the current best measurements of m_W and m_t, and favors a Higgs mass below 150 GeV/c^2. Direct exclusion from LEP excludes the Higgs below 114 GeV/c^2 at 95% confidence

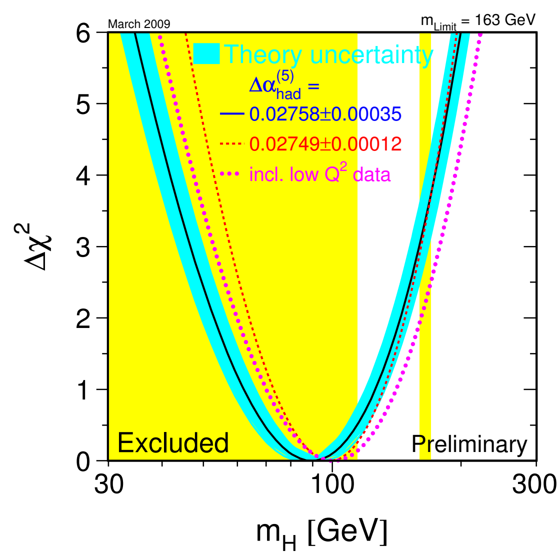

FIGURE 2.13: Global Fit to collider data [15] [16]. Excluded regions are shown in yellow, but here too we see a preference for a low mass Higgs boson

M_H	$q\bar{q} \to ZH$ (fb)
100	169.0
105	145.0
110	125.0
115	107.9
120	93.7
125	81.6
130	71.2
135	62.4
140	54.8
145	48.2
150	37.6

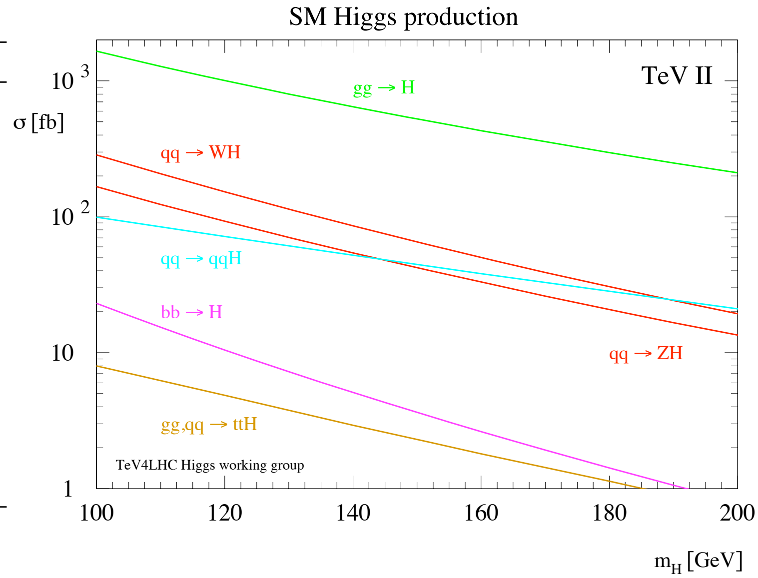

FIGURE 2.14: $p\bar{p} \to ZH$ Production Cross Section [17]

ZH production via Higgs-strahlung, as shown in the third diagram of figure 2.15.

The ZH state consists of two heavy bosons. Since both couple to the QCD sector and to leptons, they can both decay hadronically or leptonically. Higgs decays to a particle are proportional to the coupling between H and the particle. As the heaviest particle accessible for Higgs boson masses below twice the W boson mass, the H preferentially decays to $b\bar{b}$, as in figure 2.16. The Z predominately decays hadronically, but does decay to e^+e^- and $\mu^+\mu^-$ a total of 7% of the time. The diagram is figure 2.17. The combination $ZH \to l\bar{l}b\bar{b}$ process has a low cross section, but the requirement of a dilepton signature from the Z greatly reduces QCD background.

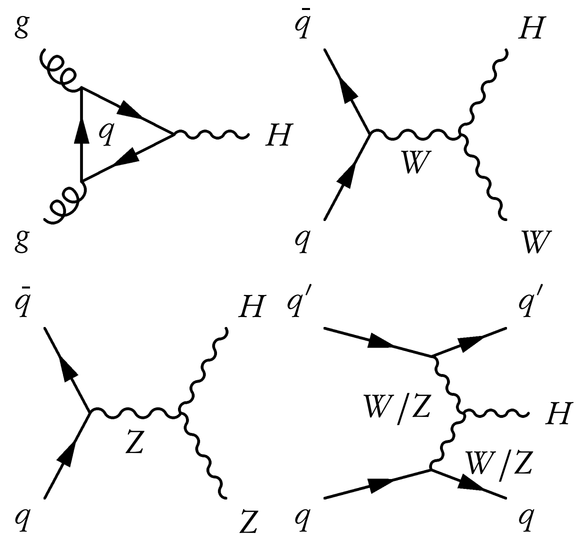

FIGURE 2.15: Dominant Higgs production processes at the Tevatron [18]. The subject of this dissertation is the lower left diagram.

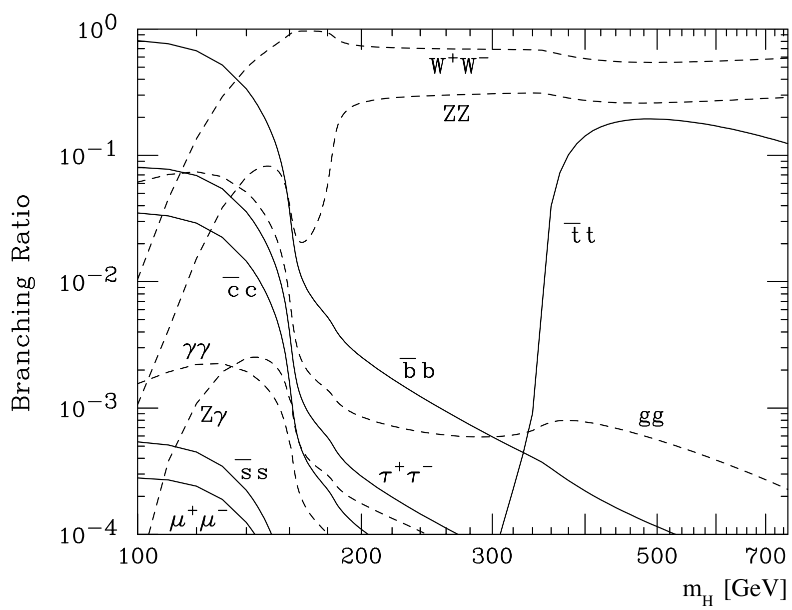

FIGURE 2.16: Higgs Boson Branching Ratios [6]

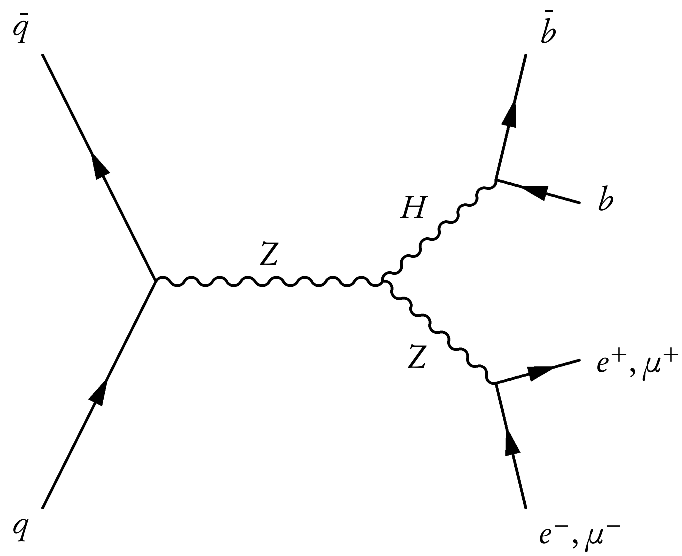

FIGURE 2.17: $ZH \rightarrow l^+ l^- b\bar{b}$ production mechanism

3

Experimental Apparatus

Since the 1940s, the study of particle physics has required collisions at higher and higher particle energies. The latest operational particle accelerator is the Tevatron, located at Fermi National Accelerator Lab (FNAL) in Batavia, Illinois. Originally constructed in the 1980s, the Tevatron was upgraded in 1999 to achieve a center of mass collision energy of $\sqrt{s} = 1.96\ TeV$. This makes the Tevatron the highest energy hadron collider currently operational. The colliding particles are protons (p) and anti-protons ($\bar{p}$), and through a multi-stage process, the Tevatron accelerates them to a speed of $\beta = 0.999999$, or one part per million away from the speed of light.

3.1 Tevatron

The Tevatron is a 6.3 km circumference circular accelerator that collides p and $\bar{p}$, shown in figure 3.1. Hydrogen gas is separated into constituent atoms, which are then ionized into H^-. These ions enter a Crockcroft-Walton pre-accelerator [19], which applies an electric field to the ions and accelerates them to $750\ keV$. The ions then enter the linear accelerator (Linac), which uses RF waves to further increase the energy to $400\ MeV$.

The electrons are stripped from the H^- ions, leaving protons, which are injected into the booster. The booster is a synchrotron with a 0.5 km circumference, and it accelerates the protons to 8 GeV. These protons are then injected into Main Injector, a larger synchrotron 3 km in circumferance.

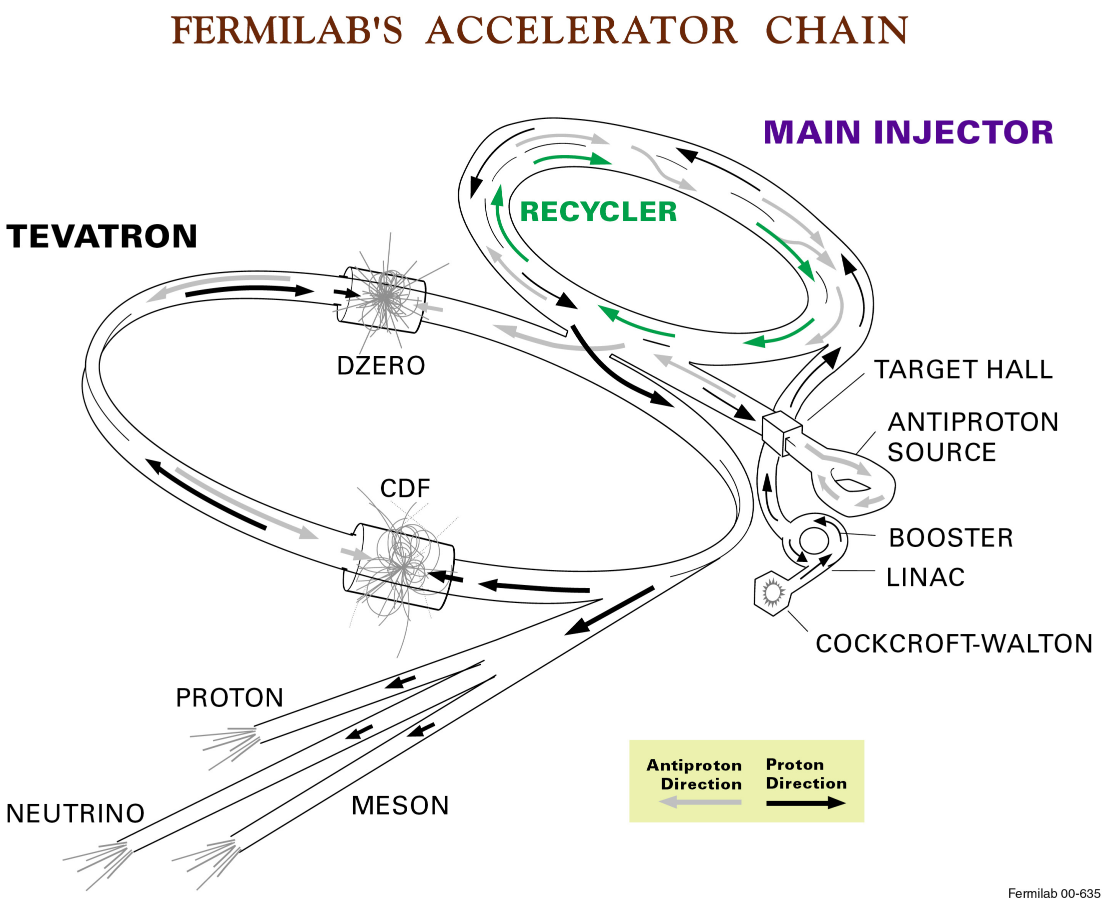

FIGURE 3.1: Tevatron Complex [19]

The Main injector performs several functions, although not concurrently. First, it accelerates the protons from the booster to 150 GeV, and injects them into the main Tevatron ring. Second, for $\bar{p}$ production, it accelerates protons to 120 GeV, which are then directed into a nickel target, which produces a large number of particles, including the constituents for $\bar{p}$, which are directed toward the anti-proton source. Third, it is used to collect $\bar{p}$ produced by the anti-proton source, and accelerating them to 150 GeV

as well, for injection into the main Tevatron ring.

Many different types of particles are produced when the nickel target is struck by 120 GeV protons. The anti-protons are separated out by magnetic spectroscopy, and are then moved to the Debuncher. Since the anti-protons have a very large spread in momentum, the Debuncher reduces the momentum spread. The anti-protons are then moved to the Accumulator, which stores anti-protons until they are ready for injection into the main ring, at which time they are moved to the main injector, accelerated to 150 GeV and then injected into the main Tevatron ring. Producing anti-protons in this manner is difficult, and is the limiting factor in instantaneous luminosity at the Tevatron.

The Recycler, which shares a tunnel with the Main Injector, was originally conceived to store anti-protons between physics runs. This proved unfeasible, but the Recycler turned out to be useful as an additional place to store anti-protons besides the Accumulator. This greatly increases the anti-protons available during a physics run, and consequently greatly increases the instantaneous luminosity of the Tevatron.

The main Tevatron ring accepts protons and anti-protons at an energy of 150 GeV from the Main Injector. They are accelerated using superconducting 4.2 T magnets in the 6.3 km circumference ring to 0.98 TeV, making the center of mass energy $\sqrt{s} = 1.96$ TeV. The p and $\bar{p}$ beams travel in opposite directions around the ring, and cross at the two detectors, the Collider Detector at Fermilab (CDF) and DØ detectors.

If the p and $\bar{p}$ were equally distributed throughout the ring, the chance of a collision at any given time would be very low because of a lack of sufficient densities. To remedy this, the particles are distributed into bunches, about 50 cm long, each containing roughly 10^{11} p and $\bar{p}$. There are 36 bunches of both p and $\bar{p}$ located around the ring, and they cross every 396 ns [6]. Bunching greatly increases instantaneous luminosity, which is given by the formula

$$\mathscr{L} = \frac{N_B N_p N_{\bar{p}} f}{2\pi \sigma_p^2 \sigma_{\bar{p}}^2} \tag{3.1}$$

where N_B is the number of bunches in the ring, N_p ($N_{\bar{p}}$) are the number of protons (anti-protons) per bunch, f is the bunch revolution frequency, and σ_p ($\sigma_{\bar{p}}$) is the effective width of the proton (anti-proton) bunches. The integrated luminosity (in units of pb^{-1}), when combined with the cross section (in pb) gives the number of collisions that occurred. Since the beginning of Run II in March 2001, the integrated luminosity is shown in figure 3.2. This analysis uses 2.7 fb^{-1} of CDF II data, through period 17.

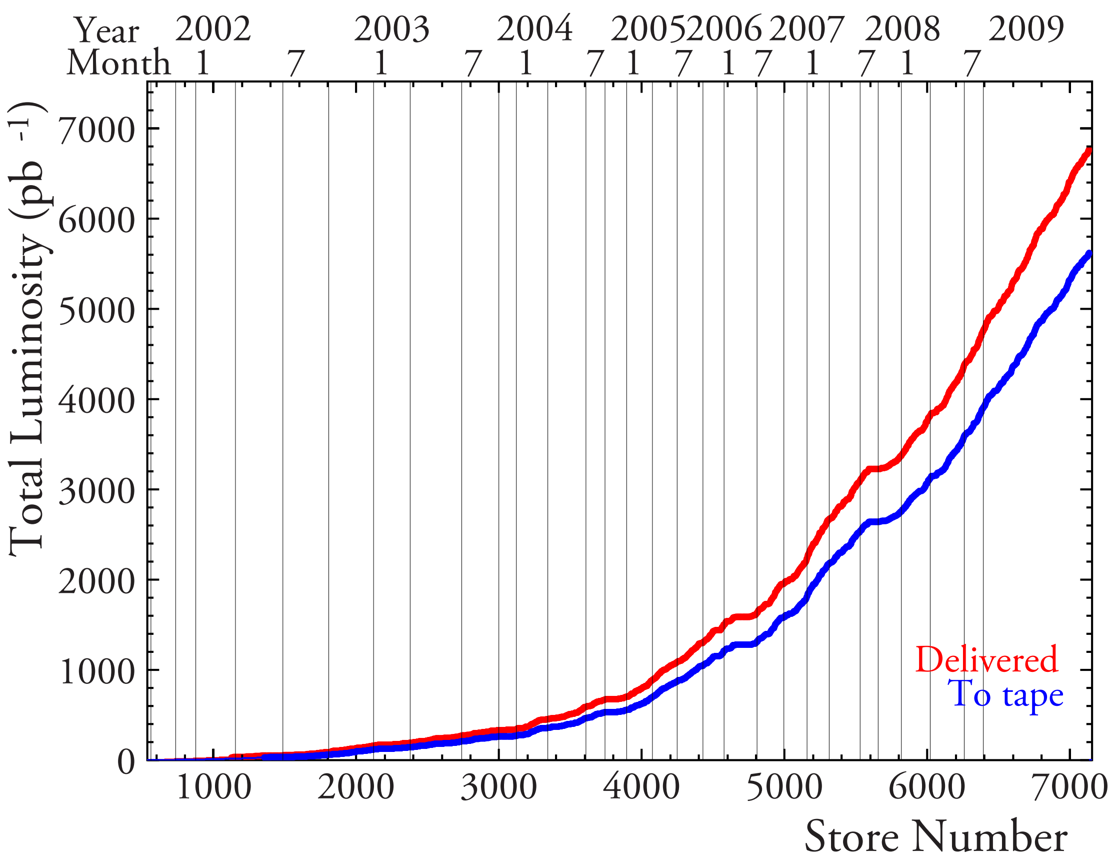

FIGURE 3.2: Integrated luminosity at CDF II

3.2 CDF II Detector

The CDF detector is a general purpose, azimuthally and forward-backward symmetric detector at the Tevatron. The z axis is taken to be along the proton beam direction, and the ϕ is defined with respect to the outward direction on the Tevatron ring. Because the cylindrical coordinate is not invariant under Lorentz transforms, the pseudo-rapidity is used, defined as $\eta = -\ln \tan(\theta/2)$, which is invariant under Lorentz transforms in the massless approximation. Together, z, ϕ, and η form the coordinate system for the CDF detector. Distance between two objects is defined as $\Delta R = \sqrt{(\Delta\phi)^2 + (\Delta\eta)^2}$ A schematic of the detector is shown in figure 3.3 [20, 21].

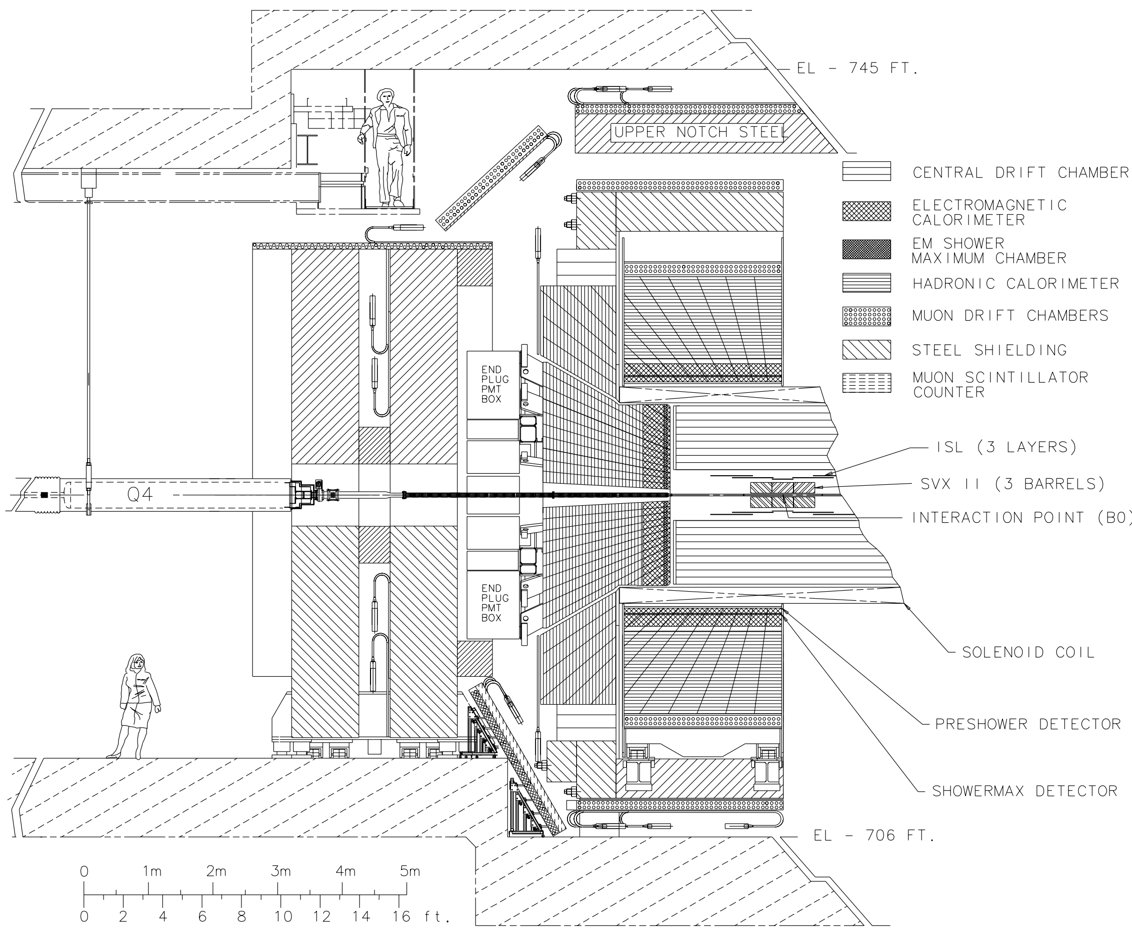

FIGURE 3.3: CDF detector schematic [20, 21]

In order of inward to outward from the beam pipe, the CDF detector has the following parts:

- Cerenkov Luminosity Counter (CLC) that measures instantaneous luminosity.

- Silicon Vertex Detector (SVX) that provides tracking of charged particles near the interaction point.
- Central Outer Tracker (COT) drift chamber consisting of drift wires in a strong (1.4 T) magnetic field to measure momenta and charge.
- Electromagnetic calorimeter to measure energy deposition from objects like electrons and photons.
- Hadronic calorimeter to measure energy deposition from protons, pions and other hadrons.
- Muon detector measures muons, which are assumed to pass through the other detectors essentially unaffected.

All parts that make up the tracking volume are shown in figure 3.4.

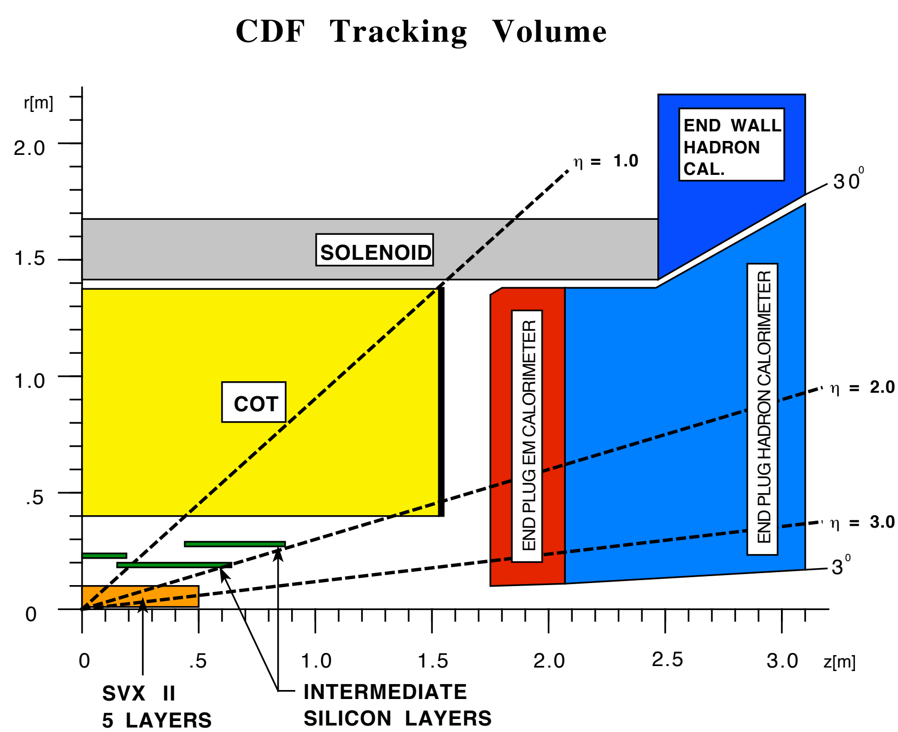

FIGURE 3.4: CDF Tracking Volume

3.2.1 Cerenkov Luminosity Counter

The Cerenkov Luminosity Counter is used to measure instantaneous luminosity. It is placed very close to the beam line, at $3.7 < |\eta| < 4.7$ [20, 22, 23]. Since acceleration of charged particles produces Cerenkov radiation, the CLC measures the amount of Cerenkov radiation produced, thereby measuring the number of p and $\bar{p}$ in every bunch. The relation used is

$$\mu f_{\mathrm{BC}} = \sigma_{\mathrm{inelastic}} \mathscr{L} \tag{3.2}$$

where μ is the average number of p, $\bar{p}$ interactions per bunch crossing, f_{BC} is the bunch crossing rate, and $\sigma_{\mathrm{inelastic}}$ is the inelastic cross section of the beam. Knowing the other three variables allows us to solve for $\mathscr{L}$, the instantaneous luminosity.

3.2.2 Silicon Tracking

Many particles produced in $p, \bar{p}$ collisions are very short lived. Physics analyses often require these short lived particles be detected before they decay. The silicon tracking system [24, 25] is located closest to the beam pipe and provides high precision measurement of position and momentum for particles from the collision. In the case of the ZH analysis, the b quarks from the Higgs boson are measured using the silicon detector.

A voltage is applied across the silicon detector to strip out the excess electrons. When an ionizing particle from a collision passes through the silicon, it ionizes the silicon, causing a buildup of charge at the terminal, which is then measured. The position of the wires that carried the current to the terminal allows the location of the particle to be inferred and the timing of successive hits allows a path to be reconstructed for the particle.

The silicon detector is broken into the Silicon Vertex (SVXII) detector and the intermediate silicon layers (ISL). The SVXII detector has three concentric barrels. Silicon strips are mounted on the inner and outer surfaces of the barrels. Additionally, there is a silicon strip mounted directly on the beampipe, which is called Layer 00 (L00). Outside the SVXII, the ISL is another cylindrical detector that extends silicon coverage to $|\eta| = 2.0$, as shown in figure 3.4. The barrel structure of the SVX detector is shown in figure 3.5. The total SVX detector has 722,432 channels.

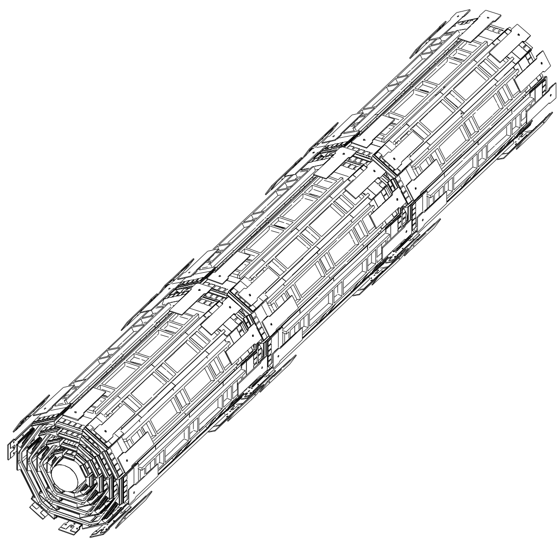

FIGURE 3.5: Silicon detector barrel structure

3.2.3 *Central Outer Tracker*

The Central Outer Tracker [26] (COT) is another, much larger tracking volume that extends from 0.43 m to 1.32 m radially and from -1.5 m to $+1.5$ m along the beam direction. The chamber is filled with a low pressure mixture of argon and ethane and contains 8 "superlayers", each of which contains 12 wire layers for a total of 96 layers. When a particle goes through the chamber, it ionizes the gas, leading to free electrons being attracted to the sensing wires which are then measured. The superlayers alternate as axial superlayers (measure $R-\phi$) and sterial superlayers (measure ϕ). The fine resolution of the wires in the drift chamber allow a transverse momentum resolution of 0.15%. Combined with silicon, the resolution is 0.07%. In order to measure the the charge of a particle, the solenoid around the COT applies a 1.4 T magnetic field, which causes the path of the particle to curl, allowing the charge to be inferred when the mass is known.

3.2.4 Calorimeters

The electromagnetic and hadronic calorimeters sit outside the solenoid. They are divided into central ($|\eta| < 1.1$) [27, 28] and plug ($1.1 < |\eta| < 3.6$) [29]. The EM calorimeter absorbs energy from electrons and photons, whereas the hadronic calorimeter absorbs energy from particles not absorbed in the EM calorimeter (not including muons).

The calorimeters are composed of alternating layers of scintillator and metal. Particles passing through the calorimeter interact with the dense materials and produce a shower of particles that are detected as photons in the scintillator photomultiplier tubes. The em calorimeter metal is lead and the hadronic calorimeter metal is iron. The towers are segmented into 15 degree wedges in ϕ and 0.1 in η. In the plug region, ϕ segmentation is 7.5 degree wedges until $\eta = 2.11$, after which again the wedges in ϕ are 15 degrees. Together the scintillator and metal in the calorimeters form six radiation lengths of material, which would be expected to trap 99.8% of the energy of interacting particles passing through the scintillator on average.

3.2.5 Muon Detectors

The muon detectors are located outside all other detectors because the muons are long lived and and do not strongly interact with the calorimeter. The detectors are single wire drift chambers, and cover most of the space where $|\eta| < 1.0$. There are three parts to the muon detectors, the central muon detector (CMU), the central muon upgrade (CMP), and the central muon extension (CMX). The CMP is an additional layer of drift chamber outside the CMU. The coverage is shown in figure 3.6.

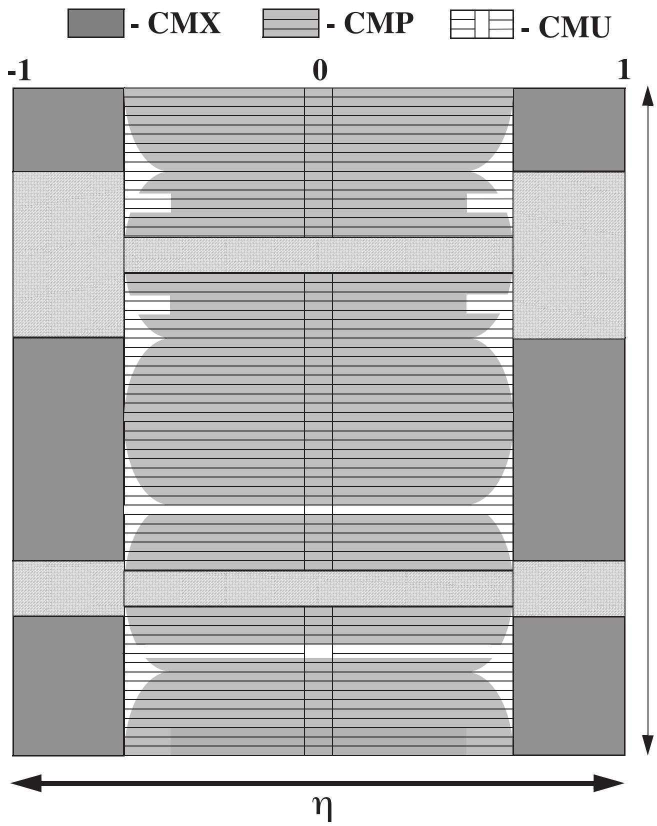

FIGURE 3.6: Muon detector coverage

3.3 CDF Software

The CDF detector is an amazingly complex machine, with many different interoperating systems. To extract maximum sensitivity for a physics analysis, all the components must function as a whole to reconstruct particles and trajectories from hits on wires. This requires a combination of hardware and software to isolate interesting events for analysis and reconstruct the particle content of the events.

3.3.1 Event Triggers

Collisions occur at a rate of approximately 2.5 MHz. Storing all the hits and raw detector level information for an event is approximately 200 KB. That translates to a raw data rate of nearly 500 GB/s, which was well beyond the reach of computing when the

CDF detector was constructed and upgraded, even if it may be feasible soon. Coupled with the fact that most $p\bar{p}$ collisions result in some sort of elastic scattering, which are not terribly interesting from a physics perspective, we know events must be discarded.

The system for deciding what events to keep is called triggering. At CDF, there are three levels of event triggers. Each one successively applies more stringent criteria. If an event passes all three triggers, it is recorded to a permanent storage medium.

The Level 1 trigger (L1) is purely hardware based and it uses calorimeter information, tracks reconstructed in the COT with the eXtremely Fast Tracker (XFT)[30] algorithm, and muon chamber stubs to make a decision. The specialized hardware nature of the trigger and simplistic algorithm ensures fast rejection, allowing the event rate to be reduced from approximately 2.5 MHz to 20 kHz.

The Level 2 trigger (L2) has better (but slower) resolution and identification algorithms. It also considers tracking information from silicon, allowing better rejection of unwanted events. It reduces the event rate from 20 kHz to 300 Hz.

The Level 3 trigger (L3) is entirely in software and is performed by a computing cluster. It takes raw detector output, reconstructs higher level objects, clustered calorimeter energies, and sophisticated reconstructed tracking from both COT and silicon as inputs. It reduces the event rate from 300 Hz to 75 Hz, after which the events are written to permanent storage.

3.3.2 Lepton Identification

The ZH analysis depends on accurate measurement of charged leptons, e, μ (τ does not have sufficient acceptance to contribute to the result at this luminosity). These two charged leptons are relatively easy to measure in the CDF detector, as they leave tracks in the COT and do not shower like gluons and quarks. The following quantities are used in selection of electrons and muons (see chapter 4).

Electron Quantities

- E_T - Transverse energy – the energy deposited in the calorimeters. For electrons, at most two towers (neighboring in η) are allowed.

- p_T - Transverse momentum – the momentum of the electron as measured in the COT tracking detector.

- Had/EM - The ratio of energy deposited in the hadronic to the energy deposited in the em calorimeters. Electrons mostly deposit in the em calorimeter, so this should be low.

- L_{shr} - This indicates the agreement of the electron with the expected lateral shower profile.

- $|\Delta x|$ and $|\Delta z|$ - Separation between COT track position and shower position.

- E/P - Ratio of calorimeter energy to momentum from the COT. May deviate from unity because of bremsstrahlung.

- Isolation - Ratio of energy deposited outside a cone of $\Delta R = 0.4$ from the center of the electron cluster. If a lepton is produced as part of a jet, this is low, and from a Z boson, this is high.

- χ^2_{strip} - Comparison of shower profile to expected profile.

Muon Quantities

- p_T - Transverse momentum – the momentum of the muon as measured in the COT tracking detector.

- $|\Delta x|$ and $|\Delta z|$ - Separation between COT track position and the object seen in the muon chambers.

- $E_{\text{em,hadronic}}$ must be low for a muon as they do not deposit much energy in the calorimeters.

- Isolation - Ratio of energy deposited outside a cone of $\Delta R = 0.4$ from the center of the muon cluster. If a lepton is produced as part of a jet, this is low, and from a Z boson, this is high.

3.3.3 Jet Modeling and Reconstruction

By the principle of confinement, QCD requires that objects with nonzero color charge cannot exist outside of a bound state. This means that in high energy collisions, any high p_T quarks or gluons (which carry color charge) must *hadronize*, or turn into a set of hadrons that are colorless. To do this, the energy of the original quark or gluon causes pair production of new quarks from the vacuum. This process repeats until the newly produced items can form colorless bound states. Typically, a high energy quark hadronizes into a stream of 10-30 particles, collectively referred to as a jet.

In the CDF detector reconstruction, jets are found by the JetCLU [31] algorithm, which operates by iteratively calculating the centroid of energy deposition in the calorimeter towers until the centroid no longer changes. These raw jet energies are corrected to account for

- Nonuniform calorimeter response as a function of jet energy.

- η corrections to account for gaps in the detector

- Multiple $p, \bar{p}$ interactions at a single bunch crossing, which can happen at high luminosities.

These lead to significant scale corrections for the measured jet energy, given in figure 3.7. The uncertainty on the jet energy scale is given in figure 3.8. Since the systematic

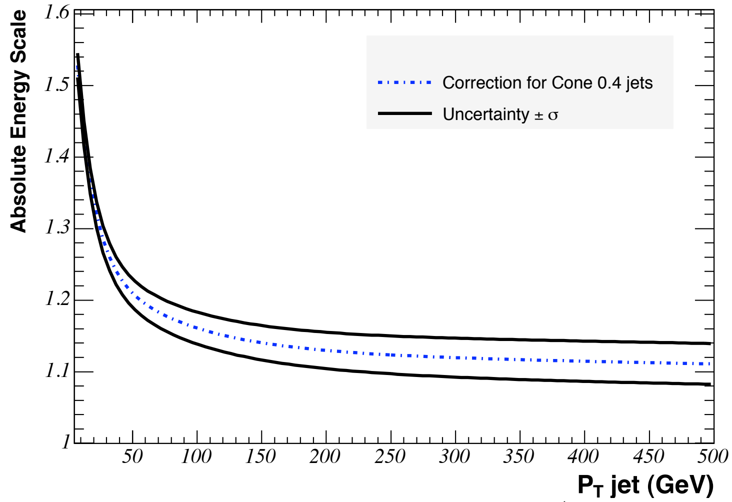

FIGURE 3.7: Jet energy scale

on the jet energy scale will affect different processes differently, this systematic must be propagated forward in the analysis. This is examined in chapter 6.

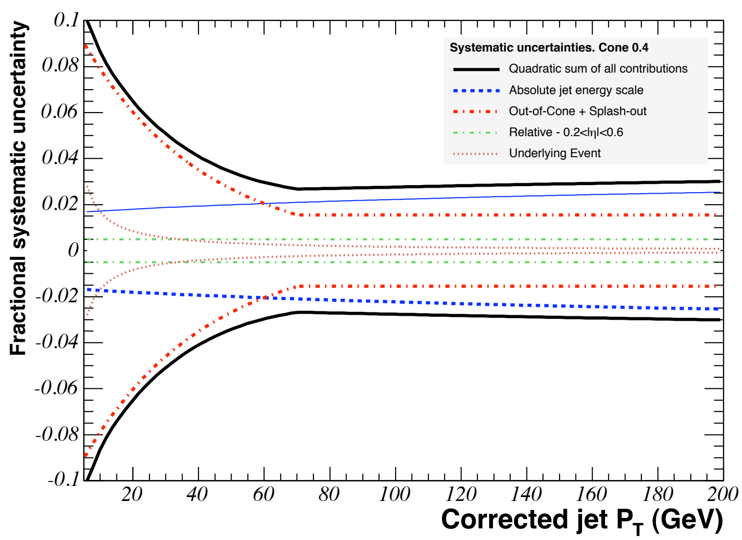

FIGURE 3.8: Jet energy scale systematic uncertainty

3.3.4 SecVtx Tagging

b quarks decay through the weak force, which requires they have long lifetimes compared to particles that decay through the strong force. The high resolution particle tracking available from the silicon vertex (SVX) detector allows detection of production of the b quark at the primary interaction vertex, a short track ($\sim \mathcal{O}(10\ mm)$) and a secondary decay to other particles. The SECVTX (Secondary Vertex) algorithm looks for a vertex displaced from the main vertex in the silicon detector. Tracks where this displacement is found are then matched with jets within a $\Delta R = 0.4$ cone, allowing a jet to be tagged as coming from a b quark. Two different sets of criteria (loose and tight) are possible, and both are used in the ZH analysis (see chapter 4). Approximately 45% of b quarks meet loose criteria and 35% of b quarks meet tight criteria at a jet E_T of 30 GeV.

4

Event Selection

While the $ZH \rightarrow l^+l^-b\bar{b}$ channel has a low cross section $\times$ branching ratio (see figures 2.14 and 2.16) compared to other SM Higgs searches, it has significantly lower background. This is mainly caused by the requirement for two high p_T, visible, opposite sign electrons or muons, which are rare in $p\bar{p}$ collisions. Additionally, unlike the $WH \rightarrow l\nu b\bar{b}$ channel or $ZH \rightarrow \nu\bar{\nu}b\bar{b}$ channel, all final products are directly measured, decreasing the chance of fake backgrounds due to mismeasurement of missing E_T.

We select $q\bar{q} \rightarrow ZH \rightarrow l^+l^-b\bar{b}$ candidates by requiring (i) high-p_T lepton trigger, (ii) two leptons each with $p_T > 20\ GeV/c$ and a dilepton invariant mass in the Z mass window, $76\ GeV/c^2 < M_{ll} < 106\ GeV/c^2$ (iii) two cone-0.4 jets with $E_T > 15\ GeV$, one of which has $E_T > 25\ GeV/c^2$, and (iv) 2 loose SECVTX b-tags or exclusively 1 tight SECVTX b-tag. These requirements are summarized in table 4.1.

This selection was designed for the $ZH \rightarrow l^+l^-b\bar{b}$ neural network analysis at CDF. Results with 1 fb^{-1} of data using the same selection are published in [32]. A description of selection and trigger requirements follows.

A central lepton trigger
One high E_T central lepton with 'tight' requirements
A second high E_T lepton of the same flavor with the opposite sign
Z boson mass window of 76 GeV/c^2 to 106 GeV/c^2
Two or more jets with $E_T > 15$ GeV and $\lvert\eta\rvert < 2$
One or more jets with $E_T > 25$ GeV
Either: 2 'loose' b-tags or 1 'tight' b-tag

Table 4.1: Summary of Event Criteria

4.1 Event Criteria

In $p\bar{p}$ collisions, the interacting particles are the quarks and gluons that compose the protons. Since the coupling of quarks to the strong force is much higher than the coupling to the electroweak force, the dominant product of interaction is hadronic. Since we seek to reduce this large hadronic background, we search for a high p_T lepton using the CDF central high p_T lepton trigger [33]. These are summarized in tables 4.2 and 4.3.

Trigger	Central Electron
Level 1	Central Calorimeter $E_T \geq 8$ GeV XFT $p_T \geq 8.34$ GeV/c Had/EM < 0.125
Level 2	L2 $E_T \geq 16$ GeV L2 Had/EM ≤ 0.125 $\lvert\eta\rvert < 1.317$
Level 3	Central $E_T > 18$ GeV Central Had/EM < 0.125 Central $\Delta z \leq 2$ cm Track $p_T > 9$ GeV/c

Table 4.2: Central electron trigger path

The central electron trigger looks for energy in an EM calorimeter tower with a corresponding XFT track. At level 2, there must be a EM tower with $E_T > 8$ GeV and nearby towers must sum up to $E_T > 16$ GeV. At level 3, there must be a corresponding track with $p_T > 9$ GeV/c and $\Delta z \leq 2$ cm. The minimum E_T is 18 GeV, but because

Trigger	CMUP	CMX
Level 1	CMU stub $p_T \geq 6\ GeV/c$ XFT $p_T \geq 4.09\ GeV/c$ CMP Stub	CMU stub $p_T \geq 6\ GeV/c$ XFT $p_T \geq 8.34\ GeV/c$
Level 2	XFT $p_T \geq 14.77\ GeV/c$	XFT $p_T \geq 14.77\ GeV/c$
Level 3	XFT $p_T \geq 18.0\ GeV/c$ CMP $\Delta X < 20$ CMU $\Delta X < 10$	XFT $p_T \geq 18.0\ GeV/c$ CMX $\Delta X < 10$

Table 4.3: Central muon trigger paths

of trigger turn on effects, we only consider electrons above 20 GeV.

Muons have two triggers, CMUP and CMX, corresponding to the parts of the muon detector. The CMUP trigger requires aligned muon hits in CMU and CMP, whereas the CMX trigger only requires hits in the CMX. A corresponding XFT track is also required.

Lepton η and ϕ also affect the trigger efficiency. For $ZH \rightarrow l^+l^-b\bar{b}$, 60% of events where the Z decays to electrons are triggered by CEM, and 50% of events where the Z decays to muons are triggered by the CMUP and CMX triggers combined [34].

Since this is a search, it is critical to maximize acceptance for ZH signal. To that effect, we use a lepton selection looser than the standard CDF selection [33] [35]. At least one of the two leptons must meet the tight lepton requirements, however the other can meet the looser requirements defined below in table 4.4 for electrons and 4.5 for muons. Together the two leptons must have an invariant mass between 76 and 106 GeV/c^2.

4.1.1 Jets

Figure 2.16 tells us that a low mass Higgs boson decays to $b\bar{b}$ most of the time. QCD requires the b quarks hadronize into jets, which are then measured in the calorimeter. Kinematics favor b quarks with high transverse momentum because the Higgs is so massive compared to the b quark. Figure 4.1 shows that the leading b quark almost always

Tight Electron Selection	Loose Electron Selection
$E_T > 18\ GeV$ $p_T > 9\ GeV/c$ Had/Em $< 0.055 + 0.0004{\cdot}$E $E/P < 2.5 + 0.015E_T$ $\lvert Z_{\text{vertex}}\rvert < 60$ cm $\lvert\eta\rvert < 1$ $L_{\text{shr}} < 0.2$ Isolation $\cdot E_T^{\text{raw}}/E_T^{\text{corr}} < 0.1$ $-3.0 < Q \cdot \lvert\Delta x\rvert < 1.5$ $\chi^2_{\text{strip}} < 25.0$ $\lvert Z_{\text{electron}} - Z_{\text{vertex}}\rvert < 3$ cm 2 stereo and 2 axial super-layer segments	$E_T > 10\ GeV$ (central) $E_T > 18\ GeV$ (plug) Had/Em $< 0.055 + 0.00045{\cdot}$E Isolation $\cdot E_T^{\text{raw}}/E_T^{\text{corr}} < 0.1$ $p_T > 5\ GeV/c$ (if central) $\lvert Z_{\text{vertex}}\rvert < 60$ cm Fiducial

Table 4.4: Electron requirements

Tight Muon Selection ($p_T > 20\ GeV/c$)	Loose Muon Selection ($p_T \leq 20\ GeV/c$)	Loose Muon Selection ($p_T > 20\ GeV/c$)
Had Energy $< 6\ GeV$ Em Energy $< 2\ GeV$ Isolation < 0.1 $d_0 < 0.2$ (w/ silicon hits) $d_0 < 0.02$ (w/o silicon hits) ≥ 3 sterial segments ≥ 3 axial segments	Had Energy $< 6\ GeV$ Em Energy $< 2\ GeV$ Isolation < 0.1 $d_0 < 0.2$ (w/ silicon hits) $d_0 < 0.02$ (w/o silicon hits) ≥ 1 COT segment	Had Energy $< 12\ GeV$ Em Energy $< 4\ GeV$ Isolation < 0.1 ≥ 1 COT segment
Tight CMUP requirements $\lvert\Delta x\rvert_{CMU} < 3.0$ cm $\lvert\Delta x\rvert_{CMP} < 5.0$ cm		
Tight CMX requirements $\lvert\Delta x\rvert_{CMX} < 6.0$ cm $\rho > 140$ cm		

Table 4.5: Muon requirements. Any of the three sets of criteria can be satisfied. Loose muons are not required to have muon detector stubs.

has p_T over 25 GeV/c and the second b quark almost always has p_T over 15 GeV/c. Setting the jet cuts at those values reduces significant background while maintaining most of the signal.

We choose to use $\Delta R = 0.4$ cone jets, meaning the distance in the η, ϕ plane ($\Delta R = \sqrt{\Delta\phi^2 + \Delta\eta^2}$) is 0.4. This is used when finding the bounds of the jet in the reconstruction software. Larger cones allow capture of more of the partons that make up a jet at the expense of more noise.

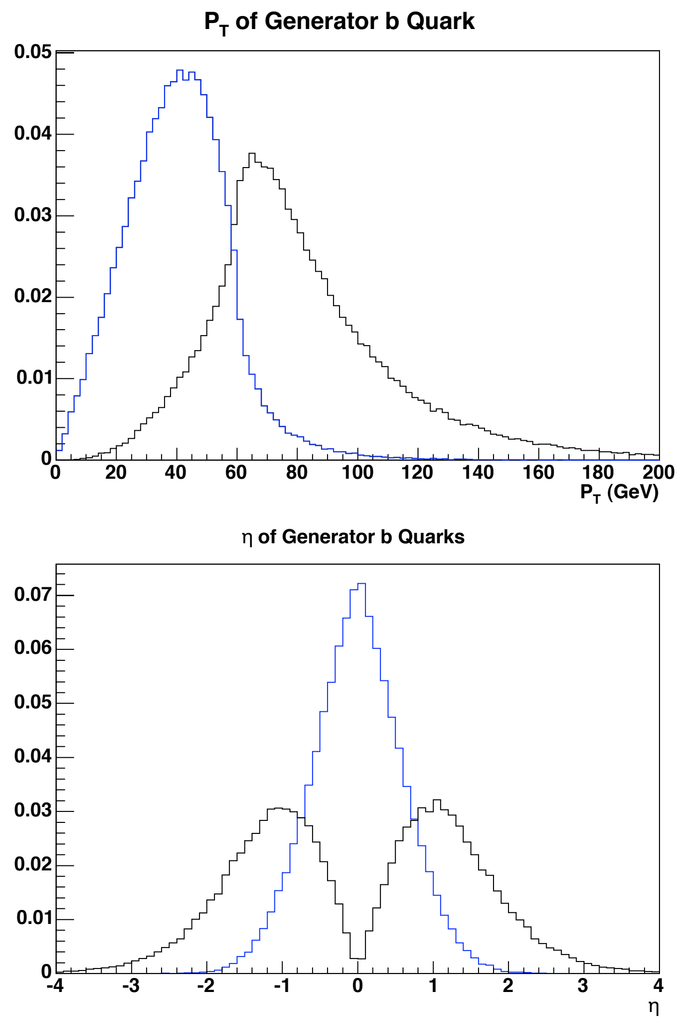

FIGURE 4.1: *ZH* Higgs decay *b*-quark kinematics. Transverse momenta (top) and η (bottom) of the two *b* quarks produced [34]

4.1.2 b-Tagging

Higgs events are sometimes hard to separate from Drell-Yan events based on kinematics alone. However, the Higgs boson strongly favors decay to $b\bar{b}$ over other hadronic decays. By searching for this b quark signature, we greatly enhance sensitivity to signal.

We use the SECVTX b-tagging algorithm [36], which uses the Silicon detector to look for a secondary vertex in the event since b quarks have such a short lifetime.

We separate events into two categories, those with two 'loose' b-tags, and those with one or more b-tags, preferring to classify an event as two loose if both criteria are satisfied. The signal and background partition into the two categories differently, leading to a higher signal to background ratio in the two loose tag channel. This fact is later used to enhance sensitivity (see chapter 6).

b-tags are very good at reducing Drell-Yan background. Requiring a b-tag cuts $\sim$ 98% of light flavor backgrounds and $\sim$ 80% of heavy flavor backgrounds. Fakes, which are essentially similar to Drell-Yan kinematically, with a lepton faked by a jet achieve similar reduction factors. In contrast, ZH is reduced by only 35% by the b-tag requirement, dramatically improving the signal to background ratio.

4.2 Backgrounds

The selection must be balanced between cutting out background while maintaining sufficient signal acceptance. This leads to three large backgrounds to be accounted for: Drell-Yan (Z + jets), $t\bar{t}$ pair production, and diboson ($WW/WZ/ZZ$) production, shown in figure 4.2 and 4.3.

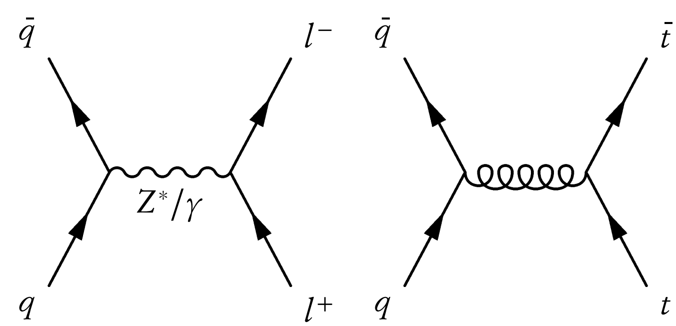

FIGURE 4.2: Tree level diagrams for the Drell-Yan and $t\bar{t}$ background processes

The Drell-Yan background events typically have two jets that are not from the primary $q\bar{q} \rightarrow l^+l^-$ interaction. There are many sources for the extra jets, but the most common sources are a radiated gluon that hadronized or interactions between other quarks in the collision. This produces the requisite two jet, two lepton signature that passes our selection.

The $t\bar{t}$ pair production has a $\sim$ 100% branching ratio to $WWbb$. Both W bosons can decay hadronically or leptonically. In the case where both decay leptonically, the final state is $l^+l^-\nu\bar{\nu}b\bar{b}$. Since the neutrinos are practically invisible, the observed state is the same as our selection, except with high missing transverse energy.

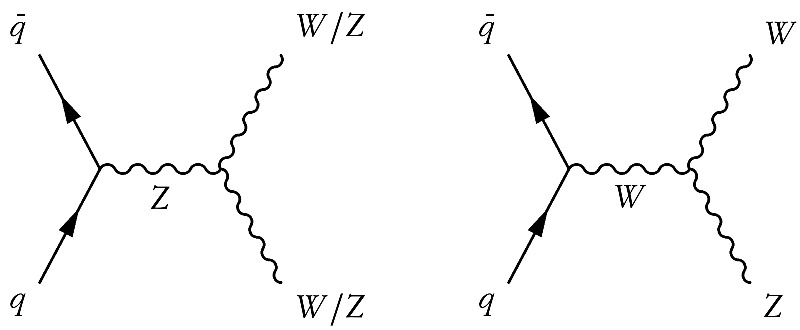

FIGURE 4.3: Tree level diagrams for the diboson $WW/WZ/ZZ$ processes

The diboson production usually occurs one of two ways. Either $q\bar{q}$ can annihilate to a Z, which pair produces W or Z. Or $q\bar{q}$ produces a W, which radiates a Z. The net result is a final state of $WW/WZ/ZZ$. The WW can decay to $l^+l^-\nu\bar{\nu}b\bar{b}$ with a small branching ratio, but the combination of requiring the reconstructed dilepton mass to be in the Z mass window and a bTag reduces the acceptance on this background to effectively zero. For similar reasons, WZ also has very low acceptance, approximately 1.0 event out of 315 events expected. However ZZ can have one Z decay hadronically to $b\bar{b}$ and the other to l^+l^-. Kinematically, ZZ is very similar to ZH with the exception of the reconstructed dijet mass distribution. This makes it difficult to separate from ZH and consequently significant amounts of ZZ are allowed into the selection. The

$WW/WZ/ZZ$ category in tables 4.9-4.8 is 92% ZZ and 8% WZ after tag requirements.

4.3 Signal Acceptance

Figure 2.14 gives ZH production cross sections at the Tevatron, and figure 2.16 gives Higgs boson branching ratios. The Feynman diagram for the production process is shown as figure 4.4. With 2.7 fb^{-1} of collected data, based on ALPGEN [37] Monte Carlo and the effects of trigger and selection efficiencies we expect events as shown in table 4.6.

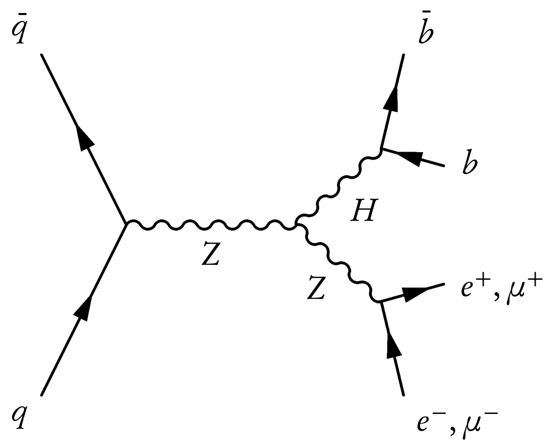

FIGURE 4.4: $ZH \to l^+ l^- b\bar{b}$ production mechanism

M_H	σ (fb)	$BR(H \to b\bar{b})$	Pretag	1 Tight	2 Loose
100	169.0	0.803	4.52	1.97	0.96
105	145.0	0.785	4.12	1.81	0.93
110	125.0	0.758	3.23	1.41	0.71
115	107.9	0.716	2.88	1.25	0.65
120	93.7	0.659	2.60	1.13	0.58
125	81.6	0.587	1.79	0.79	0.42
130	71.2	0.502	1.31	0.57	0.31
135	62.4	0.410	0.93	0.45	0.25
140	54.8	0.319	0.68	0.31	0.17
145	48.2	0.235	0.44	0.21	0.12
150	37.6	0.160	0.28	0.12	0.07

Table 4.6: Expected number of $ZH \to l^+l^-b\bar{b}$ events for Higgs masses (in GeV/c^2) between 100 and 150 in the two loose b-tag and one tight b-tag channels. Pretag indicates all selection requirements except b-tagging.

4.4 Event Totals

4.4.1 Pretag

Source	ee	mm	ll
$Z \to ee$	3768.54 ± 986.85	0.00 ± 0.00	3768.54 ± 986.85
$Z \to ee + \mathrm{hf}$	391.71 ± 68.15	0.00 ± 0.00	391.71 ± 68.15
$Z \to \mu\mu$	0.04 ± 0.01	2685.53 ± 681.26	2685.57 ± 681.26
$Z \to \mu\mu + \mathrm{hf}$	0.00 ± 0.00	263.07 ± 45.68	263.07 ± 45.68
$Z \to \tau\tau$	3.07 ± 0.63	0.66 ± 0.13	3.73 ± 0.65
$Z \to \tau\tau + \mathrm{hf}$	0.15 ± 0.04	0.01 ± 0.00	0.16 ± 0.04
WW, WZ, ZZ	91.76 ± 12.73	65.87 ± 9.16	157.62 ± 15.69
Fakes	640.28 ± 111.30	35.80 ± 13.61	676.08 ± 112.12
tt	19.13 ± 3.83	14.86 ± 2.97	33.99 ± 4.85
Total	4916.33 ± 995.44	3067.02 ± 683.00	7986.35 ± 1207.22
Data	4297	2960	7257

Table 4.7: Pretag background expectation

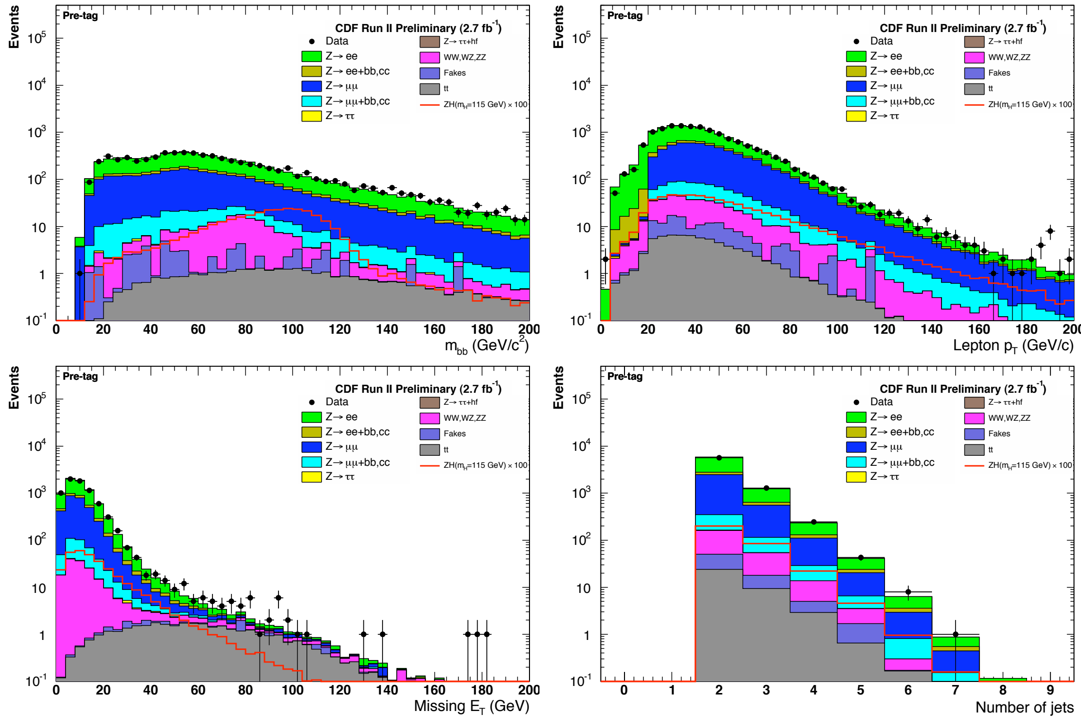

4.4.2 Double Loose b-Tag

Source	ee	$\mu\mu$	ll
$Z \to ee$	2.93 ± 0.73	0.00 ± 0.00	2.93 ± 0.73
$Z \to ee + \text{hf}$	11.39 ± 2.76	0.00 ± 0.00	11.39 ± 2.76
$Z \to \mu\mu$	0.00 ± 0.00	2.55 ± 0.61	2.55 ± 0.61
$Z \to \mu\mu + \text{hf}$	0.00 ± 0.00	8.12 ± 1.93	8.12 ± 1.93
$Z \to \tau\tau$	0.00 ± 0.00	0.00 ± 0.00	0.00 ± 0.00
$Z \to \tau\tau + \text{hf}$	0.00 ± 0.00	0.00 ± 0.00	0.00 ± 0.00
WW, WZ, ZZ	1.69 ± 0.33	1.24 ± 0.24	2.94 ± 0.41
Fakes	0.03 ± 0.01	0.02 ± 0.01	0.04 ± 0.01
$t\bar{t}$	4.38 ± 0.88	3.29 ± 0.66	7.66 ± 1.09
Total	20.42 ± 3.01	15.21 ± 2.14	35.63 ± 3.69
Data	16	16	32

Table 4.8: Double bTag background expectation

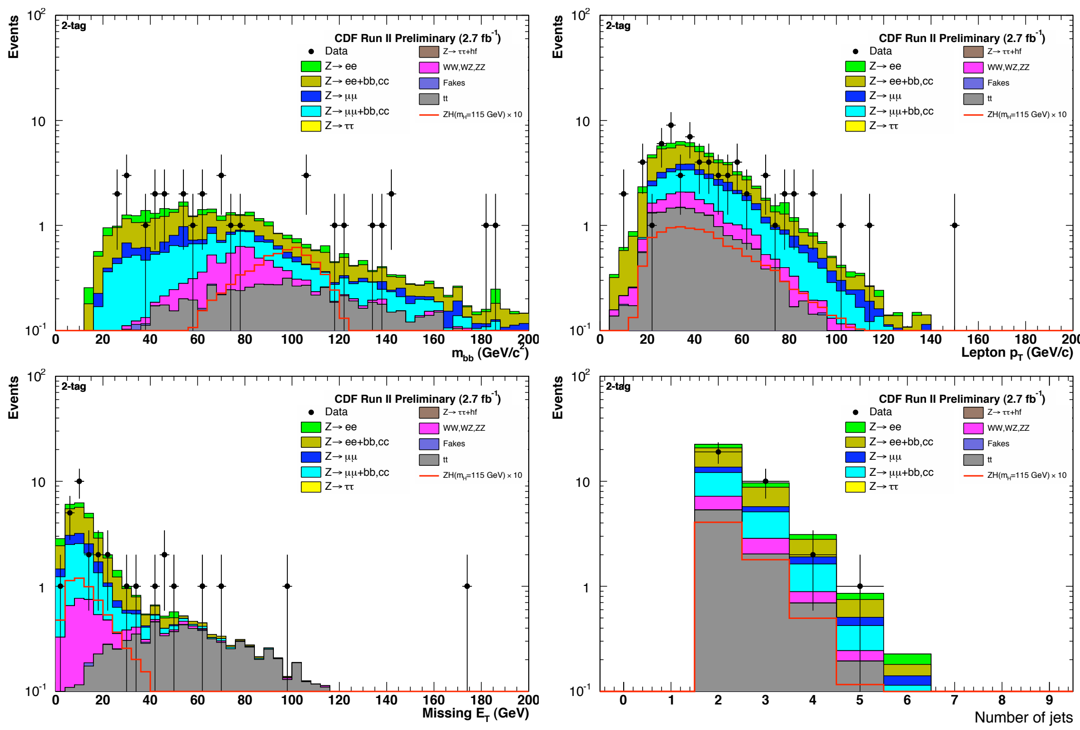

4.4.3 Single Tight b-Tag

Source	ee	$\mu\mu$	ll
$Z \to ee$	70.67 ± 18.84	0.00 ± 0.00	70.67 ± 18.84
$Z \to ee + \text{hf}$	63.03 ± 11.43	0.00 ± 0.00	63.03 ± 11.43
$Z \to \mu\mu$	0.00 ± 0.00	58.89 ± 14.89	58.89 ± 14.89
$Z \to \mu\mu + \text{hf}$	0.00 ± 0.00	44.21 ± 8.14	44.21 ± 8.14
$Z \to \tau\tau$	0.05 ± 0.02	0.02 ± 0.01	0.07 ± 0.02
$Z \to \tau\tau + \text{hf}$	0.04 ± 0.01	0.01 ± 0.00	0.04 ± 0.01
WW, WZ, ZZ	6.64 ± 1.04	4.97 ± 0.79	11.61 ± 1.30
Fakes	12.80 ± 6.40	3.09 ± 1.55	15.89 ± 6.58
$t\bar{t}$	7.71 ± 1.54	6.15 ± 1.23	13.86 ± 1.97
Total	160.94 ± 23.15	117.34 ± 17.10	278.28 ± 28.78
Data	152	106	258

Table 4.9: Single bTag background expectation

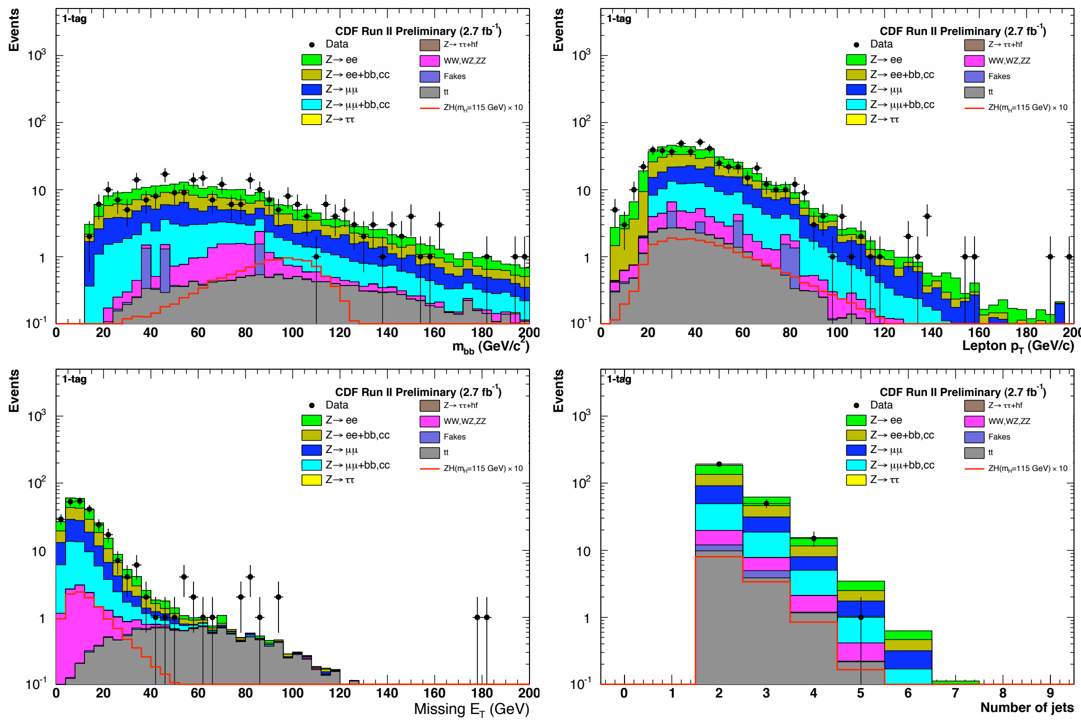
1-tag
CDF Run II Preliminary (2.7 fb^{-1})
Data
Z→ ee
Z→ ee+bb,cc
Z→ μμ
Z→ μμ+bb,cc
Z→ ττ
Z→ ττ+hf
WW,WZ,ZZ
Fakes
tt
ZH(m$_H$=115 GeV) x 10
Events
m$_{bb}$ (GeV/c^2)
Lepton p$_T$ (GeV/c)
Missing E$_T$ (GeV)
Number of jets

5

Matrix Elements

Perturbation theory allows calculation of transition probabilities between quantum states. Since the standard model is a perturbative theory, in an ideal world, the probability of a transition between the initial state $p\bar{p}$ and the final measured partons would be calculable. In the real world, many specifics about the initial and final states are unknowable. But, by integrating over unknown quantities and making a few assumptions, an analogous probability can be obtained. If we call the complete set of measured event kinematics $\mathbf{x}$, and the set of physics parameters (particle masses, couplings, etc.) used to perform the calculation $\boldsymbol{\Theta}$, the probability density function P_j of the j^{th} process is proportional to the differential cross section in equation 5.1.

$$P_j(\mathbf{x}|\boldsymbol{\Theta}) = \frac{1}{\sigma(\boldsymbol{\Theta})}\frac{d\sigma(\boldsymbol{\Theta})}{d\mathbf{x}} \tag{5.1}$$

5.1 Matrix Element Approximations

Without any approximations, if the initial and final states could be known exactly (including quantum numbers that are unknowable like color), the differential cross section would simply be the matrix element transition probability calculated using perturbation theory.

$$\frac{d\sigma(\boldsymbol{\Theta})}{dp_i dp_f} = \left|\mathscr{M}_j(p_i, p_f|\boldsymbol{\Theta})\right|^2 \tag{5.2}$$

Since there is a great deal we do not know about the initial and final states of the we must make the following approximations

5.1.1 *Initial State*

From detector construction we know the collision is between a proton and an anti-proton. Since protons and anti-protons are composite particles, the actual interaction occurs between the constituents of the protons, the quarks and gluons. Unfortunately we do not know the exact kinematics of the quarks and gluons. We also do not know color and spin configurations of the colliding particles. We do not even know if the interacting particles were quarks or if they were gluons; we only know that we collided p with $\bar{p}$.

To account for this broad lack of knowledge of the initial state, we use a parton density function (PDF) from the CTEQ group [38], version 6.1, which is a parametrization of the momenta of the components of a proton. We integrate over the parton density functions for both the p and $\bar{p}$. This removes the dependence on p_i in both the $\mathscr{M}$ and the differential cross section, leading to a new differential cross section.

$$\frac{d\sigma(\boldsymbol{\Theta})}{dp_f} = \int d\Phi \left|\mathscr{M}_j(p_i, p_f|\boldsymbol{\Theta})\right|^2 f_{\mathrm{PDF}}(p_1) f_{\mathrm{PDF}}(p_2) \tag{5.3}$$

where f_{PDF} is the parton density function, applied twice for both initial state partons. Because the PDF returns a probability of measuring a momenta (given some collider and theory parameters), it allows integration over all accessible regions of the 4-momentum for initial state particles. Usually initial state particles are not virtual, which reduces the dimension of integration by one.

5.1.2 Final State

QCD confinement makes it impossible to measure color, spin, or momentum of the actual final state quarks. The quarks hadronize into jets which loosely resemble the original quark. In the case of backgrounds, there can be jets from gluons which hadronize as well. Additionally all of the final state partons measured variables are affected by limited detector resolution and granularity.

To account for this we introduce the *transfer functions* $W(p_f, \mathbf{x})$. Each transfer function links a final state parton to the corresponding measured reconstructed object. Since there are a range of parton momenta that can result in the measured value, this implies an integration over final parton momenta. Changing variables for the differential cross section and including the additional integrations in $d\Phi$, equation 5.3 becomes

$$\frac{d\sigma(\mathbf{\Theta})}{d\mathbf{x}} = \int d\Phi \left|\mathcal{M}_j(p_i, p_f|\mathbf{\Theta})\right|^2 \left[\prod W(p_f, \mathbf{x})\right] f_{\text{PDF}}(p_1) f_{\text{PDF}}(p_2) \tag{5.4}$$

We make a few simplifying assumptions about the to reduce the necessary integrations.

- Leptons are measured perfectly. This is equivalent to the lepton transfer function being a three dimensional delta function.
- Jet angles are measured perfectly, and jet energies are parametric functions of parton energy. The jet transfer functions can be expressed as

  $$\delta(\theta_{\text{jet}} - \theta_{\text{parton}})\delta(\phi_{\text{jet}} - \phi_{\text{parton}})W(E_{\text{parton}}, E_{\text{jet}})$$

  where $W(E_p, E_j)$ is the parametrized relationship between parton energy and jet energy.
- Incoming partons are massless (good approximation for light quarks), and have no transverse momentum.

- The two leading jets are b quark jets.
- Final state leptons are massless, and final state b quarks have an invariant mass of $4.7\ GeV/c^2$.

Additionally, each production process has multiple Feynman diagrams, which requires

$$\left|\mathcal{M}_j(p_i, p_f|\mathbf{\Theta})\right|^2 \rightarrow \sum_a \left|\mathcal{M}_j^{(a)}(p_i, p_f|\mathbf{\Theta})\right|^2$$

where the index a runs over the different Feynman diagrams available to a production process. At minimum, the number of incoming quark flavors and colors must be summed over. This makes the general form of the differential cross section

$$\frac{d\sigma(\mathbf{\Theta})}{d\mathbf{x}} = \int d\Phi \left[\sum_a \left|\mathcal{M}_j^{(a)}(p_i, p_f|\mathbf{\Theta})\right|^2\right] \left[\prod W(p_f, \mathbf{x})\right] f_{\mathrm{PDF}}(p_1) f_{\mathrm{PDF}}(p_2) \qquad (5.5)$$

5.2 Jet Transfer Function

As mentioned in the simplifications, the $W(E_{\text{parton}}, E_{\text{jet}})$ function links the measured jet energy to a possible parton energy E_{parton} with some probability. By integrating over all parton energies, this allows removal of the unknown parton energy from the differential cross section.

To get this transfer function we start with a Monte Carlo sample of $ZH \rightarrow l^+ l^- b\bar{b}$ events. Using the knowledge of the Monte Carlo, we eliminate jets in the final state that can be traced to initial state radiation (ISR) quarks or gluons. For b quark jets (matched to partons within a $\Delta R = 0.4$ cone), we find the parton energy E_{parton} and the Level 5 corrected [31] jet energy E_{jet}. We then perform a fit of $\delta = E_p - E_j$ with our functional form, which we take to be a double Gaussian, defined as equation 5.6 [39].

$$W_j(\delta) = \frac{1}{\sqrt{2\pi}(p_2 + p_3 p_5)} \left[\exp\left(\frac{-(\delta - p_1)^2}{2p_2^2}\right) + \exp\left(\frac{-(\delta - p_4)^2}{2p_5^2}\right)\right] \qquad (5.6)$$

where each p_i depends linearly on E_p:

$$p_i = a_i + b_i E_p \tag{5.7}$$

The fitted transfer function, has constants given in table 5.1 and figure 5.1-5.2.

p_i	a_i	b_i
p_1	-3.99 ± 0.15	-0.035 ± 0.002
p_2	2.66 ± 0.13	0.072 ± 0.001
p_3	0.652 ± 0.020	0.00 ± 0.000
p_4	0.374 ± 0.23	-0.274 ± 0.005
p_5	7.82 ± 0.20	0.092 ± 0.003

Table 5.1: Constants for the $W(E_{\text{parton}}, E_{\text{jet}})$ transfer function.

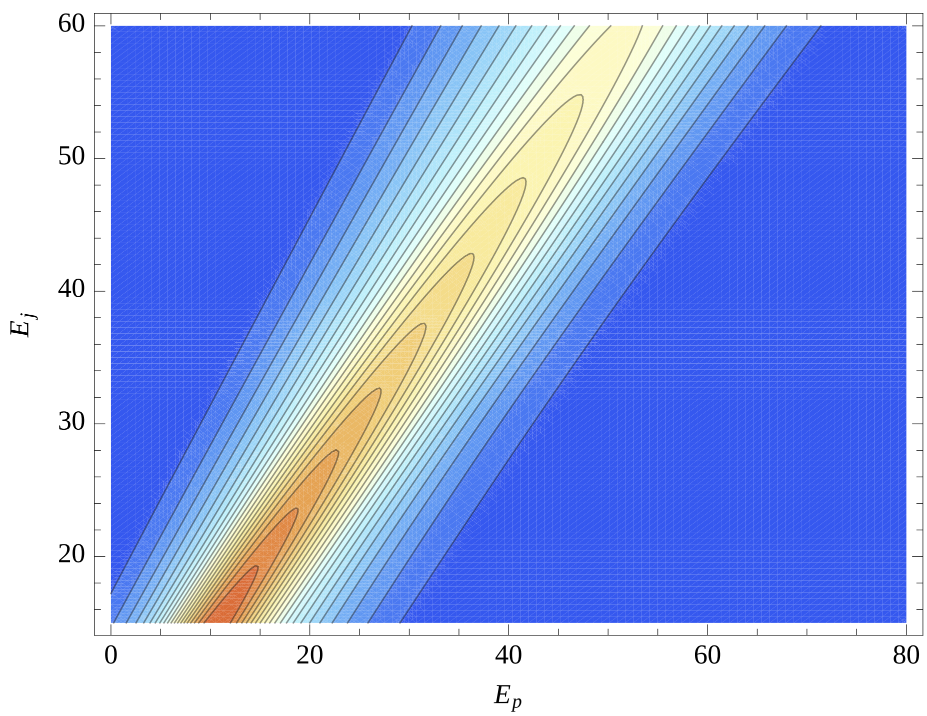

FIGURE 5.1: The parton-jet transfer function contours are shown. As expected, at low transverse energies, the jet and parton energies match to within an offset and smearing. The smearing increases as E_j and E_p increase.

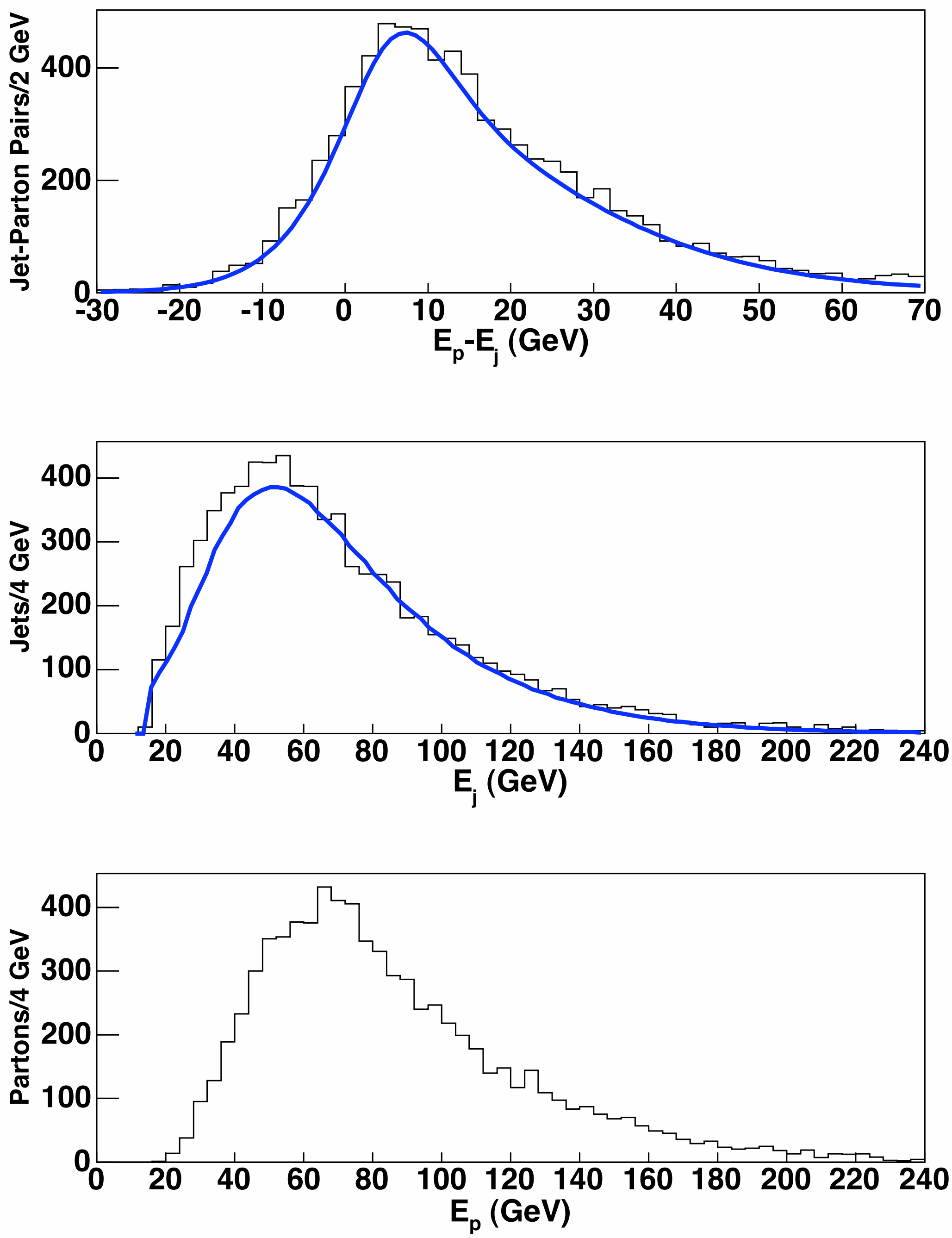

FIGURE 5.2: Fitted parton and jet spectra. The first plot shows $E_p - E_j$, which is the fitted distribution. The second shows the E_j distribution given the E_p distribution as the input distribution in the third plot.

5.3 Processes

All four matrix elements we use for the ZH search integrate over the following variables:

- Lepton momenta (x2)
- Initial parton momenta (x2)
- Final state quark momenta (x2)
- x and y components of system momenta (recoil)

To perform the integration, we use the Monte Carlo importance sampling technique VEGAS from the GNU Scientific Library (GSL) version 1.9. Although a full description of VEGAS is best left to Lepage [40], the key feature is a multi-pass iterative buildup of a sampling distribution for the integrand. Moreover, the sampling distribution is adaptive to the integrand, being determined to higher precision in regions of higher contribution to the integral. Since the sampling distribution closely follows the integrand, the variance of the points chosen by VEGAS is lower than the variance of points from a more naive approach.

A more in depth explanation of the matrix elements is presented in [39], including the variables of integration, changes of variables required and the corresponding Jacobians.

5.3.1 $ZH \rightarrow l^+l^-b\bar{b}$ and ZZ

Here we use *M*onte *C*arlo for *FeM*tobarn processes (MCFM) [41, 42] to calculate

$$\sum_a \left| \mathcal{M}_j^{(a)}(p_i, p_f|\Theta) \right|^2 \tag{5.8}$$

In addition to the integration needed for all matrix elements, there is an additional integration over the unknown intermediate Z and H bosons (see figure 2.17). We use the known Z boson mass and width and the theoretical H pole mass parameters to reduce the dimensionality of the integration.

The $ZZ \rightarrow l^+l^-b\bar{b}$ matrix element only differs from the $ZH \rightarrow l^+l^-b\bar{b}$ in terms of the kinematic distributions of the hadronic decay. The dijet mass for ZZ events will reconstruct to 91.2 GeV/c^2 instead of the Higgs boson pole mass.

5.3.2 Z+jets

We use MadEvent/MadGraph [43] to calculate $|\mathcal{M}|^2$ in the case of Z + jets. Unlike the other processes, there are many different mechanisms of Z + jets event production. At least 65 distinct mechanisms (Feynman diagrams) result in a final state of two leptons and two jets. The most common mechanism is shown in figure 5.3.

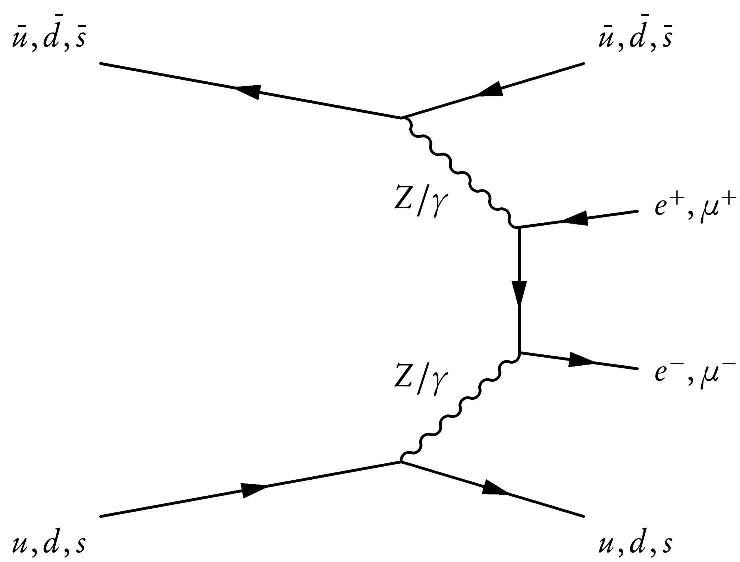

FIGURE 5.3: Z+jets dominant production mechanism

In order to carry out the integration over all the 8 specified variables for a given event, a great many evaluations ($\mathcal{O}(100,000)$) of $|\mathcal{M}|^2$ are required. Although each diagram can be evaluated fairly quickly (milliseconds), in order to achieve higher speed, MadGraph does statistical sampling of possible diagrams, choosing to weight dominant processes more heavily (several orders of magnitude faster). Unlike other processes we have matrix elements for, there is no integration over intermediate particles in the event.

5.3.3 $t\bar{t}$

We expect two neutrinos in $t\bar{t}$ events. Since they are invisible and have three degrees of freedom in the massless approximation, together they introduce six degrees of freedom that must be integrated over. The momenta of the intermediate particles, $t\bar{t}, W^{\pm}$ must also be integrated over.

The $|\mathscr{M}|^2$ for $t\bar{t}$ can be analytically derived, as in Mahlon and Parke [44, 45], reproduced here

$$|\mathscr{M}|^2 = \frac{g_s^{\,4}}{9} F\bar{F}((2-\beta^2 s_{qt}^2) - X_{sc}) \tag{5.9}$$

where β is the top quark velocity in the $q\bar{q}$ rest frame, X_{sc} contains terms describing spin correlations between top quarks, g_s is the strong coupling constant, and F $(\bar{F})$ are the top (anti-top) quark propagators respectively.

6

Analysis Technique

The sensitivity of a search can be estimated from the empirical measure of

$$\text{signal}/\sqrt{\text{background}}$$

The combination of SM prediction and detector effects like selection and tagging produces a $S/\sqrt{B} \sim \mathcal{O}(10^{-1})$. This is insufficient to do any kind of pure counting experiment, so advanced analysis techniques are required. Likelihood fitting allows extraction of the maximum amount of information from each event. We use the matrix elements as described in chapter 5 to form a likelihood function.

6.1 Likelihood Fitting — 1

Likelihood functions in a parameter need not be unique [46]. We use the matrix elements described in the previous chapter to form a likelihood function for each event. Each event has a signal and background probability based on matrix elements, P_s and a P_b respectively. The expression

$$L(S, \mathbf{x}|\mathbf{\Theta}) = SP_S(\mathbf{x}|\mathbf{\Theta}) + (1-S)P_b(\mathbf{x}|\mathbf{\Theta}) \tag{6.1}$$

is a per event likelihood in S given event kinematics $\mathbf{x}$ and theory parameters $\mathbf{\Theta}$. Notice that this function is linear in the S parameter, with the slope of the line indicating if the event is more signal-like or background-like.

The standard prescription for a likelihood fit on a set of measurements is to take the product of the individual likelihood curves. Therefore equation 6.1 becomes

$$\mathscr{L}(S) = \prod_i L(S, \mathbf{x}_i) = \prod_i SP_s(\mathbf{x}_i|\mathbf{\Theta}) + (1-S)P_b(\mathbf{x}_i|\mathbf{\Theta}) \tag{6.2}$$

where i is the index over events in the sample. As a matter of computability, we choose to instead maximize the log-likelihood

$$\log \mathscr{L}(S) = \sum_i \log L(S, \mathbf{x}_i) = \sum_i \log \left(SP_s(\mathbf{x}_i|\mathbf{\Theta}) + (1-S)P_b(\mathbf{x}_i|\mathbf{\Theta}) \right) \tag{6.3}$$

In the combined likelihood S means signal fraction, N_s/N for the sample under consideration. One of crucial properties of likelihood fitting is that the maximum likelihood estimator is normally distributed [6, 46].

6.2 Resampling

When considering events to fit, there are two complications. First, due to the slow speed of Monte Carlo generation and matrix element calculation, the statistics of events are limited. Secondly, the events that are generated by the slow Monte Carlo have weights based on things like trigger efficiencies.

Resampling techniques allow the extraction of more information from a limited set of events. The technique we use is called bootstrapping, which involves taking random subsamples from the large pool of events. A cursory overview of bootstrapping can be found in [47] and detailed information in [48]. Barlow [49] states the estimation of an error allows $(\mathcal{N}/n)^2$ subsamples in the bootstrap, where $\mathcal{N}$ is the number of events in the pool, and n is the number of events in the subsample. Since we are estimating the spread of a likelihood fit, the Barlow limit applies.

Bootstrapping allows us to form subsets of events similar to what we would expect from the CDF detector based on theory predictions. The theory predictions are given by table 4.9 and table 4.8. The subsets of events assembled are called *pseudo-experiments* (PEs). Because the events are sampled from a large pool of events, it allows weighted sampling, as more heavily weighted events are part of the subsamples more often.

6.3 Normalization

To ensure normalization of the matrix elements described in chapter 5, we perform an ad-hoc two component normalization using the likelihood fitter. Correctly normalized density functions are required for any likelihood fitting technique.

The four matrix elements, ZH, ZJJ, $t\bar{t}$, and ZZ are indexed by j. In principle, each should integrate to unity over all allowable phase space.

$$\int d\mathbf{x} P_j(\mathbf{x}|\mathbf{\Theta}) = \frac{1}{\sigma(\mathbf{\Theta})} \int d\mathbf{x} \frac{d\sigma(\mathbf{\Theta})}{d\mathbf{x}} = 1 \tag{6.4}$$

Practically, we obtain this instead

$$\int d\mathbf{x} P_j(\mathbf{x}|\mathbf{\Theta}) = \int d\mathbf{x} \frac{d\sigma(\mathbf{\Theta})}{d\mathbf{x}} = \sigma(\mathbf{\Theta}) \tag{6.5}$$

In the likelihood fit, P_s and P_b must have a correct relative normalization. Since there are four matrix elements, and relative normalizations must commute, that leaves three independent normalization constants to find. We find the three normalization constants by choosing one matrix element as a basis and calibrating the other three using a two component likelihood fit. We choose to normalize the other matrix elements againt the $t\bar{t}$ matrix element with a (arbitrary) subsample size of 500 events. To normalize, we let $P_s \rightarrow P_{t\bar{t}}$ and $P_b \rightarrow P_{\{ZH,ZJJ,ZZ\}}$. Then we run the likelihood fitter on sets of events that are 50% $t\bar{t}$ and 50% of $\{ZH, ZJJ, ZZ\}$. One sample log likelihood curve is shown as figure 6.1. There is a central limit theorem based effect that causes the polynomial

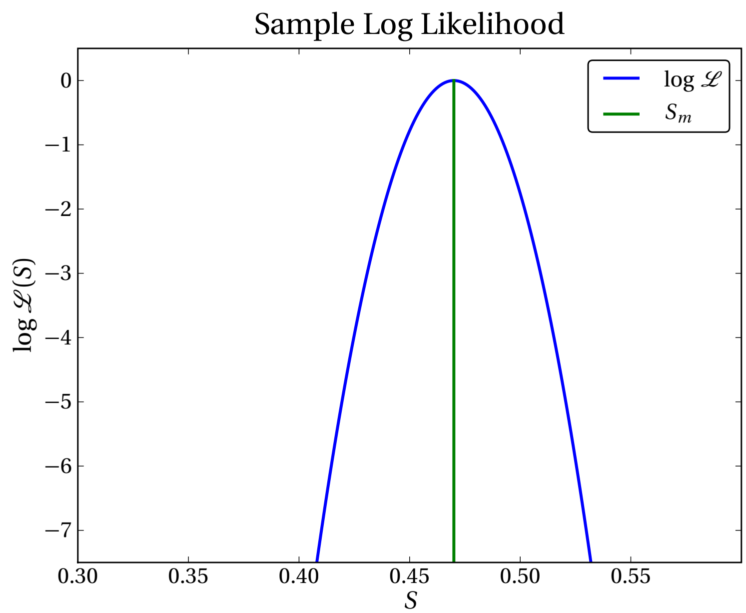

FIGURE 6.1: A single log likelihood curve, with the most likely value of S marked as S_m

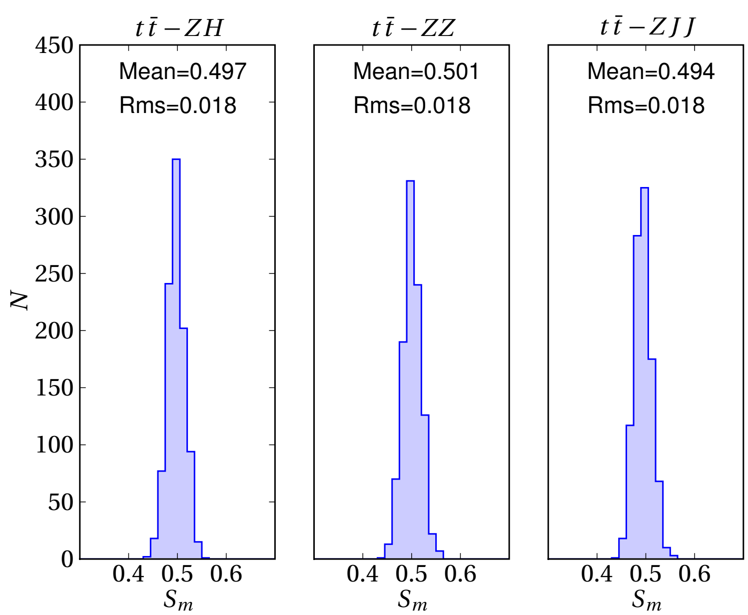

FIGURE 6.2: The aggregate histogram of most likely values (S_m) for normalization sets of events at $m_H = 115\ GeV/c^2$. Each of the matrix elements were multiplied by the appropriate constant (table 6.1) such that the histogram is centered at 0.5

expression for likelihood to become normally distributed, or correspondingly parabolic in log-likelihood space.

The bootstrap resampling technique introduces significant variation between subsamples. Each subsample produces a curve like the one in figure 6.1, and each curve has a most likely value, S_m (short for S_{measured}). Individual S_m values are histogrammed for each of the three cases ZH, ZJJ, ZZ, and the P_b values are multiplied by normalization constants which are adjusted until the mean of the histogram occurs at 0.5. The histograms for background and signal at $m_H = 115\ GeV/c^2$ are in figure 6.2. Other Higgs mass points produce very similar histograms. The properties of maximum likelihood fitting ensure the distribution of most likely values is Gaussian [46]. The arbitrary subsample size of 500 does not affect the mean of the S_m distribution, and so does not affect the normalization constant obtained.

Matrix Element	Normalization ($\sigma_{t\bar{t}}/\sigma(\Theta)$)
$t\bar{t}$	1
ZJJ	1.90×10^{-2}
ZZ	8.90×10^{-4}
$ZH100$	1.77×10^{3}
$ZH105$	2.01×10^{3}
$ZH110$	2.15×10^{3}
$ZH115$	2.35×10^{3}
$ZH120$	2.50×10^{3}
$ZH125$	2.65×10^{3}
$ZH130$	2.85×10^{3}
$ZH135$	3.05×10^{3}
$ZH140$	3.35×10^{3}
$ZH145$	3.65×10^{3}
$ZH150$	4.00×10^{3}

Table 6.1: Normalization constants for the matrix elements. $t\bar{t}$ was chosen as the basis for the normalization, and thus has a normalization of 1

6.4 Pseudo-Experiments

As described in section 6.2, pseudo-experiments are bootstrapped sets of events that follow the distributions we expect from theory (Tables 4.9 and 4.8). Because the theory predicts a constant rate of production for any given process, the number of events of events for that process must follow a Poisson distribution. The means of the Poisson distributions for each process are given in table 4.9 and 4.8.

The SM predicts a signal/$\sqrt{\text{background}}$ ratio of $\sim \mathcal{O}(0.1)$. Put another way, at $m_H = 115\ GeV/c^2$ and integrated luminosity of 2.7/fb, there is a background expectation of $\sim 300 \pm \sqrt{300} = 300 \pm 17$ events and a signal expectation of $\sim 1.9 \pm 1.4$ events. The background fluctuations due to Poisson statistics completely overwhelm any signal that may be present.

Consider a toy example where we are fitting a one dimensional kinematic distribution with two shapes, a signal shape and a background shape. In the case of these pseudo-experiments, there would be large fluctuations in the total integrated area between pseudo-experiments. Since the signal and background shapes are fixed, there would be a large spread in the fitted parameter purely due to poisson fluctuations.

Since the desirable outcome is to reduce the spread in the fitted parameter, we instead choose to normalize the distributions to some constant before performing the fit. This forces the fit to be based purely on shapes, and eliminates a large source of variation between pseudo-experiments. The same principle applies to the complex multidimensional fit done in this analysis.

We choose to only consider pseudo-experiments where $N_{\text{PE}} = N_{\text{data}}$, where N_{data} is the number of events observed at the CDF detector, in this case 290 events. This eliminates spread in the fitted parameter S_m caused by fluctuations in pseudo-experiment size, making the analysis a pure shape fit. It also has a nice interpretation that can be thought of as a Bayesian prior, that we only consider pseudo-experiments that might be what we observed at the real experiment.

As described in Chapter 4, SECVTX b tagging allows us to distinguish b quark jets from other jets by looking for a secondary vertex in the silicon detector. The selection requires at least one b tag, but there are kinematic differences between single b tagged and double b tagged events. To ensure that pseudo-experiments accurately represent the distributions we expect from theory, it is important to make sure the correct numbers of single b tagged and double b tagged events from each process are present. We define the ζ factors as

$$\zeta^{(j)}_{1\text{tag}} = N^{(j)}_{1\text{tag}}/N^{(j)} \tag{6.6}$$

$$\zeta^{(j)}_{2\text{tag}} = N^{(j)}_{2\text{tag}}/N^{(j)} \tag{6.7}$$

where the index j runs over the four different matrix elements (and corresponding Monte Carlo event pools), $\{ZH, ZJJ, t\bar{t}, ZZ\}$. ζ factors are the probability of an event from a certain category being single or double tagged. Table 6.2 and 6.3 give single and double tag rates for each of the four matrix elements.

	ZJJ	$t\bar{t}$	ZZ	
$\zeta_{1\text{tag}}$	0.91	0.74	0.80	$\zeta^B_{1\text{tag}} = 0.89$
$\zeta_{2\text{tag}}$	0.09	0.26	0.20	$\zeta^B_{2\text{tag}} = 0.11$

Table 6.2: Tagging rates for the backgrounds. The total $\zeta^B_{\text{k}-\text{tag}}$ are obtained by $N^{\text{k}-\text{tag}}_{\text{back}}/(N^{1\text{tag}}_{\text{back}} + N^{2\text{tag}}_{\text{back}})$ where $N^{\text{k}-\text{tag}}_{\text{back}}$ are the total background predictions from table 4.9 and 4.8 and k is 1 or 2.

ZH (m_H)	100	105	110	115	120	125	130	135	140	145	150
$\zeta_{1\text{tag}}$	0.67	0.67	0.66	0.66	0.66	0.65	0.65	0.64	0.64	0.64	0.63
$\zeta_{2\text{tag}}$	0.33	0.33	0.34	0.34	0.34	0.35	0.35	0.36	0.36	0.36	0.37

Table 6.3: Tagging rates for the signal at all Higgs masses between 100 and 150 GeV/c^2.

In addition to Poisson variability, each process has an associated rate systematic uncertainty from things like k-factor, b tagging uncertainties, and luminosity. Each rate systematic uncertainty is independent from other rate systematics, but is correlated across production processes. So for each production process, we add the different systematics in quadrature (because they are independent) and correlate the same systematic across processes. Therefore, all of the rate systematics can be reduced to a single distribution that is scaled according to the process. We believe the distribution to be Gaussian with a mean of zero and scale (σ) as given in table 6.4. A detailed examination of factors that compose the systematic are in section 6.7.

Process	Scale Factor
$Z \to ee + u\bar{u}, d\bar{d}, s\bar{s}$	0.425
$Z \to \mu\mu + u\bar{u}, d\bar{d}, s\bar{s}$	0.425
$Z \to \tau\tau + u\bar{u}, d\bar{d}, s\bar{s}$	0.425
$Z \to ee + c\bar{c}, b\bar{b}$	0.435
$Z \to mm + c\bar{c}, b\bar{b}$	0.435
$Z \to \tau\tau + c\bar{c}, b\bar{b}$	0.435
WW, WZ, ZZ	0.246
Fakes	0.500
$t\bar{t} \to l\bar{l}\nu\bar{\nu}b\bar{b}$	0.224

Table 6.4: Rate Systematic scale factor

Since we are searching for ZH signal in a shape fit, the amount of ZH in the pseudo-experiment must be a parameter of construction. This parameter is called $S_{\text{true}} = S_t = N_{\text{ZH}}/N_{\text{PE}}$ and represents the (known) fraction of ZH signal in the pseudo-experiment, where N_{ZH} is the poisson mean. Now we are ready to follow the pseudo-experiment procedure.

Pseudo-experiment Procedure

To understand the systematics, please see section 6.7.

1. Calculate the number of signal and background events expected given S_t.

$$N_s = S_t N_{\text{data}} \qquad\qquad N_b = N_{\text{data}} - N_s$$

2. Calculate the breakdown of signal and background events into 1-tag and 2-tag channels

$$N_s^{(1\text{tag})} = \zeta_{1\text{tag}}^{(ZH)} N_s \qquad N_s^{(2\text{tag})} = \zeta_{2\text{tag}}^{(ZH)} N_s$$

$$N_b^{(1\text{tag})} = \zeta_{1\text{tag}}^{B} N_b \qquad N_b^{(2\text{tag})} = \zeta_{2\text{tag}}^{B} N_b$$

3. Calculate event 1 tag and 2 tag probabilities and signal fractions

$$P_{1\text{tag}} = (N_s^{(1\text{tag})} + N_b^{(1\text{tag})})/N_{\text{data}}$$

$$P_{2\text{tag}} = (N_s^{(2\text{tag})} + N_b^{(2\text{tag})})/N_{\text{data}}$$

$$S_t^{(1\text{tag})} = N_s^{(1\text{tag})}/(N_s^{(1\text{tag})} + N_b^{(1\text{tag})})$$

$$S_t^{(2\text{tag})} = N_s^{(2\text{tag})}/(N_s^{(2\text{tag})} + N_b^{(2\text{tag})})$$

4. Generate a Binomial variate with $p = P_{1t}$, $q = P_{2t}$, and $N = N_{\text{data}} = 290$. This will give the single tagged PE size and the double tagged PE size by subtraction from N_{data}. This gives $N_{\text{constraint}}^{(1\text{tag})}$ and $N_{\text{constraint}}^{(2\text{tag})}$ respectively. Clearly $N_{\text{constraint}}$ fluctuates across different PEs.

5. Generate a Gaussian ($\mu = 0$, $\sigma = 1$) variate for rate scaling. For each process, scale this variate by the quadrature sum of all rate systematics (dominated by the k-factor, see table 6.4). Scale all background poisson means from Table 4.9 and 4.8 by the scaled Gaussian variate.

6. Generate Poisson variates per process based on the scaled poisson means in the 1 tag and 2 tag channel separately. Independently check that the number of events in the 1 tag channel $= N_{\text{constraint}}^{(1\text{tag})}$ and the number of events in the 2 tag channel $= N_{\text{constraint}}^{(2\text{tag})}$. If the constraint is not met for the 1 tag or 2 tag channel, generate a new set of Poisson variates for all processes within the tag channel. This is equivalent to

discarding PEs where $N \neq N_{\text{constraint}}$. Because N_{data} is the sum of the two $N_{\text{constraint}}$, this implies PEs where $N \neq N_{\text{data}}$ are discarded.

7. Some Gaussian variates are heavily suppressed, (with a k-factor of 0.4, if we fluctuate 2.5σ low, the poisson mean is zero), so we limit the number of sets of Poisson variates for a given Gaussian variate to 1000. The limit changes by a maximum of 0.5% as the number of Poisson sets per Gaussian variate varies from 1 to 10^6, which is significantly less than the statistical error on the limit.

8. At this point there is a breakdown of channels and processes (9 background and 1 signal process, 2 tag channels)=20 with a number of events to draw from each. At this point, we go to the pools of events (which have weights from trigger efficiencies and cross section), and using rejection based Monte Carlo, we draw the appropriate number of events from each category. These events form a pseudo-experiment, which is then fit using the likelihood fitter.

Noticeably, all tagging rates and ζ factors are based on Monte Carlo, not observed fluctuations in the data. This makes the analysis 'blind' to the observed number of 1 tag and 2 tag events. This is desirable as poisson b tagging fluctuations would propagate to a better or worse limit otherwise, amplifying b tagging uncertainty in the process.

6.5 Likelihood Fitting — 2

From table 4.9, 4.8 and 4.6, it is clear that the $S/\sqrt{B}$ is significantly higher in the 2 tag channel than in the 1 tag channel. We seek to take advantage of this to improve sensitivity by separating the two tag channels. However, for illustrative purposes, first consider the simpler case presented in section 6.1 (Combined tags).

6.5.1 Combined Tag Channels

We reproduce equation 6.2 here

$$\mathscr{L}(S) = \prod_i L(S, \mathbf{x}_i) = \prod_i S P_s(\mathbf{x}_i|\boldsymbol{\Theta}) + (1-S) P_b(\mathbf{x}_i|\boldsymbol{\Theta}) \tag{6.8}$$

To account for multiple backgrounds we replace P_b with a correctly weighted sum of the matrix element density functions for the backgrounds, namely

$$P_b(\mathbf{x}_i|\boldsymbol{\Theta}) \to \lambda_1 P_{b1}(\mathbf{x}_i|\boldsymbol{\Theta}) + \lambda_2 P_{b2}(\mathbf{x}_i|\boldsymbol{\Theta}) + \lambda_3 P_{b3}(\mathbf{x}_i|\boldsymbol{\Theta}) + \ldots \tag{6.9}$$

where λ_j is the background fraction of the jth background as defined by $\lambda_j = N_b^{(j)}/N_b$. Therefore, $\sum_j \lambda_j = 1$. This constraint on λ_j and the S, $(1-S)$ construction in the likelihood ensure that normalization is maintained at all S, an essential condition for likelihood fitting. With the three backgrounds, the likelihood expression becomes.

$$\mathscr{L}(S) = \prod_i (S P_{ZH}(\mathbf{x}_i|M_H) + (1-S)\left(\lambda_{ZJJ} P_{ZJJ}(\mathbf{x}_i) + \lambda_{ZZ} P_{ZZ}(\mathbf{x}_i) + \lambda_{t\bar{t}} P_{t\bar{t}}(\mathbf{x}_i)\right) \tag{6.10}$$

Like the normalization case, pseudo-experiments produce a Gaussian curve in S, much like figure 6.1. And like the normalization case, we make a histogram of most likely values of the signal fraction (S_m).

6.5.2 Separated Tag Channels

We know that a ZH signal event has a higher probability than background of being double tagged. We seek to enhance sensitivity by using this fact, so we reform the likelihood expression as follows.

$$\mathscr{L}(S) = \left(\prod_m L(S, \mathbf{x}_m)\right) \times \left(\prod_n L(S, \mathbf{x}_n)\right) \tag{6.11}$$

where m runs over single tagged events and n runs over double tagged events. If we make an approximation that the tagging probability is independent of event kinematics (a reasonable approximation), we can reweight matrix element probabilities by the tagging probability for that matrix element.

$$P_j(\mathbf{x}|\mathbf{\Theta}) \rightarrow P(\mathbf{x}|\mathbf{\Theta})P_j(k) \tag{6.12}$$

where k is the number of tags for the event. Since $P_j(k)$ is exactly equivalent to the ζ factors defined earlier (equation 6.6 and 6.7), we substitute. This makes equation 6.10 into

$$\begin{aligned}\mathscr{L}(S) = &\Bigg[\prod_m (S)\left(\zeta^{ZH}_{1\text{tag}}\, P_{ZH}(\mathbf{x}_m|M_H)\right) \\ &\quad + (1-S)\left(\lambda_{ZJJ}\,\zeta^{ZJJ}_{1\text{tag}} P_{ZJJ}(\mathbf{x}_m) + \lambda_{ZZ}\,\zeta^{ZZ}_{1\text{tag}} P_{ZZ}(\mathbf{x}_m) + \lambda_{t\bar{t}}\,\zeta^{t\bar{t}}_{1\text{tag}} P_{t\bar{t}}(\mathbf{x}_m)\right)\Bigg] \\ \times &\Bigg[\prod_n (S)\left(\zeta^{ZH}_{2\text{tag}}\, P_{ZH}(\mathbf{x}_n|M_H)\right) \\ &\quad + (1-S)\left(\lambda_{ZJJ}\,\zeta^{ZJJ}_{2\text{tag}} P_{ZJJ}(\mathbf{x}_n) + \lambda_{ZZ}\,\zeta^{ZZ}_{2\text{tag}} P_{ZZ}(\mathbf{x}_n) + \lambda_{t\bar{t}}\,\zeta^{t\bar{t}}_{2\text{tag}} P_{t\bar{t}}(\mathbf{x}_n)\right)\Bigg]\end{aligned} \tag{6.13}$$

which coupled with tables 6.2, 6.3, and 6.5, completely defines the likelihood fitter.

λ_{ZJJ}	0.8852
λ_{ZZ}	0.0463
$\lambda_{t\bar{t}}$	0.0685

Table 6.5: λ background fractions are based on theory predictions, as given in tables 4.9 and 4.8

Since each event introduces a term into the likelihood that is linear in S, the product is necessarily a polynomial. The polynomial construction of the likelihood ensures that $\mathscr{L}(S)$ diverges at $\pm\infty$. We start to see this divergence at S less than 0 and greater than 1. Because we know the likelihood fit to be a biased estimator, we scan outside the physical zero to one region in S. This leads to difficulties in finding the likelihood peak in an automated way in the analysis software.

$$\begin{aligned}\log \mathscr{L}(S) = \sum_m \log \Bigg[&(S)\left(\zeta^{ZH}_{1\text{tag}}\, P_{ZH}(\mathbf{x}_m|M_H)\right) \\ &+ (1-S)\left(\lambda_{ZJJ}\,\zeta^{ZJJ}_{1\text{tag}} P_{ZJJ}(\mathbf{x}_m) + \lambda_{ZZ}\,\zeta^{ZZ}_{1\text{tag}} P_{ZZ}(\mathbf{x}_m) + \lambda_{t\bar{t}}\,\zeta^{t\bar{t}}_{1\text{tag}} P_{t\bar{t}}(\mathbf{x}_m)\right)\Bigg] \\ + \sum_n \log \Bigg[&(S)\left(\zeta^{ZH}_{2\text{tag}}\, P_{ZH}(\mathbf{x}_n|M_H)\right) \\ &+ (1-S)\left(\lambda_{ZJJ}\,\zeta^{ZJJ}_{2\text{tag}} P_{ZJJ}(\mathbf{x}_n) + \lambda_{ZZ}\,\zeta^{ZZ}_{2\text{tag}} P_{ZZ}(\mathbf{x}_n) + \lambda_{t\bar{t}}\,\zeta^{t\bar{t}}_{2\text{tag}} P_{t\bar{t}}(\mathbf{x}_n)\right)\Bigg] \end{aligned} \tag{6.14}$$

When fitting the peak in the analysis software, we use the log likelihood, as in equation 6.14. Reliably finding the peak is not always trivial, so we use the well known and efficient Nelder-Mead [50, 51] maximization algorithm. Nelder-Mead, also known as the *amoeba method*, is preferred over other methods as it does not require the calculation of derivatives and minimizes computationally expensive function evaluations of likelihood. The specific implementation used is from the Apache Java Commons Math 2.0 Snapshot.

6.6 Feldman-Cousins Method

The likelihood fitter produces a likelihood curve for each constructed pseudo-experiment. Examples for pseudo-experiment likelihood and log-likelihood curves are shown as figures 6.3 and 6.4.

The most likely value is the S_{measured}, the measured signal fraction. This corresponds to S_{true}, the true signal fraction the pseudo-experiment was constructed with. We map the correspondence between the known signal fraction and the measured signal fraction, and the mapping allows us to adjust for any biases in the estimator.

The Feldman-Cousins method [52] provides a prescription for performing this map-

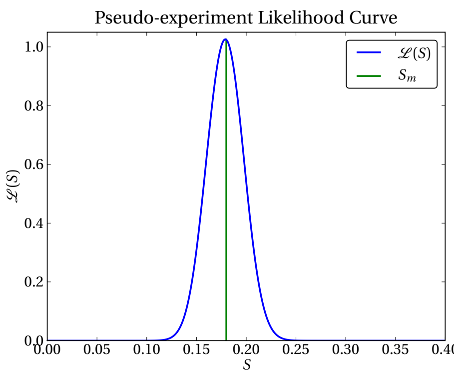

FIGURE 6.3: Pseudo-experiment Likelihood

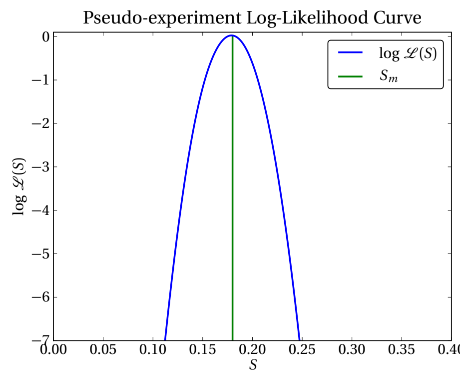

FIGURE 6.4: Pseudo-experiment Log-Likelihood

ping and setting an interval. It requires scanning in the theory parameter, and forming a distribution of the measured parameter on simulated pseudo-experiments. The relationship can be inverted to obtain the distribution in the theory parameter given the measured parameter. The most likely theory parameter for any given S_{measured} is $S_{\text{true}}^{\text{best}}$.

$$R = \frac{\mathscr{L}(S_m|S_t)}{\mathscr{L}(S_m|S_t^{\text{best}})} \tag{6.15}$$

The ratio R gives the relative likelihood of two hypotheses, one with a theory parameter of S_t and the other with a theory parameter of S_t^{best}. The ratio of the relative likelihoods (not the same likelihood as the matrix element likelihood) is something known as a *likelihood ratio test*, which is equivalent to more well known statistical hypothesis tests like a t-test. Choosing a value of the ratio R is equivalent to choosing a statistical significance confidence level.

The ratio is used as the test statistic in the Feldman-Cousins procedure, and the frequentist Neyman construction is used to form confidence bands. This ensures statistical coverage by construction and allows a self-consistent way of setting a two sided or one sided coverage interval.

We follow the Feldman-Cousins procedure for this analysis, using the likelihood fitter's most likely value S_m as the estimator. Figure 6.5 shows the histograms for selected S_t

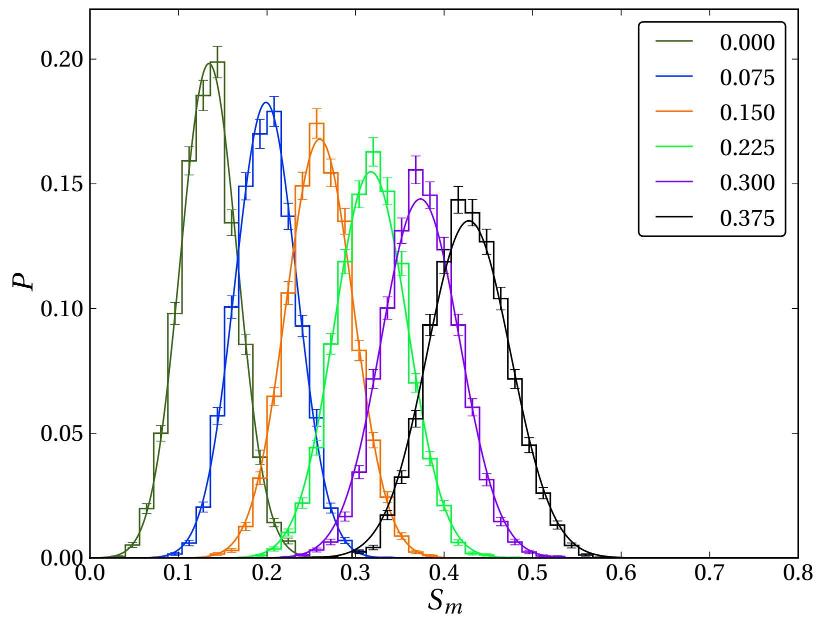

FIGURE 6.5: Measured Signal Fraction Peak Histograms. The legend indicates S_t.

values in the scan. From the properties of likelihood fitting [46], we know that the most likely value has a Gaussian distribution as long as the original source distribution (in this case the matrix elements) have compact support. We fit Gaussians to the histograms and use the fitted Gaussians (shown) as the distribution of S_m.

Noticeably, the width of the fitted Gaussians increase as the amount of average signal fraction present in pseudo-experiments (S_t) increases. This is exactly what we expect if we think of the likelihood fit a two component signal-background fit, because the size of the Poisson fluctuations on signal increase as S_t increases. We gain a better sense of what the histograms look like in two dimensions (Figure 6.6). The figure indicates that the mean and spread of the Gaussians in S_m can be modeled as a function of S_t. We fit an ad-hoc cubic polynomial for the mean and width of the Gaussians.

The polynomial fit for the mean and width of the Gaussians in S_m gives an analytic model of $P(S_m|S_t)$. We then take the ratio R as defined in equation 6.15 and normalize the ratio distribution for each S_t. In the S_m, S_t plane, this leads to adjusted distribution of Figure 6.7.

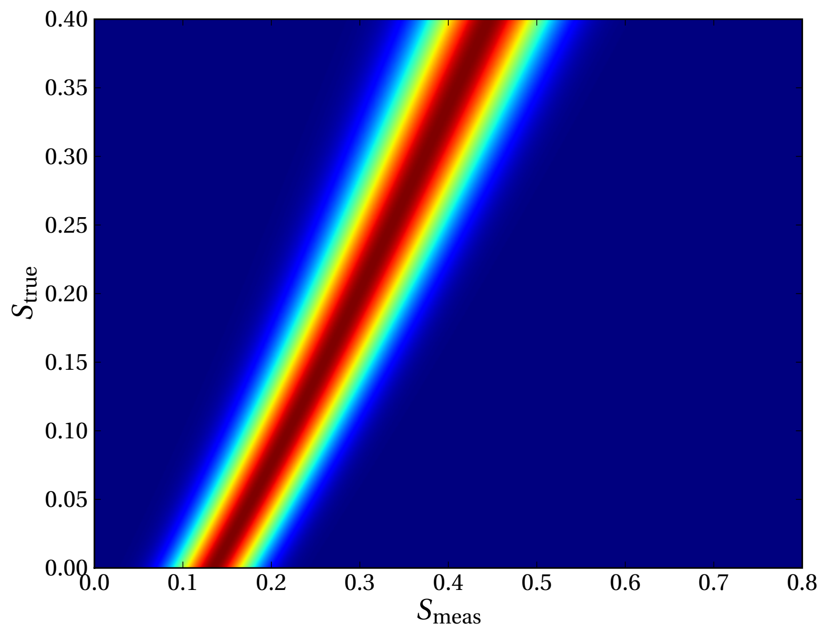

FIGURE 6.6: Measured Signal Fraction 2D Map. Warmer colors indicate higher probabilities of measurement.

For a given S_t and coverage threshold, we select the central interval in R such that the integrated area is equal to the coverage threshold. We do this at all S_t to get the boundaries at the specified coverage interval. This sets the coverage bands over the S_m, S_t plane which is all that is necessary for setting a one-sided or two-sided interval using the Feldman-Cousins construction. The results are presented in chapter 7.

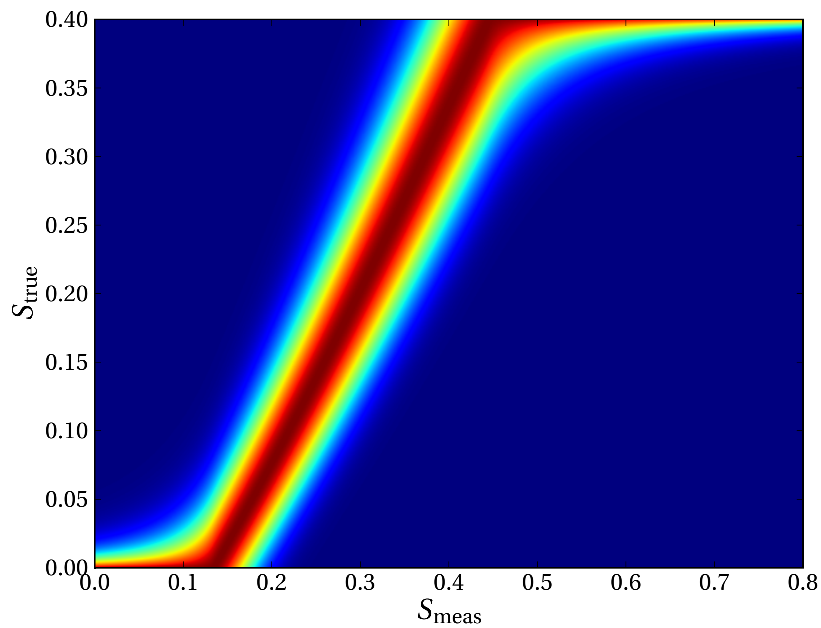

FIGURE 6.7: Feldman-Cousins Ratio

6.7 Systematics

There are several systematic effects that must be accounted for when performing the analysis. They can broadly be broken up into two categories, rate systematics and shape systematics. Rate systematics reflect an uncertainty in the number of events of a particular process in relation to other processes or total. Shape systematics affect the shape of the kinematic distributions, and therefore the shape of the matrix element distributions.

The rate systematics are k-factor uncertainty, luminosity uncertainty, and b-Tagging uncertainty. The k-factor is defined as the ratio of the true cross section of a process to the leading order cross section, $k = \sigma/\sigma_{LO}$. Since the luminosity needs to be measured, there is an experimental uncertainty from the CDF luminosity detector. The b-tagging uncertainty indicates that the simulated tagging rate might not match the actual tagging rate. b-tagging uncertainty varies for the different quarks in the final state, namely that a light flavor or c quark is tagged differently from an actual b quark.

Uncertainty	Value
k-factor (ZJJ)	40%
k-factor (WZ/ZZ, $t\bar{t}$)	20%
Luminosity	6%
Tagging ($u\bar{u}$, $d\bar{d}$, $s\bar{s}$)	13%
Tagging ($c\bar{c}$)	12.4%
Tagging ($b\bar{b}$)	5.6%

Table 6.6: Rate Uncertainties. Each of the three uncertainties (k-factor, Luminosity, b-Tagging) is believed to be independent of the others. Tagging uncertainty is applied once per tag.

Since the three rate uncertainties are independent of each other, the total uncertainty is the quadrature sum of the three uncertainties. Because each of the uncertainties is correlated across samples, the rates of all samples must be scaled simultaneously. This explains the drawing of the Gaussian variate as outlined in the pseudo-experiment construction procedure in section 6.4

The k-factor uncertainty dominates the rate uncertainties because of the quadrature sum. However, table 4.8 and 4.9 show that the total number of events predicted agrees with the observed number to within 1 σ. Entirely separate from the rate systematics, there are poisson fluctuations for each process. Because the analysis is a pure shape fit, the data effectively constrains the rate systematic distribution.

There are also the shape systematic uncertainties, which are *Initial State Radiation* (ISR), *Final State Radiation* (FSR), and *Jet Energy Scale* (JES). ISR introduces an extra parton in the initial state, leading to an extra jet in the event, ($q\bar{q}q' \rightarrow ZHq' \rightarrow l^+l^-b\bar{b}q'$). FSR introduces an extra jet or lepton in the event as well, but in the final state ($q\bar{q} \rightarrow ZH \rightarrow l^+l^-b\bar{b}q'$). Jet Energy Scale uncertainty arises from the difficulty in calibrating the energy measured in the calorimeter with the true energy of the jet.

Shape uncertainties can be accounted for by adjusting the shape of the S_m histograms. For each shape systematic, we perform pseudo-experiments at $\pm 1\sigma$ in the systematic. At any given S_t, these systematically varied pseudo-experiments lead to a shift in the

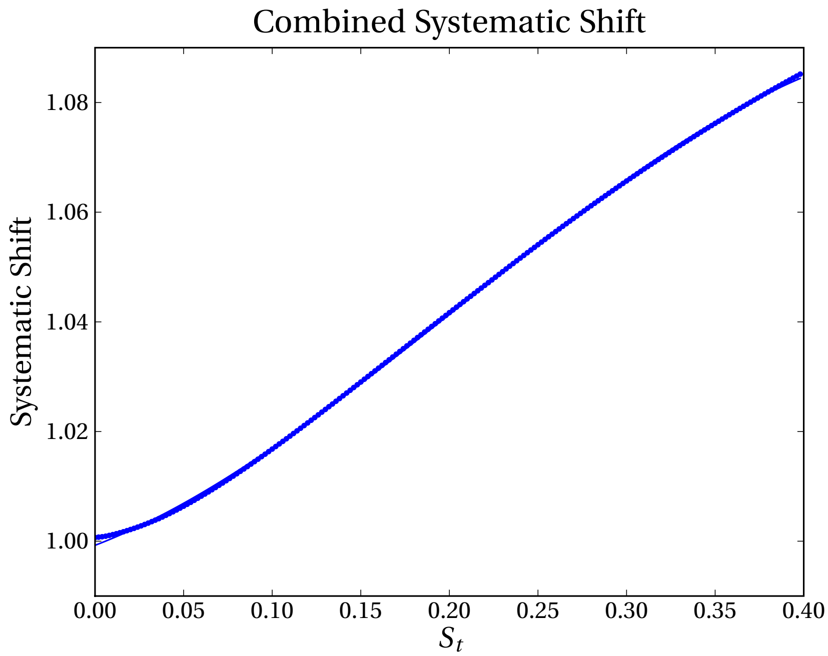

FIGURE 6.8: Rms scale factor as a function of S_t for S_m distributions due to shape systematics. The dominant systematic is ISR, which causes misidentification of jets when performing the selection.

S_m histogram mean by $\delta_\pm$. We assume the shift in the S_m histogram to be linear in the systematic, namely $\Delta = \delta_\pm \sigma_{\text{syst}}$. Since the systematic distribution is assumed to be a Gaussian, we want to weight the shift in the S_m histogram with a Gaussian in the systematic. Because the S_m histogram is itself Gaussian, and we want to weight with a systematic Gaussian, we convolute the two Gaussians, effectively adding their variances to form a new histogram in S_m with the systematic included. We repeat this for all three shape systematics, effectively increasing the S_m histogram variance at each S_t by the sum of the variances due to the three shape systematics. The ratio of the standard deviations with and without all systematics included is plotted in figure 6.8. It shows that over a range of 0 to 0.4 S_t, standard deviation of the S_m histogram is increased between 0 and 9% due to systematics.

7

Results

Using 2.7 fb^{-1} of data (through period 17), 290 events pass the selection outlined in chapter 4. These 290 events are fitted with the likelihood fitter from chapter 6. The resulting likelihood curve is figure 7.1.

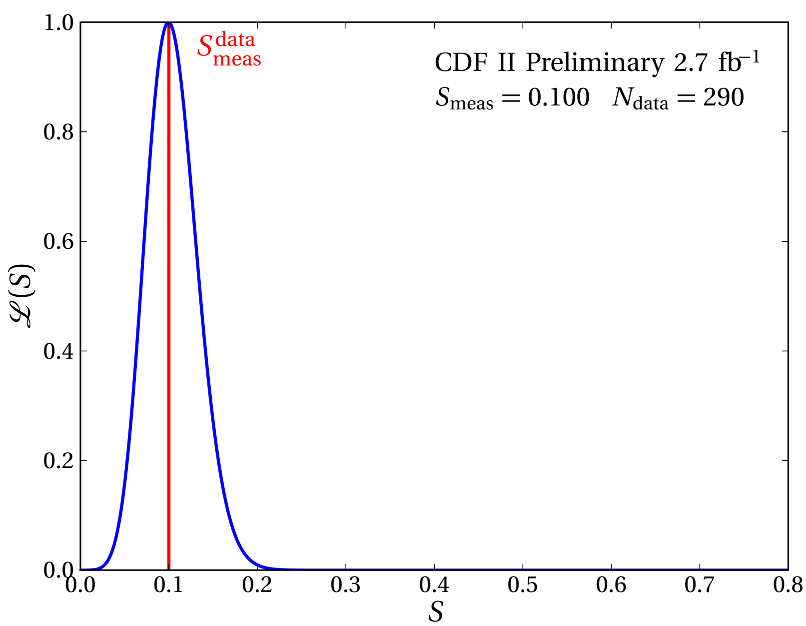

FIGURE 7.1: Data Likelihood Curve

The data likelihood curve peaks at $S_{\text{meas}}^{(\text{data})} = 0.100$. Three discrete coverage levels corresponding to 1, 2, and 3 σ are selected from figure 6.7 and are shown as figure 7.2.

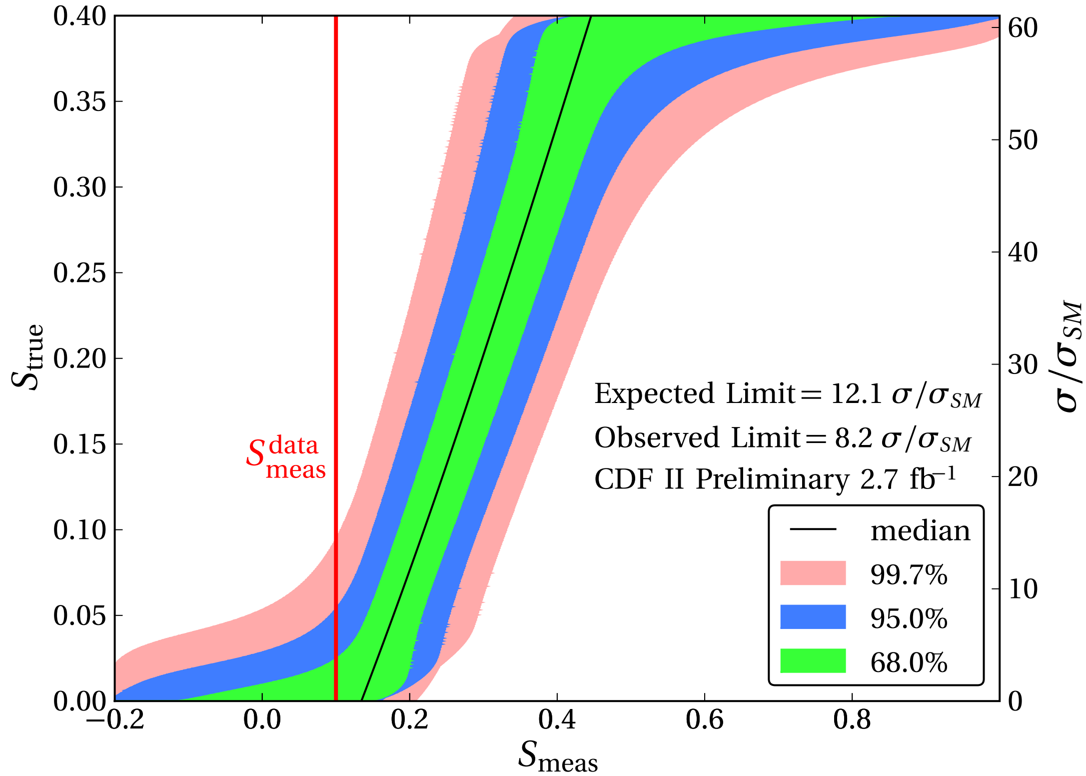

FIGURE 7.2: Feldman-Cousins confidence bands. The most likely S from data is indicated as the red line. The most likely S_m (based on simulation) as a function of S_t is the black median line. $M_H = 115\ GeV/c^2$

The most likely S from the data is indicated as $S_{\text{meas}}^{\text{data}}$, the red line. At 95 % coverage (blue band), $S_{\text{meas}}^{\text{data}}$ crosses the upper blue boundary at a S_{true} of 0.0537, which corresponds to a σ/σ_{SM} of 8.2 (right axis).

The expected limit is obtained by assuming that $S_t = 0$, and calculating the distribution of limits that would be obtained by the Feldman-Cousins prescription. The distribution for $M_H = 115\ GeV/c^2$ is given in figure 7.3.

The limits at all masses are given in table 7.1 using the SM cross sections defined in

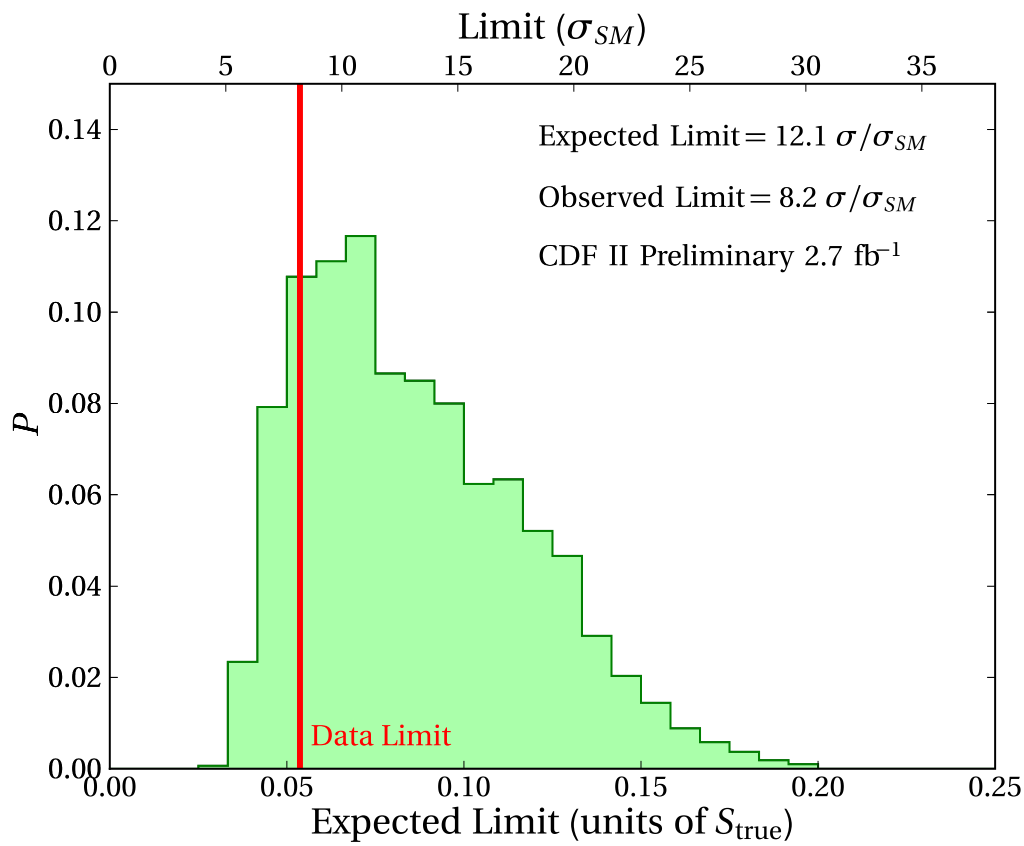

FIGURE 7.3: Expected distribution of limits assuming that $S_t = 0$ and 95% coverage. The data limit is at the 13th percentile. The median of this distribution defines the expected limit. $\pm 1, \pm 2\ \sigma$ limits are defined by the appropriate point on the cumulative density function for this distribution. $M_H = 115\ GeV/c^2$

figure 2.14. The table is plotted in figure 7.4. Noticeably, the data favors a lower limit as compared to the expected limit at all M_H considered. A full set of coverage bands for all M_H between 100 and 150 GeV/c^2 is provided in appendix A

M_H	-2σ	-1σ	*median*	$+1\sigma$	$+2\sigma$	*Observed*
100	4.8	6.0	*8.7*	12.5	16.2	*7.0*
105	4.7	6.1	*8.7*	12.9	17.1	*6.5*
110	5.6	7.5	*11.3*	16.8	22.3	*7.6*
115	6.4	8.3	*12.1*	18.2	24.2	*8.2*
120	7.1	9.3	*13.5*	20.0	26.5	*9.0*
125	10.7	13.2	*18.3*	27.1	35.2	*13.2*
130	13.7	17.1	*24.2*	35.7	46.6	*17.7*
135	17.4	21.8	*31.0*	44.8	58.6	*22.9*
140	24.4	31.1	*44.3*	65.4	85.0	*32.0*
145	33.5	42.8	*61.6*	89.9	118.8	*43.2*
150	58.2	73.7	*104.1*	153.2	198.3	*71.3*

Table 7.1: Expected and observed limits in units of σ_{SM}, as given by Figure 2.14. Uses 2.7 fb^{-1} of CDF II data, through period 17.

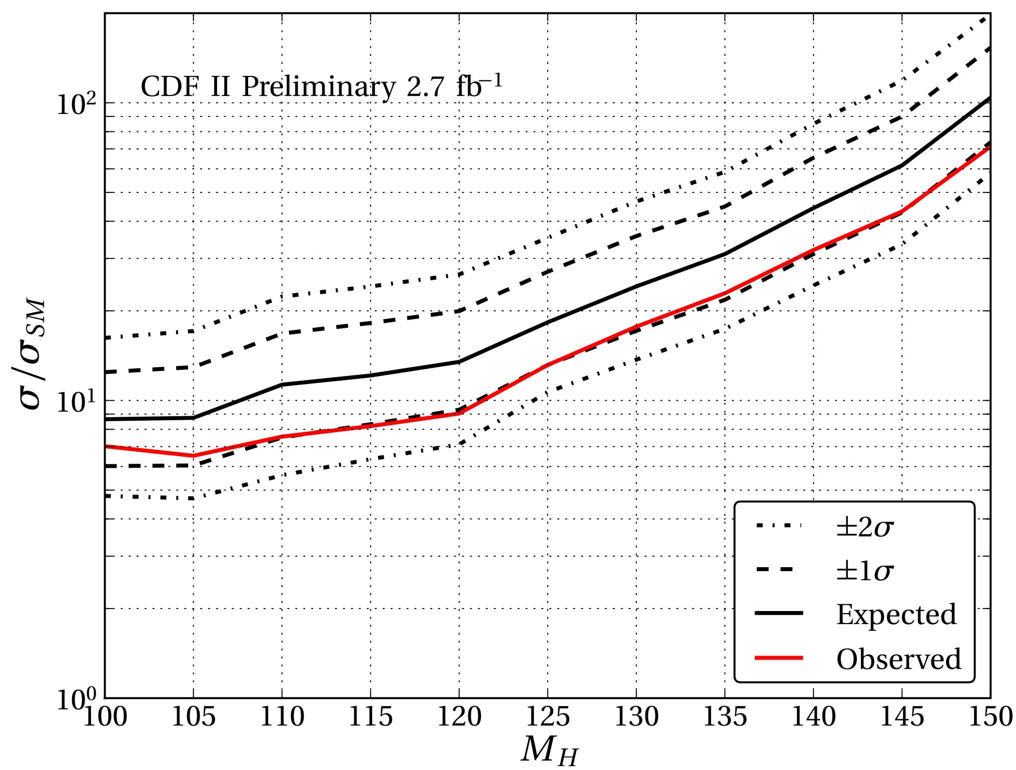

FIGURE 7.4: $p\bar{p} \to ZH \to l^+l^-b\bar{b}$ limits at 95% coverage.

8

Conclusions

Appendix A

Additional Plots

We show data likelihood curves, Feldman-Cousins confidence bands, and expected limit distributions at all M_H between 100 and 150 GeV/c^2.

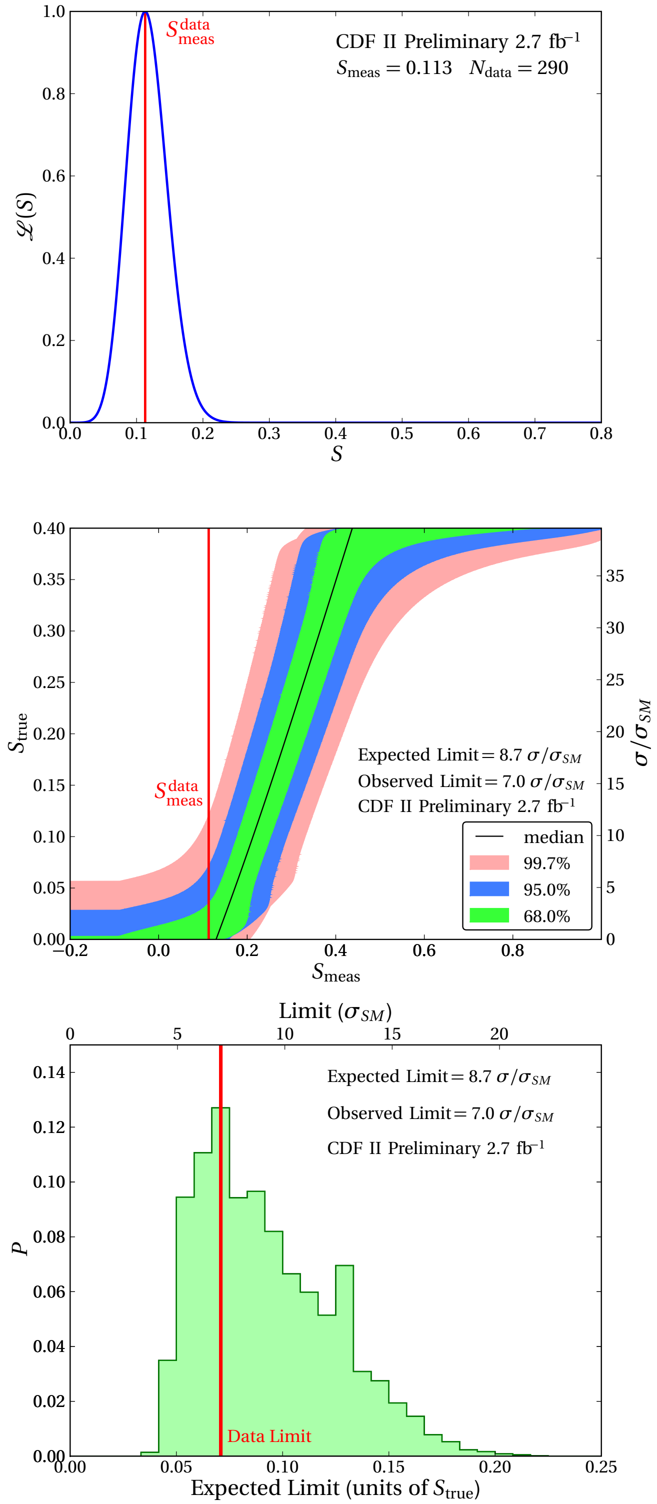

FIGURE A.1: $M_H = 100\ GeV/c^2$

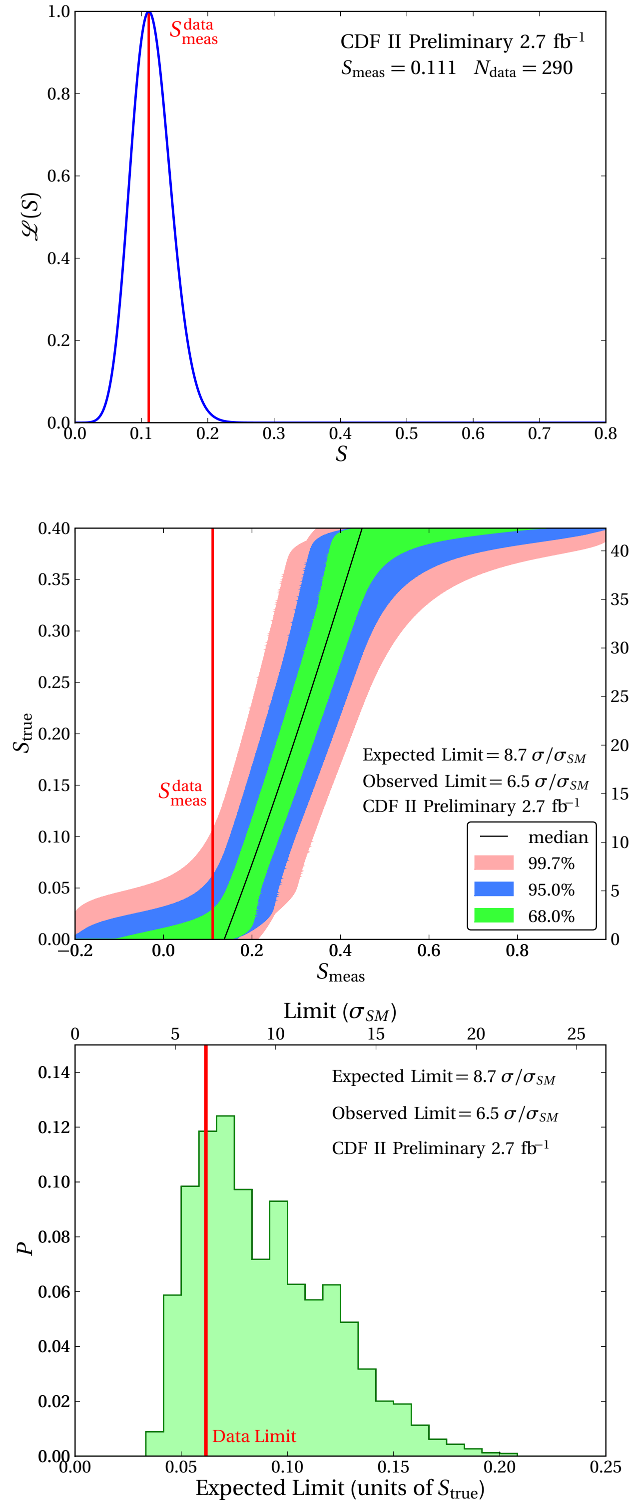

FIGURE A.2: $M_H = 105\ GeV/c^2$

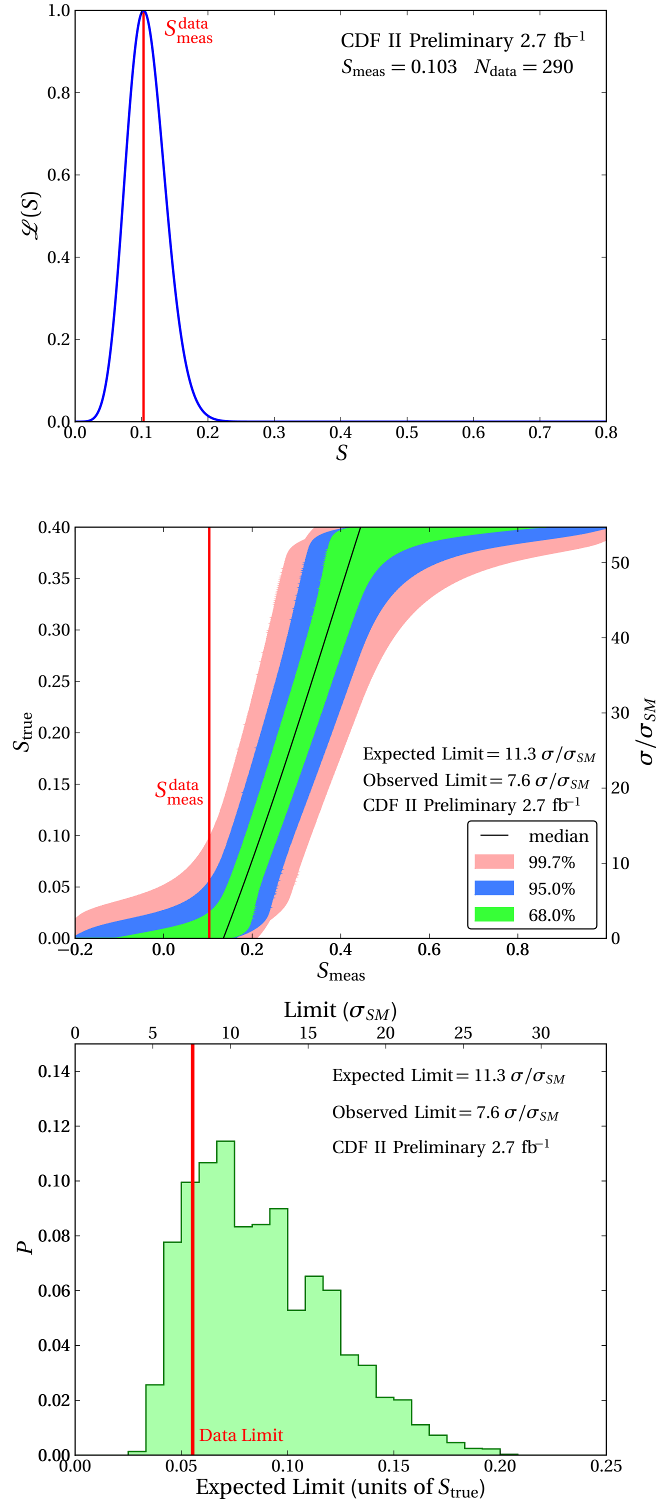

FIGURE A.3: $M_H = 110\ GeV/c^2$

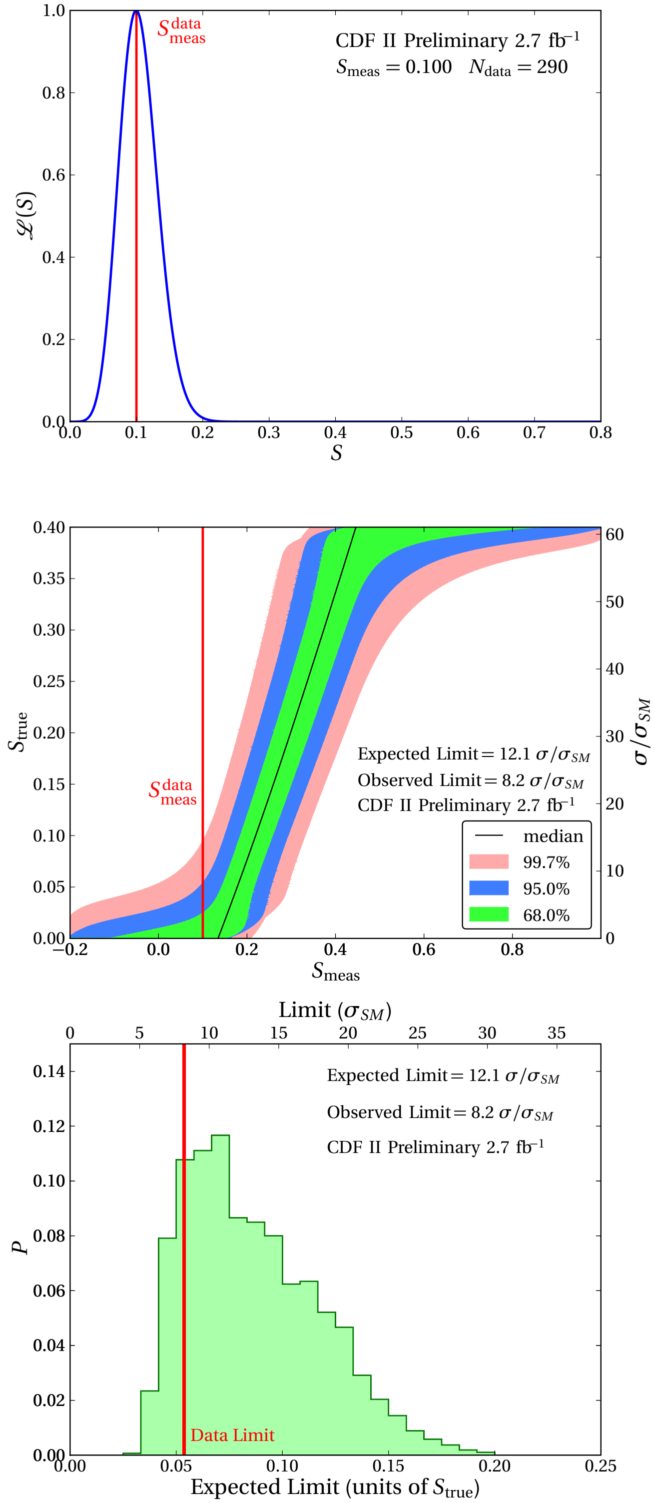

FIGURE A.4: $M_H = 115\ GeV/c^2$

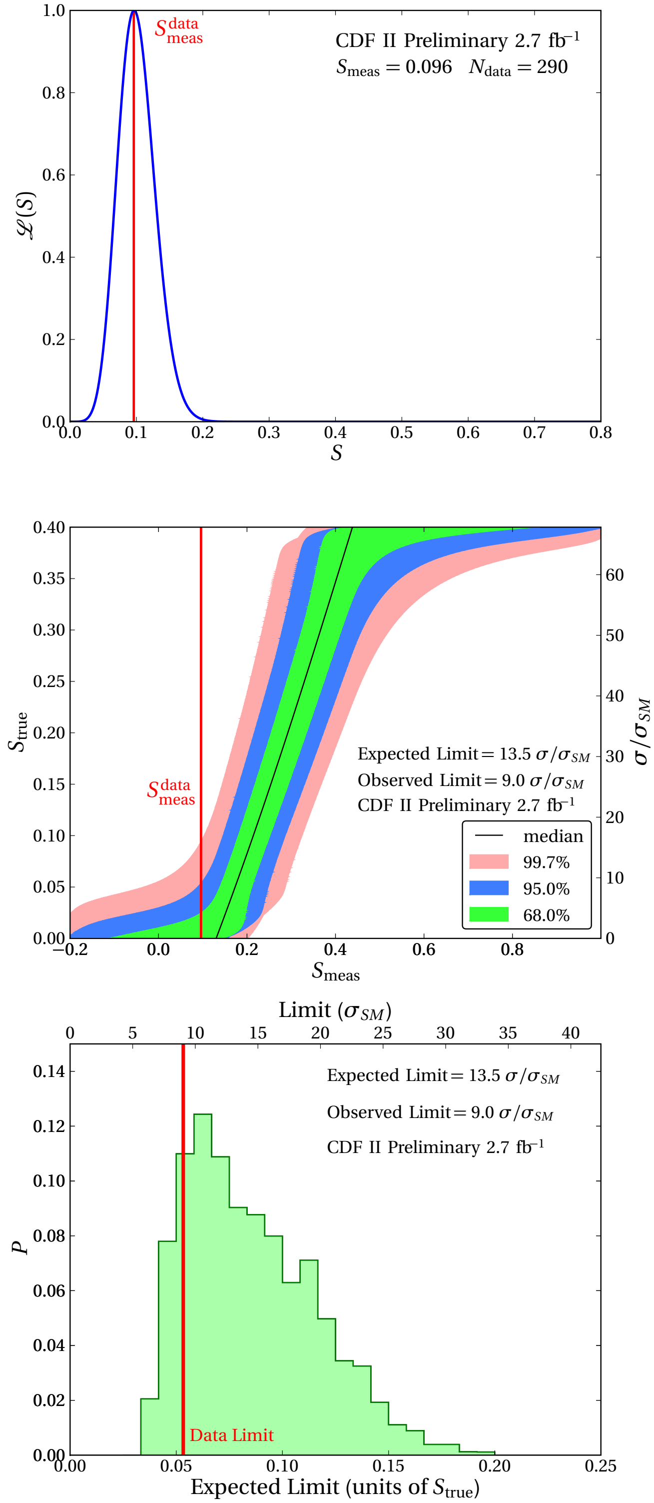

FIGURE A.5: $M_H = 120\ GeV/c^2$

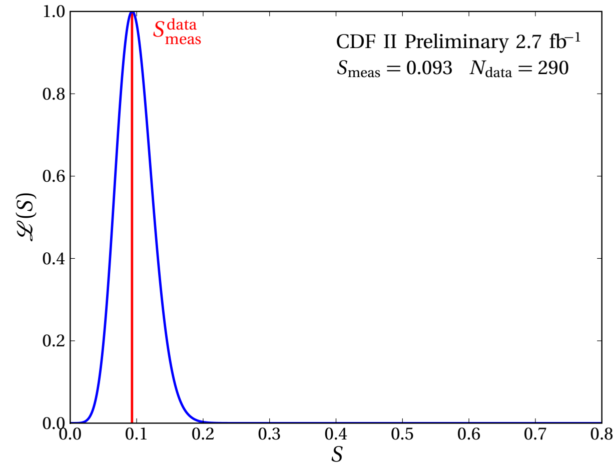

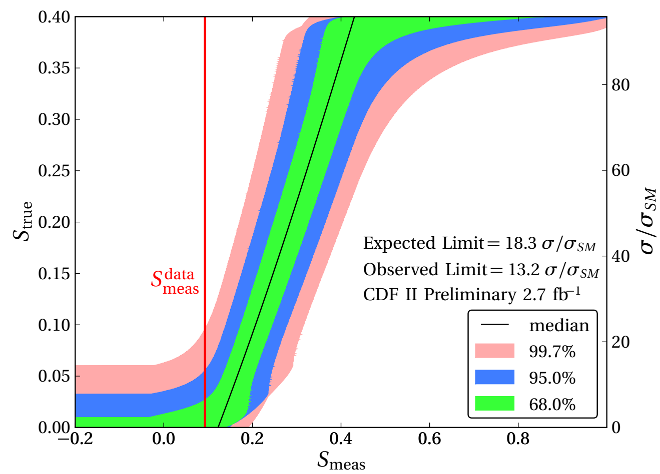

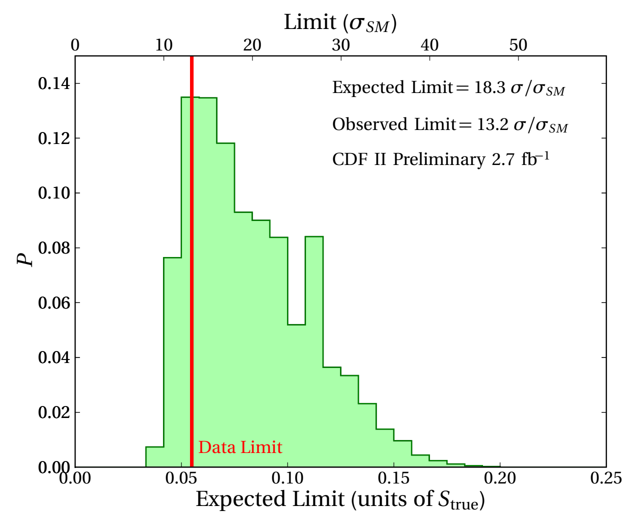

FIGURE A.6: $M_H = 125\ GeV/c^2$

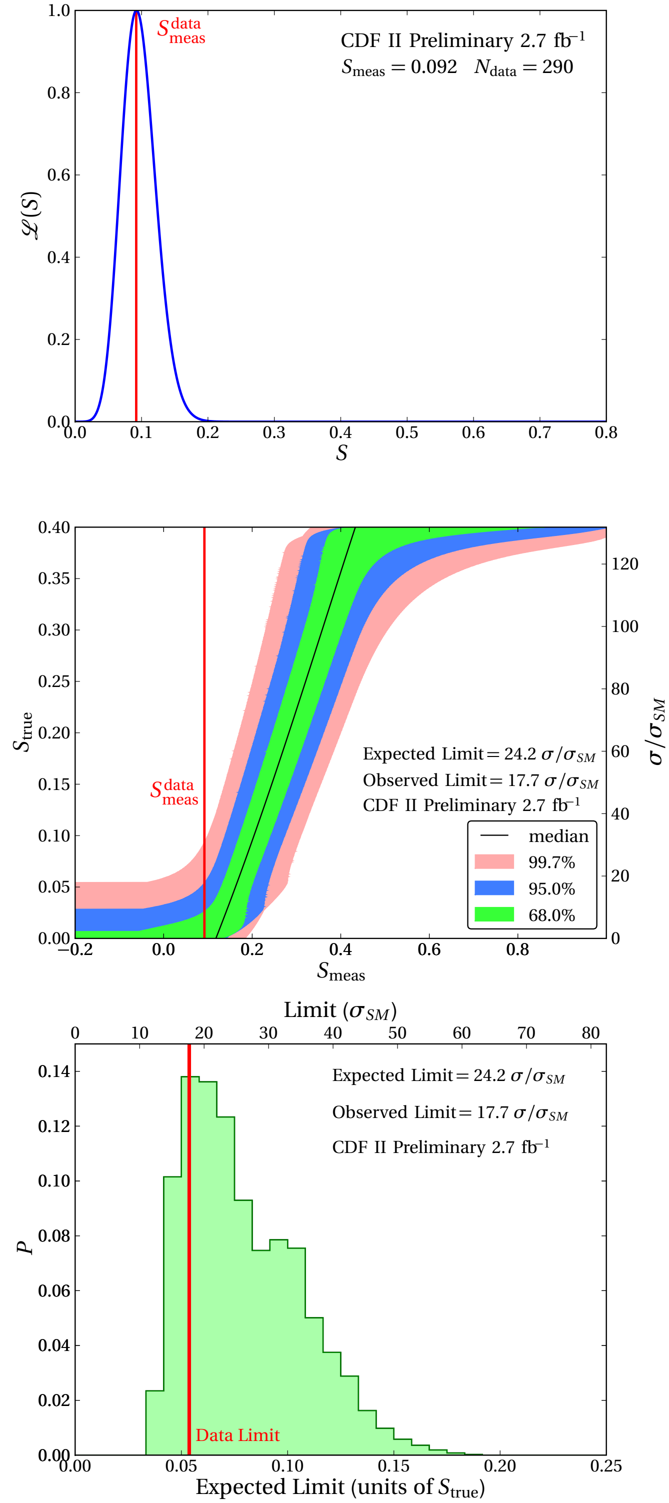

FIGURE A.7: $M_H = 130\ GeV/c^2$

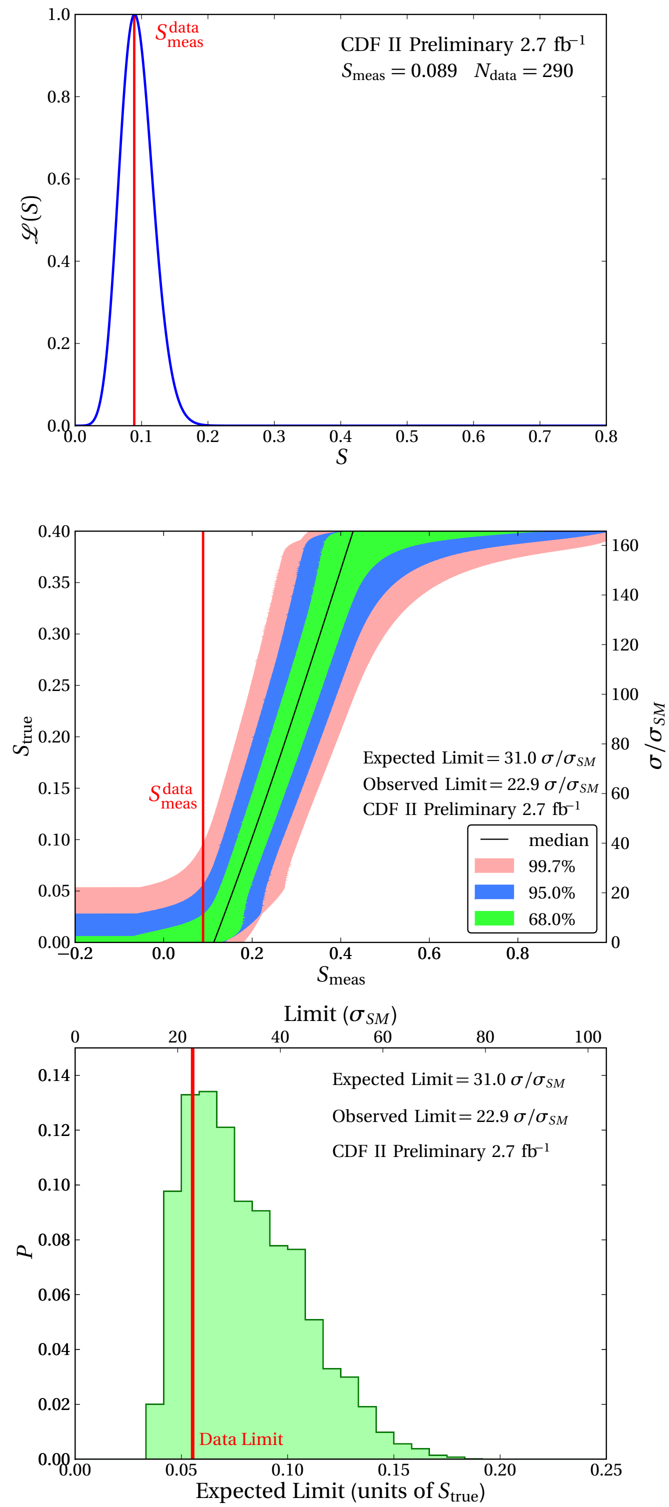

FIGURE A.8: $M_H = 135\ GeV/c^2$

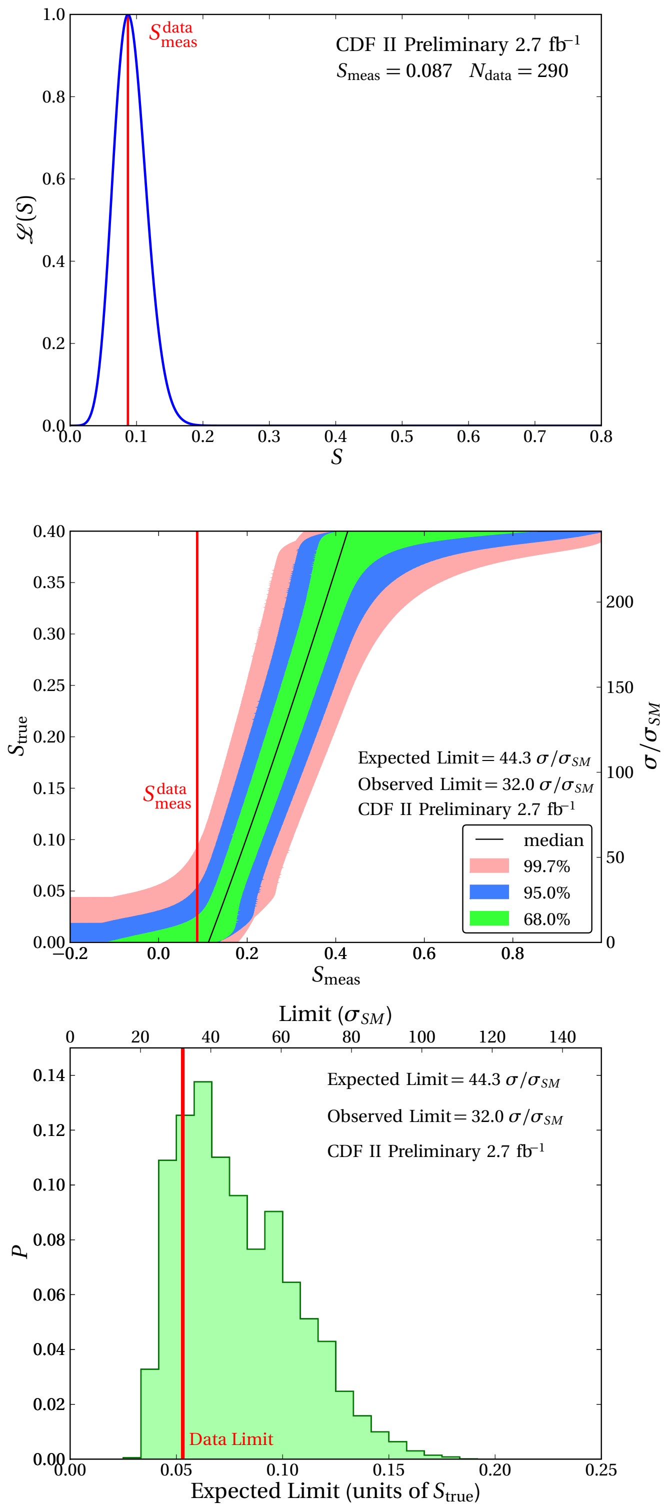

FIGURE A.9: $M_H = 140\ GeV/c^2$

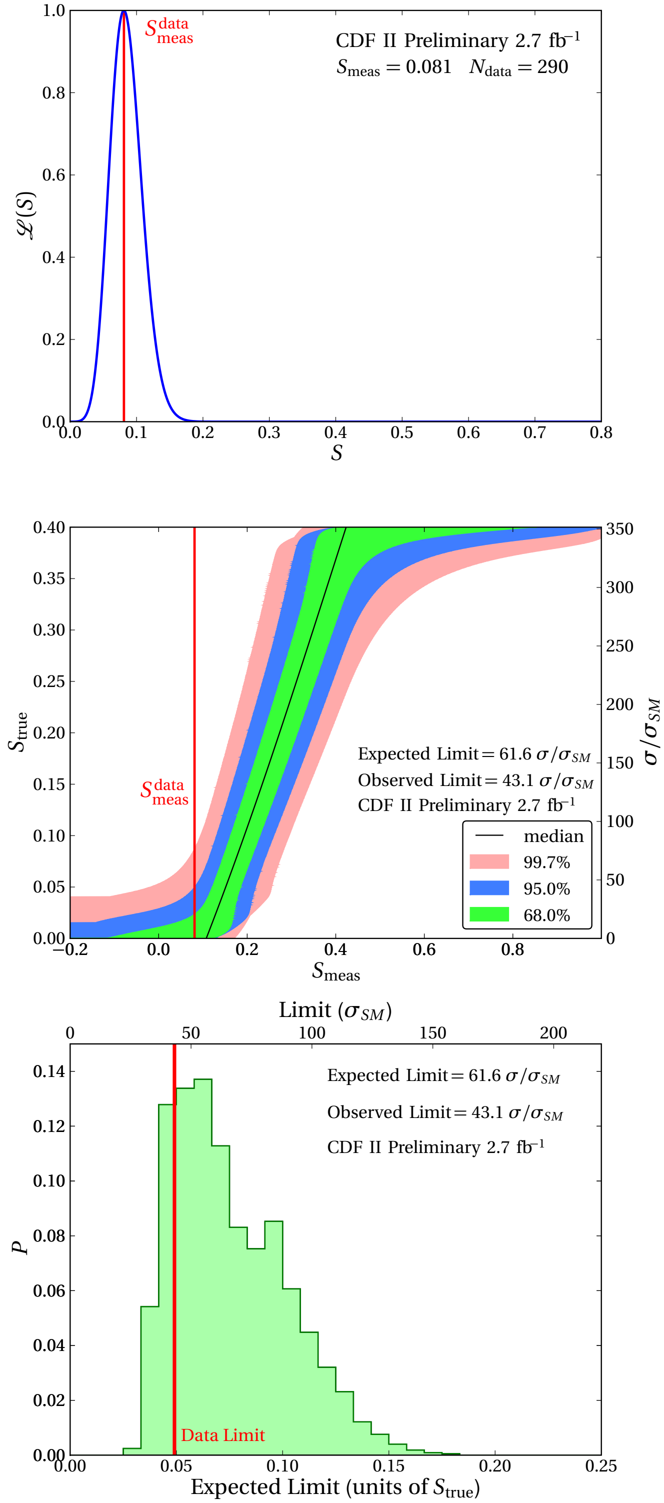

FIGURE A.10: $M_H = 145\ GeV/c^2$

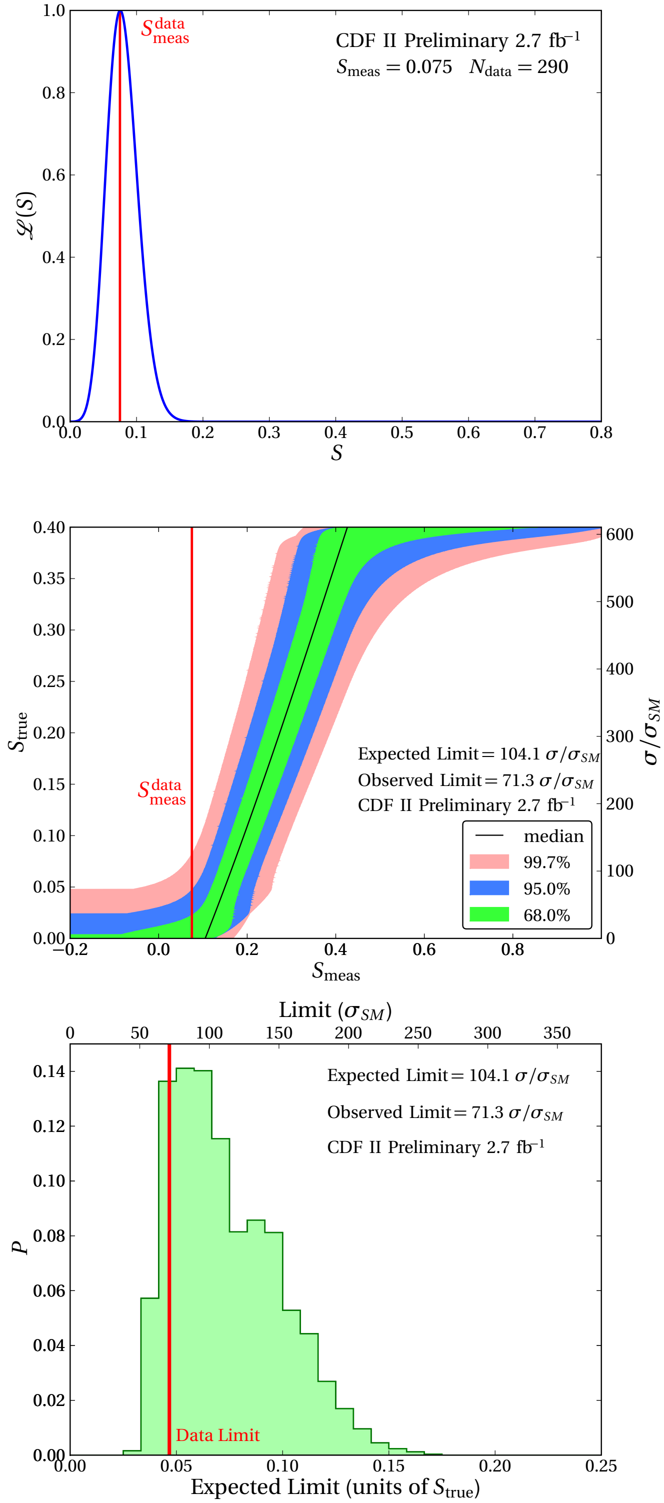

FIGURE A.11: $M_H = 150\ GeV/c^2$

Bibliography

[1] A.A. Michelson. *Light Waves and their Uses*. University of Chicago Press, Chicago, 1903.

[2] P.W. Higgs. Broken Symmetries and the Masses of Gauge Bosons. *Physical Review Letters*, 13(16):508–509, 1964.

[3] SuperK Collaboration. Measurements of the Solar Neutrino Flux from Super-Kamiokande's First 300 Days. *Physical Review Letters*, 81(6):1158–1162, Aug 1998. doi: 10.1103/PhysRevLett.81.1158.

[4] D. Griffiths. Introduction to Elementary Particles. *John Willey & Sons Inc*, 1987.

[5] Wikimedia Commons. Creative commons attribution 3.0 unported. *Wikipedia*, 2006. URL http://commons.wikimedia.org/wiki/File:Standard_Model_of_Elementary_Particles.svg. [Online; accessed 27-April-2009].

[6] C. Amsler et al. (Particle Data Group). Review of Particle Physics. *Physics Letters B*, 667:1–6, 2008. doi: 10.1016/j.physletb.2008.07.018. URL http://pdg.lbl.gov.

[7] V.D. Barger and R.J.N. Phillips. *Collider Physics*. Westview Press, 2nd edition, 1996.

[8] I.J.R Aitchison and A.J.G. Hey. *Gauge Theories in Particle Physics*, volume 1-2. Taylor and Francis Group, New York, 3rd edition, 2003.

[9] J. Goldstone. Field theories with Superconductor solutions. *Il Nuovo Cimento (1955-1965)*, 19(1):154–164, 1961.

[10] B.W. Lee, C. Quigg, and H. B. Thacker. Weak Interactions at Very High Energies: The Role of the Higgs-Boson Mass. *Physical Review D*, 16(5):1519–1531, Sep 1977. doi: 10.1103/PhysRevD.16.1519.

[11] B.W. Lee, C. Quigg, and H. B. Thacker. Strength of Weak Interactions at Very High Energies and the Higgs Boson Mass. *Physical Review Letters*, 38(16):883–885, Apr 1977. doi: 10.1103/PhysRevLett.38.883.

[12] T. Hambye and K. Riesselmann. Matching Conditions and Higgs Boson Mass Upper Bounds Reexamined. *Physical Review D*, 55(11):7255–7262, Jun 1997. doi: 10.1103/PhysRevD.55.7255.

[13] M. Carena and HE Haber. Higgs Boson Theory and Phenomenology. *Progress in Particle and Nuclear Physics*, 50(1):63–152, 2003.

[14] Tevatron Electroweak Working Group. Combination of CDF and D0 Results on the Mass of the Top Quark. *arXiv*, 0903.2503, 2009. URL http://arxiv.org/abs/0903.2503.

[15] ALEPH, CDF, D0, DELPHI, L3, OPAL, SLD Collaborations et al. Precision Electroweak Measurements and Constraints on the Standard Model. *arXiv*, 0811.4682v1, Nov 2008. URL http://arxiv.org/abs/0811.4682v1.

[16] LEPEWWG. LEP Electroweak Working Group Report. 2009. URL http://lepewwg.web.cern.ch/LEPEWWG. [Online; accessed 16-May-2009].

[17] TeV4LHC web page, 2009. URL http://maltoni.home.cern.ch/maltoni/TeV4LHC. [Online; accessed 5-May-2009].

[18] D. Hidas. Search for Standard Model Higgs Bosons Decaying to W-Boson Pairs in $p\bar{p}$ Collisions at $\sqrt{s} = 1.96$ TeV. *CDF Note*, 9734, Oct 2007. URL http://www-cdf.fnal.gov/thesis/cdf9734_DeanHidasThesis_1.pdf.

[19] Fermilab Beams Division Collaboration. *Tevatron Run 2 handbook*. Fermilab, 1998.

[20] CDF Collaboration. The CDF detector: an overview. *Nuclear Instruments and Methods in Physics Research A*, 271:387.

[21] CDF Collaboration. Measurement of the J/ψ meson and b-hadron production cross sections in $p\bar{p}$ collisions at $\sqrt{s} = 1960\ GeV$. *Physical Review D*, 71(3):032001, Feb 2005. doi: 10.1103/PhysRevD.71.032001.

[22] CDF Collaboration: D. Acosta et al. The CDF Cherenkov luminosity monitor. *Nuclear Inst. and Methods in Physics Research, A*, 461(1-3):540–544, 2001. doi: 10.1016/S0168-9002(00)01294-8.

[23] CDF Collaboration: D. Acosta et al. The performance of the CDF luminosity monitor. *Nuclear Inst. and Methods in Physics Research, A*, 494(1-3):57–62, 2002. doi: 1016/S0168-9002(02)01445-6.

[24] CDF Collaboration. Intermediate silicon layers detector for the CDF experiment. *Nuclear Inst. and Methods in Physics Research, A*, 453(1-2):84–88, 2000. doi: 10.1016/S0168-9002(00)00610-0.

[25] CDF Collaboration. CDF Run II silicon tracking projects. *Nuclear Inst. and Methods in Physics Research, A*, 447(1-2):1–8, 2000. doi: 10.1016/S0168-9002(00)00166-2.

[26] T. et al. CDF Collaboration: Affolder. CDF central outer tracker. *Nuclear Inst. and Methods in Physics Research, A*, 526(3):249–299, 2004. doi: 10.1016/j.nima.2004.02.020.

[27] L. Balka et al. The CDF central electromagnetic calorimeter.

[28] CDF Collaboration: S. Bertolucci et al. The CDF central and endwall hadron calorimeter. *Nuclear Inst. and Methods in Physics Research, A*, 267(2-3):301–314, 1988. doi: 10.1016/0168-9002(88)90476-7.

[29] S. et al. CDF Collaboration: Kuhlmann. The CDF calorimeter upgrade for Run IIb. *Nuclear Inst. and Methods in Physics Research, A*, 518(1-2):39–41, 2004. doi: 10.1016/j.nima.2003.10.018.

[30] CDF Collaboration: E.J. Thompson et al. Online track processor for the CDF upgrade. *IEEE Transactions on Nuclear Science*, 49(3 Part 2):1063–1070, 2002. doi: 10.1109/TNS.2002.1039615.

[31] A. et al. CDF Collaboration: Bhatti. Determination of the jet energy scale at the Collider Detector at Fermilab. *Nuclear Inst. and Methods in Physics Research, A*, 566 (2):375–412, 2006. doi: 10.1016/j.nima.2006.05.269.

[32] CDF Collaboration. Search for the Higgs Boson Produced in Association with $Z \rightarrow l^+l^-$ in $p\bar{p}$ Collisions at $\sqrt{s} = 1.96$ TeV. *Physical Review Letters*, 101(25): 251803, 2008. doi: 10.1103/PhysRevLett.101.251803.

[33] CDF Collaboration. First Measurements of Inclusive W and Z Cross Sections from Run II of the Fermilab Tevatron Collider. *Physical Review Letters*, 94(9): 091803, Mar 2005. doi: 10.1103/PhysRevLett.94.091803.

[34] J.Z Efron. Search for the Higgs Boson in the ZH → llbb Channel at CDF Run II. *CDF Note*, 8976, Oct 2007. URL http://www-cdf.fnal.gov/thesis/cdf8976_ZHllbb_JZE_Thesis_2.ps.gz.

[35] CDF Collaboration. Measurement of the $t\bar{t}$ Production Cross Section in $p\bar{p}$ Collisions at $\sqrt{s} = 1.96\ TeV$ Using Dilepton Events. *Physical Review Letters*, 93(14): 142001, Sep 2004. doi: 10.1103/PhysRevLett.93.142001.

[36] CDF Collaboration. Measurement of the $t\bar{t}$ Production Cross Section in $p\bar{p}$ Collisions at $\sqrt{s} = 1.96\ TeV$ using Lepton + Jets Events with Secondary Vertex b -tagging. *Physical Review D*, 71(5):052003, Mar 2005. doi: 10.1103/PhysRevD.71.052003.

[37] Michelangelo L. Mangano, Mauro Moretti, Fulvio Piccinini, Roberto Pittau, and Antonio D. Polosa. ALPGEN, a Generator for Hard Multiparton Processes in Hadronic Collisions. *Journal of High Energy Physics*, 07:001, 2003.

[38] Daniel Stump et al. Inclusive jet production, parton distributions, and the search for new physics. *Journal of High Energy Physics*, 10:046, 2003. URL http://arxiv.org/abs/hep-ph/0303013.

[39] B. Jayatilaka. A Measurement of the Top Quark Mass in the Dilepton Decay Channel at CDF II. *CDF Note*, 8481, 2006. URL http://www-cdf.fnal.gov/thesis/cdf8481_me_dil_thesis.pdf.

[40] G.P. Lepage. A new algorithm for adaptive multidimensional integration. *Journal of Computational Physics*, 27(2):192–203, 1978.

[41] J. Campbell, R. K. Ellis, F. Maltoni, and S. Willenbrock. Production of a Z boson and two jets with one heavy-quark tag. *Physical Review D*, 73(5):054007, 2006. doi: 10.1103/PhysRevD.73.054007.

[42] John Campbell and R. K. Ellis. Radiative corrections to $Zb\bar{b}$ production. *Physical Review D*, 62(11):114012, Oct 2000. doi: 10.1103/PhysRevD.62.114012.

[43] J. Alwall, P. Demin, S. de Visscher, R. Frederix, M. Herquet, F. Maltoni, T. Plehn, D.L. Rainwater, and T. Stelzer. MadGraph/MadEvent v4: The New Web Generation. *Journal of High Energy Physics*, 09:028, 2007. URL http://arxiv.org/abs/0706.2334.

[44] G. Mahlon and S.J. Parke. Maximizing spin correlations in top quark pair production at the Tevatron. *Physics Letters B*, 411(1-2):173–179, 1997.

[45] G. Mahlon and S.J. Parke. Improved spin basis for angular correlation studies in single top quark production at the Tevatron. *Physical Review D*, 55(11):7249, 1997.

[46] Wikipedia. Maximum likelihood, 2009. URL http://en.wikipedia.org/w/index.php?title=Maximum_likelihood&oldid=288802199. [Online; accessed 16-May-2009].

[47] Wikipedia. Bootstrapping (statistics), 2009. URL http://en.wikipedia.org/w/index.php?title=Bootstrapping_(statistics)&oldid=287033127. [Online; accessed 12-May-2009].

[48] B. Efron and R. J. Tibshirani. *An Introduction to the Bootstrap*. Chapman and Hall, New York, 1993.

[49] R. Barlow. Application of the Bootstrap Resampling Technique to Particle Physics Experiments. Technical report, MAN/HEP/99, 2000.

[50] J.A. Nelder and R. Mead. A Simplex Method for Function Minimization. *The Computer Journal*, 7(4):308, 1965. doi: 10.1093/comjnl/7.4.308.

[51] Wikipedia. Nelder-mead method, 2009. URL http://en.wikipedia.org/w/index.php?title=Nelder-Mead_method&oldid=286921633. [Online; accessed 29-April-2009].

[52] G.J. Feldman and R.D. Cousins. Unified Approach to the Classical Statistical Analysis of Small Signals. *Physical Review D*, 57(7):3873–3889, Apr 1998. doi: 10.1103/PhysRevD.57.3873.

[53] CDF Collaboration: T. Aaltonen et al. Measurement of the top quark mass with dilepton events selected using neuroevolution at CDF. *Physical Review Letters*, 102: 152001, 2009. doi: 10.1103/PhysRevLett.102.152001.

[54] John D. Hunter. Matplotlib: A 2d graphics environment. *Computing in Science and Engineering*, 9(3):90–95, 2007. ISSN 1521-9615. doi: 10.1109/MCSE.2007.55.